National Library
of Canada

Acquisitions and
Bibliographic Services Branch

395 Wellington Street
Ottawa, Ontario
K1A 0N4

Bibliothèque nationale
du Canada

Direction des acquisitions et
des services bibliographiques

395, rue Wellington
Ottawa (Ontario)
K1A 0N4

Your file Votre référence

Our file Notre référence

NOTICE

The quality of this microform is heavily dependent upon the quality of the original thesis submitted for microfilming. Every effort has been made to ensure the highest quality of reproduction possible.

If pages are missing, contact the university which granted the degree.

Some pages may have indistinct print especially if the original pages were typed with a poor typewriter ribbon or if the university sent us an inferior photocopy.

Reproduction in full or in part of this microform is governed by the Canadian Copyright Act, R.S.C. 1970, c. C-30, and subsequent amendments.

AVIS

La qu de cette microforme dépend grandement de la qualité de la thèse soumise au microfilmage. Nous avons tout fait pour assurer une qualité supérieure de reproduction.

S'il manque des pages, veuillez communiquer avec l'université qui a conféré le grade.

La qualité d'impression de certaines pages peut laisser à désirer, surtout si les pages originales ont été dactylographiées à l'aide d'un ruban usé ou si l'université nous a fait parvenir une photocopie de qualité inférieure.

La reproduction, même partielle, de cette microforme est soumise à la Loi canadienne sur le droit d'auteur, SRC 1970, c. C-30, et ses amendements subséquents.

Canada

University of Alberta

Spin-spin relaxation rate MRI dosimetry using ferrous sulphate gelatin materials

by

Cheryl R. Duzenli ©

A thesis submitted to the Faculty of Graduate Studies and Research in partial fulfillment of the requirements for the degree of Doctor of Philosophy

in

Medical Physics

Department of Physics

Edmonton Alberta
Spring 1995

ISBN 0-612-01685-4

University of Alberta

Library Release Form

Name of Author: Cheryl R. Duzenli

Title of Thesis: Spin-spin relaxation rate MRI dosimetry using ferrous sulphate gelatin materials

Degree: Doctor of Philosophy

Year this Degree Granted: 1995

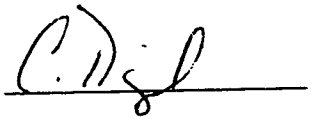

10689 63 Avenue Edmonton,
Alberta T6H 1P7

April 10, 1995

University of Alberta

Faculty of Graduate Studies and Research

The undersigned certify that they have read, and recommend to the Faculty of Graduate Studies and Research for acceptance, a thesis entitled **Spin-spin relaxation rate MRI dosimetry using ferrous sulphate gelatin materials,** by **Cheryl R. Duzenli**, in partial fulfillment of the requirements for the degree of Doctor of Philosophy in Medical Physics.

R. Sloboda
Dr. R. Sloboda

Dr. G. Greeniaus

Dr. D. Robinson

Dr. G. Hughes

Dr. R. Urtasun

Dr. N. Rodning

Dr. L. J. Schreiner, McGill
Dr. L. J. Schreiner

April 6, 1995

Abstract

Recent developments in conformal radiotherapy involving non-standard geometries and time dependent radiation beam configurations, have increased the challenge to provide accurate dosimetry. Existing methods of dose measurement in the clinical setting fall short of fulfilling the need for a volumetric, tissue equivalent, integrating dosimeter to cover the range of clinical applications now available. The volumetric measurement provides for realistic anatomical representation of the patient; tissue equivalence ensures accurate determination of absorbed dose by tissue; and integration provides for the measurement of non-stationary radiotherapy beams.

In this thesis the dosimetry problem is addressed in terms of a measurement technique that merges chemical dosimetry with nuclear magnetic resonance (NMR) and imaging in an attempt to fulfill the above criteria. A general discussion of the dosimetry of ionizing radiation is followed by a summary of the NMR relaxation theory and radiation chemistry required to understand the dosimeter response. Acquisition of accurate relaxation rate data in the spectrometer and imaging settings is discussed. A wide-ranging study of NMR spin-spin relaxation rate (*R2*) in the ferrous sulphate gelatin dosimeter system is presented. This includes an investigation of the frequency dependence of both *R2* and spin-lattice relaxation rate (*R1*) in aqueous solutions containing ferrous or ferric ions. Also explored are the effects of acid and gelling agent concentrations on the *R2* response of the dosimeter material, and on diffusion of ferric ions within the material. The effects of benzoic acid, of spontaneous oxidation, and of temperature on the dosimeter are also explored.

Correction techniques for *R2* distortion in the imaging setting are discussed. A novel method of producing accurate distributions of changes in *R2* ($\Delta R2$) to reflect absorbed dose is demonstrated. This method, termed the echo quotient technique, is then applied to external electron beam dosimetry, dynamic external photon beam

Abstract

dosimetry and [illegible] rate (HDR) brachytherapy dosimetry. The dosimetric quality of the $\Delta R2$ image data [illegible] ussed and compared with film, diode and ion chamber data.

Finally, a summary and conclusions regarding the viability of the technique include the following:

- measuring $\Delta R2$ at the highest available imaging frequency provides the best sensitivity to dose,
- a standard dosimeter composition providing the best compromise between good sensitivity to dose and reduction of ion diffusion rates has been determined to be 4% gelatin by weight, 0.05 MH_2SO_4 and 1 mM $FeSO_4$,
- O_2 depletion effects are significant but can be avoided,
- maintaining a constant phantom temperature during the imaging process is important,
- gelatin is inferior to agarose as a gelling agent in terms of both dosimeter sensitivity enhancement and reduction of ion diffusion rate,
- and, the echo quotient technique allows dose distributions to be measured in extended phantoms to an accuracy of ±1 Gy with a spatial resolution of 1 mm x 1 mm x 5 mm.

Acknowledgements

I would like to acknowledge the support of the many people who contributed to the successful completion of this Ph.D. program. In particular I would like to thank my supervisor, Dr. R. Sloboda for encouragement and guidance along the way. I am grateful to all the members of the Medical Physics department at the Cross Cancer Institute for their friendship, making this an enjoyable period of my life.

I would like to thank all the members of my graduate committee for the time and effort they put in to review and comment on the thesis.

And finally, without the continuing moral support of my husband Zeki, none of this would have been possible. Together we have accomplished many things in these past few years. A special thanks also to my children Sibel and Erkin who patiently waited for me to come home on those late nights at the office.

Table of Contents

List of Figures

page

List of Tables

Chapter 1

Introduction

1.1 Overview of radiation dosimetry

Radiation absorbed dose (D) is defined as the absorbed energy (E) per unit mass (m) of absorbing material

$$D = \frac{dE}{dm}. \qquad 1.1$$

The mass dm must be small enough such that dose is defined at a point but large enough such that statistical fluctuations in dose are negligible. In radiotherapy, the ionizing radiation is usually photons or electrons in the energy range from 100's of keV to 10's of MeV. A limited number of institutions worldwide provide radiotherapy using other particles but in this thesis, reference will be made only to the more common modalities. Radiation may be delivered to the treatment site by either externally applied beams (teletherapy) or by internally placed radionuclide sources (brachytherapy).

An example of a dosimetry application is shown in Figure 1.1, where an arrangement of external beams selected to suit the contours of a treatment site is represented. The target dose is prescribed to structure A, while B indicates a radiation sensitive structure that limits the maximum dose that can be safely delivered to A. Accurate determination of the absorbed dose distribution is necessary in order to design an optimum configuration of radiation beams in terms of position, size, shape, beam type and energy. The treatment beams may be either stationary or time modulated, uniform or intensity modulated, in order to better conform to the target region and spare normal tissue. Dosimetry is complicated by the curved incident surfaces and internal structures such as C, D and E. Ideally the dose distribution should be known in three dimensions to an accuracy of ± 5% [NCRP 1981, ICRU 1993].

The standard dosimetric data sets from which clinical dose distributions are calculated are schematically represented in Figure 1.2. These standard data sets are acquired in water for each type of radiation beam in clinical use and also provide a reference for inter-comparison of different measurement and calculation techniques. Bridging the gap between the standard data set and the clinical dose distribution for a

combination of beams is the main dosimetric problem both from the calculation and measurement point of view. The aim of this thesis is to further explore and improve a dosimetry technique that has the potential to provide integrated volumetric dose information in realistic anatomical, tissue-equivalent phantoms.

A brief discussion of other dose measurement techniques will outline the need for a new class of dosimeter. There are many tools available to the medical physicist for measuring radiation dose either in an absolute or relative sense. In general, each tool is suited to a particular aspect of the problem. Electromagnetic radiation in the energy range of interest can ionize and excite the atoms and molecules of matter upon which it is incident. By monitoring the extent of physical and chemical changes in the absorbing material, the absorbed dose to the medium can be deduced. To clarify the conversion from dosimeter reading to dose, the primary modes of interaction of high energy photons and electrons with matter are reviewed in Chapter 2. A very good overview of dosimetry techniques is available elsewhere in the literature [Attix *et al.* 1966].

Devices such as ionization chambers, solid state diodes, radiographic film and thermoluminescent dosimeters (TLD) are commonly used in most medical physics departments today. These devices do not provide a measure of absolute dose but do provide relative dosimeter readings that may be converted to dose using a calibration factor or dose response curve. Relative dose distributions referenced to a standard calibration are adequate for the planning and verification of radiation therapy treatments. Recently, radiochromic film and plastic scintillation detectors have been introduced to supplement the arsenal of traditional dosimeters. Dosimetry standards for reference include free air ionization chambers, calorimetry and liquid ferrous sulphate (Fricke) spectrophotometry.

Ionization chambers are the most widely used dose measurement devices. They generally consist of a gas (usually air) filled cavity surrounded by a solid wall. Charge liberated during ionization of the air is collected and related to the dose that would be absorbed in the volume of the medium occupied by the chamber. Because both the cavity gas and the wall material usually differ in density and atomic number from the medium, corrections must be made for differences in mass energy absorption coefficients and mass collisional stopping powers at the mean photon and electron energies of interest. Effectively, ionization chambers measure dose at a point, however they may be used to map radiation dose distributions by scanning the detector, enclosed in a waterproofing sheath, throughout a water tank, and measuring relative dose rate. Scanning techniques lose utility when the radiation distribution is modulated in time,

although arrays of ion chambers used in integrating mode may be used in this case. Due to cost, such detector arrays are usually one-dimensional, making inefficient use of both beam time and operator time for the measurement of extended dose distributions. Also, it is often difficult to simulate patient anatomy using a water tank. The chamber size governs the spatial resolution and varies from ~2-20 mm but is typically on the order of 5 mm diameter. Reproducibility is usually better than 1%. Sensitivity depends on chamber size but generally doses in the cGy range are measurable. Chamber response varies linearly with dose under most conditions except at very high dose rates where detector response time is exceeded or ion recombination occurs.

Solid state diodes, generally doped silicon p-n junctions, are also point measurement or scanning detectors and therefore suffer the same limitations as ion chambers for the measurement of extended dose distributions. Diodes may be used in reverse biased or unbiased mode where charges liberated by ionizing events are collected. Caution must be used in converting the diode signal to dose in the medium due to the diode's high atomic number compared with water and the directional dependence of the diode response [Rikner 1983]. In particular, caution must be used in cases where the energy spectrum of the beam changes markedly. Due to both the high density of silicon and lower energy required to create an electron-hole pair in silicon compared with air, diode sensitivity is significantly higher than ion chamber sensitivity. Diodes can therefore be made smaller than ionization chambers, improving spatial resolution to the order of 1 mm. Diode stability with temperature is of concern and reproducibility is on the order of 1% under optimal conditions. Diodes have very fast response times and response is linear with dose. Diodes eventually sustain radiation damage and lose their ability to function.

TLD is an integrating point measurement technique, each dosimeter being an individual packet of powder or chip. The most common TLD material is lithium fluoride, although a range of other materials is available. The effective atomic number of LiF is only slightly higher than that of water but calibration at the energy of interest is still required. Arrays of TLD dosimeters may be used to determine a dose distribution, but this is a very inefficient process (even with automated readout) since each TLD is read sequentially requiring ~ 1 minute per reading. Carefully measured dose response curves are necessary for the particular processing and measurement conditions chosen, and reproducibility is no better than ±2%. Spatial resolution is on the order of 2 mm. TLD response generally varies linearly with dose up to the kGy range but may require a separate dose response curve for the low dose region. Sensitivity allows measurement down to ~1 cGy.

Radiographic film provides a two-dimensional map of dose but its response is strongly energy dependent due to the high effective atomic number of silver bromide. Dependence on processing conditions, light sensitivity and problems with accurate positioning within phantoms may also pose problems for quantitative dosimetry. Dose response curves show a limited region of linearity where the number of developable silver bromide grains is proportional to dose. Beyond this region, the dose response curve is non-linear and saturates at a certain dose dependent upon the type of film. Dose response curves are required for each batch of film, each set of processing conditions, each beam type and irradiation configuration (whether the film is placed parallel or perpendicular to the beam). Spatial resolution is excellent, limited only by the scanning aperture, which is typically ~0.5 mm. Reproducibility is on the order of ±2% under the best conditions.

Plastic scintillation detectors have been recently designed and evaluated for use in external beam radiotherapy dosimetry [Beddar *et al.* 1992 a, b]. These devices provide the advantage of being very nearly water-equivalent in terms of dose response, as well as having high sensitivity, allowing for small detector size. The plastic scintillator is coupled to a photomultiplier tube (PMT) by means of an optical fibre and must be accompanied by a second fiber and PMT to provide a background signal measuring the contribution of Cerenkov radiation produced in the fiber to the total light signal. The detector response is linear with dose over the range from 40 to 400 cGy. Depth dose and profile measurements compare well with those obtained using diodes and ion chambers. Spatial resolution on the order of 1 mm is achievable. Plastic scintillators are again point measurement devices. Large arrays of such detectors would currently be prohibitively expensive since each detector requires two PMT's. Use of arrays of plastic scintillators could become feasible with the replacement of the PMT by some other photosensitive device such as a photodiode.

Recently, radiochromic film has been developed as a dosimeter [McLaughlin *et al.* 1991]. This is a light-insensitive medium that shows visible darkening upon irradiation. Optical density gives a measure of dose. Sensitivity is very low, requiring doses in the 10's to 100's of Gy, but water equivalence of the material is good. Limited data on the dose response characteristics are available at this time but the present cost of the material is prohibitively high for routine measurement of extended dose distributions.

Absolute dose can be measured using spectrophotometry with chemical dosimeters (such as the Fricke dosimeter), calorimetry, or free-air ionization chambers. These methods cannot generally be used under conditions simulating in vivo situations.

In practice in the clinic, a relative dosimeter is calibrated against one of these absolute dose standards.

The magnetic resonance imaging (MRI) gel dosimeter is a new class of dosimeter that involves mapping out radiation-induced chemical changes in materials using magnetic resonance imaging. The chemical changes may take on a variety of forms. To date, two different processes amenable to MRI readout have been reported. The first proposed MRI gel dosimeter material was based on the well-studied liquid Fricke dosimeter [Fricke and Morse 1927]. The Fricke dosimeter is an aqueous solution containing ferrous ions which undergo oxidation to ferric ions in amounts proportional to absorbed dose. This change from one paramagnetic species to another is detectable by measuring NMR relaxation rates. Used in the liquid form, either with spectrophotometry or NMR relaxometry, the Fricke solution is an absolute dosimeter when the yield of ferric ions with dose is predetermined. MRI can be used to measure concentrations of the paramagnetic ferric ions and hence obtain spatial distributions of dose when the ions are immobilized in a gel matrix. More recently, polymers that undergo polymerization and cross-linking within a gel matrix have been proposed [Maryanski *et al.* 1993, 1994] as candidates for MRI gel dosimetry, based on changes in the motional characteristics of the solvent water molecules following radiation. The degradation of polymers in liquid suspension has also been investigated using NMR [Audet and Schreiner 1991]. Degradation of polymers produces less marked effects on NMR relaxation times compared with polymerization and cross linking, and are not useful for radiotherapy applications.

The main potential advantage of the MRI-gel technique is that integrated dose distributions can be efficiently obtained in any spatial orientation. Furthermore, gel materials can be designed to accurately simulate both the effective atomic number and density of tissue as well as the geometry of the treatment site. Many applications including external beam conformal radiotherapy (including stereotactic radiosurgery) and high dose rate brachytherapy stand to benefit from the development of MRI gel dosimetry. A schematic representation of how the MRI gel technique works is shown in Figure 1.3.

1.2 Liquid Fricke dosimetry

The aqueous ferrous sulphate dosimeter known as Fricke solution works on the principle that water radiolysis products lead to oxidization of ferrous ions (Fe^{2+})

to ferric ions (Fe^{3+}) in proportion to the absorbed dose. Using spectrophotometry to measure the ferric ion concentration [Fe^{3+}], vessels containing approximately 1 ml of solution are irradiated to obtain the average dose over this volume. Absorbed dose is determined by measuring optical absorption at one of two main wavelengths, 224 nm or 304 nm.

The standard dosimeter consists of 10^{-3} M $FeSO_4$ or $Fe(NH_4)_2(SO_4)_2$ and 0.4 M H_2SO_4 in aerated, purified water. The sulphuric acid content was chosen [Fricke and Peterson 1927] to create the same mass absorption coefficient as air. The accepted value of the radiation chemical yield $G(Fe^{3+})$ for the standard Fricke solution is 15.5 ± 0.2 ions $(100\ eV)^{-1}$ [Fricke and Hart 1966]. For solutions of composition closer to water, 0.05 M H_2SO_4 may be used, but below this concentration the sensitivity of the dosimeter decreases. Over the years, several modifications have been tried in order to improve the response of the Fricke dosimeter. Extensive study has revealed that stabilization against trace organic impurities, improved sensitivity, and extended linear dose range can all be controlled by varying the composition of the solution [Fricke and Hart 1966 and references therein]. The standard solution shows a linear dose response over the dose range from 40 Gy to 400 Gy and may be used to measure doses over this range with better than 1% reproducibility.

It has long been known that the presence of paramagnetic species in aqueous and other materials has a dramatic influence on NMR relaxation rates [Bloembergen 1957]. It was only recently realized that this could be exploited for dosimetry purposes [Gore *et al.* 1984]. A linear variation in relaxation rate with increasing ferric ion concentration and dose in Fricke solution was demonstrated. The radio-chemical reactions and relaxation rate response were reported to proceed when the Fricke solution was incorporated into a gel matrix, and other possible, but less sensitive, paramagnetic chemical NMR dosimeters including ceric sulfate and cupric-ferrous sulfate were described.

A detailed NMR study of the liquid Fricke dosimeter has been recently carried out [Podgorsak and Schreiner 1992]. The spin-lattice relaxation rate ($R1$) was found to vary linearly with dose, with saturation at about 400 Gy. This dosimeter was slightly more sensitive at a resonant frequency of 9 MHz compared with 25 MHz, as theoretically predicted. The minimum detectable dose in this system, measuring $R1$, was 4 Gy. This provided an obvious advantage over spectrophotometry where doses of this magnitude can only be measured using very large absorption cells (10 cm long) and special techniques [Fricke and Hart 1966]. Sample sizes in NMR may be on the order of 0.1 ml allowing the average dose to be measured over a much smaller volume. The liquid

Fricke dosimeter showed enhanced *R1* response with the addition of up to ~ 10^{-2} M ethanol. It was further demonstrated that the liquid Fricke dosimeter *R1* response could be modeled using a three-site fast-exchange model.

1.3 Fricke-gel NMR dosimetry

The concept of measuring dose in two or three dimensions using gel-based dosimeters has been around for many years [Fricke and Hart 1966]. Using dye incorporated into gels or plastics, two-dimensional readout was done using colorimetric densitometry or visual inspection. Three-dimensional measurement however, could only be done in a destructive way by sectioning the sample. Methylene blue and other radiation-sensitive dyes in gelatin, agar gels and polyvinyl alcohol have been investigated, but problems with reproducibility were cited. Diffusion of the dye molecules post-irradiation also contributed to blurring of the dose distribution. As mentioned in Section 1.1, photopolymerization and cross-linking of polymers in gels form the subject of current NMR dosimetry investigations.

The use of Fricke solution incorporated into gel was not explored during the early period of dosimetry development, probably due to the enhancement of spontaneous oxidation of Fe^{2+} in the presence of impurities (such as the gelling agent) in the system and the difficulty of using spectrophotometry on extended sample sizes. The idea of combining the ferrous sulphate solution with a gel matrix and measuring spatial distributions of ferric ion using MRI followed Gore's work of 1984 [Gore *et al.* 1984]. Several notable investigations into the *R1* response to dose have led to further understanding of the Fricke gel dosimeter [Appleby *et al.* 1987, Olsson *et al.* 1989, Schulz *et al.* 1990, Olsson 1991, Hazle *et al.* 1991, Audet *et al.* 1993, Keller 1994, Kron and Pope 1994]. In one study [Guan *et al.* 1993], a xylenol orange ferric ion indicator was used to give a visible dose response, but NMR relaxation rate was not used as a measure of dose.

Appleby [1987] investigated *R1* in Fricke agarose gels with the addition of benzoic acid, without reoxygenation, however no comparison was done for gels without benzoic acid. Olsson *et al.* [1989, 1990, 1991] have looked at ferrous ion concentration, dose rate, beam energy and intrinsic oxidation effects in Fricke-agarose gel. Observations included decreased *R1* sensitivity in agarose with increasing ferrous ion concentration due to competition for radicals with the gel, and cooling-rate effects. The *R1* sensitivity of 0.196 s^{-1} Gy^{-1} quoted for 0.5 mM $FeSO_4$ by Olsson *et al* [1991] is the

highest sensitivity reported in the literature to date for any Fricke gel material, but the dose response curve was very non-linear and reproducibility was not quoted. The 1 mM $FeSO_4$ agarose dose response curve was linear with a sensitivity of 0 130 s^{-1} Gy^{-1}, approximately 4 times more sensitive than liquid Fricke. Schulz *et al.* [1990] also studied oxygenation, agarose concentration, ferrous ion concentration, acid content, dose-rate dependence, and post-preparation time effects on the Fricke agarose *R1* response. Also demonstrated in Schulz's work was a slight increase in *R1* sensitivity at a frequency of 85 MHz compared to 21 MHz, which is in contradiction with theory unless the ferric ion is bound to a macromolecule [Koenig *et al.* 1984]. This observation is not supported by any further investigation.

Olsson [1989] studied the *R1* response of Fricke gelatin, showing increased sensitivity over liquid Fricke by a factor of 2.2 for 4% gelatin. Increasing gelatin concentration decreased sensitivity. Hazle *et al.* [1991] observed that the sensitivity increased slightly with increasing ferrous ion concentration in Fricke gelatin. Olsson [1991] explained this by postulating that chain oxidation reactions do not occur in the gelatin system as they do in agarose gel. The *R1* sensitivity quoted by Hazle *et al.* is approximately 1/2 the *R1* sensitivity in agarose. Most recently, Keller [1994] has investigated Fricke gelatin dose response properties in terms of *R1*. The oxygen depletion effect was examined and the first example of dose fractionation effects were presented.

There are currently only three studies which present *R2* measurements of Fricke gel materials [Gore *et al.* 1984, Prasad *et al.* 1991, Gambarini *et al.* 1994], apart from the work that forms part of this thesis [Duzenli *et al.* 1994, see Chapter 4]. Agarose was used as the gelling agent in the three former studies.

Studies have been done using gelling agents other than gelatin or agarose [Hiraoka *et al.* 1986, 1992a-b, 1993, deGuzman *et al.* 1989], however no particular advantage to using any of these gels was identified. An inherent limitation of the Fricke gel dosimeter is diffusion of ferric ions away from their original location following irradiation, leading to blurring of the measured dose distribution. Three studies [Schulz *et al.* 1990, Olsson *et al.* 1992, Kron *et al.* 1994] have reported a diffusion rate for ferric ions in agarose of 1.9 ± 0.1 mm^2 hr^{-1}, but no such data is available for the gelatin-based system. Other polymer gels [Hiraoka *et al.* 1993] do not appear to offer any advantages over agarose in terms of ion diffusion.

Several papers and technical notes have appeared describing potential applications of MRI gel dosimetry to stereotactic radiosurgery [Olsson *et al.* 1992, Schulz *et al.* 1993, Rousseaux *et al.* 1994], inhomogeneous phantom materials in external beam

radiotherapy [Thomas *et al.* 1992], brachytherapy [Schreiner *et al.* 1994, Olsen and Hellesnes 1994] and proton beam therapy [Brunt *et al.* 1994]. Fricke gel dosimetry for superficial x-ray beams has also been examined, making use of the tissue equivalence properties of Fricke gels [Kron and Pope 1994]. The majority of these reports are qualitative in nature, and with the exception of Schreiner *et al.* indicate insufficient accuracy and/or precision of the technique for use in quantitative dosimetry. Stereotactic radiosurgery and brachytherapy applications both require measurement of relatively small volumes in which very steep dose gradients are present. Although small imaging volumes lead to better MRI tip angle homogeneity across the phantom and reduced phantom noise, accuracy of measured dose distributions for these cases may be limited due to ion diffusion in regions of steep dose gradients. It is anticipated that for external beam radiotherapy where dose gradients are generally less steep, the ferrous sulphate gel technique may provide quite adequate dose distributions if problems with tip angle non-uniformity can be overcome.

At the outset of this study then, several important questions remain to be answered including :

- which is the better parameter to measure, *R1* or *R2*, and how does this change with imaging frequency,
- can the dose response sensitivity be accurately reproduced and how does this depend on dosimeter material composition,
- which gelling agent is superior in terms of dose response and ion diffusion, and
- can the technique be used successfully on large phantoms for external beam radiotherapy ?

In response to these questions, the *R2* and *R1* frequency dependence for aqueous solutions containing Fe^{3+} and Fe^{2+} ions, as well as the effects of dosimeter material composition and sample size on dose response sensitivity are explored in Chapter 4. Extension of the NMR technique is made to the imaging setting in Chapter 5, where it is demonstrated that *R2* artifacts arising from inhomogeneities in MRI tip angle throughout the phantom may be largely removed using a novel echo quotient technique for determination of changes in *R2*. An evaluation of the dosimetric potential of the technique compared with other methods is presented in Chapter 6, with summary and conclusions in Chapter 7.

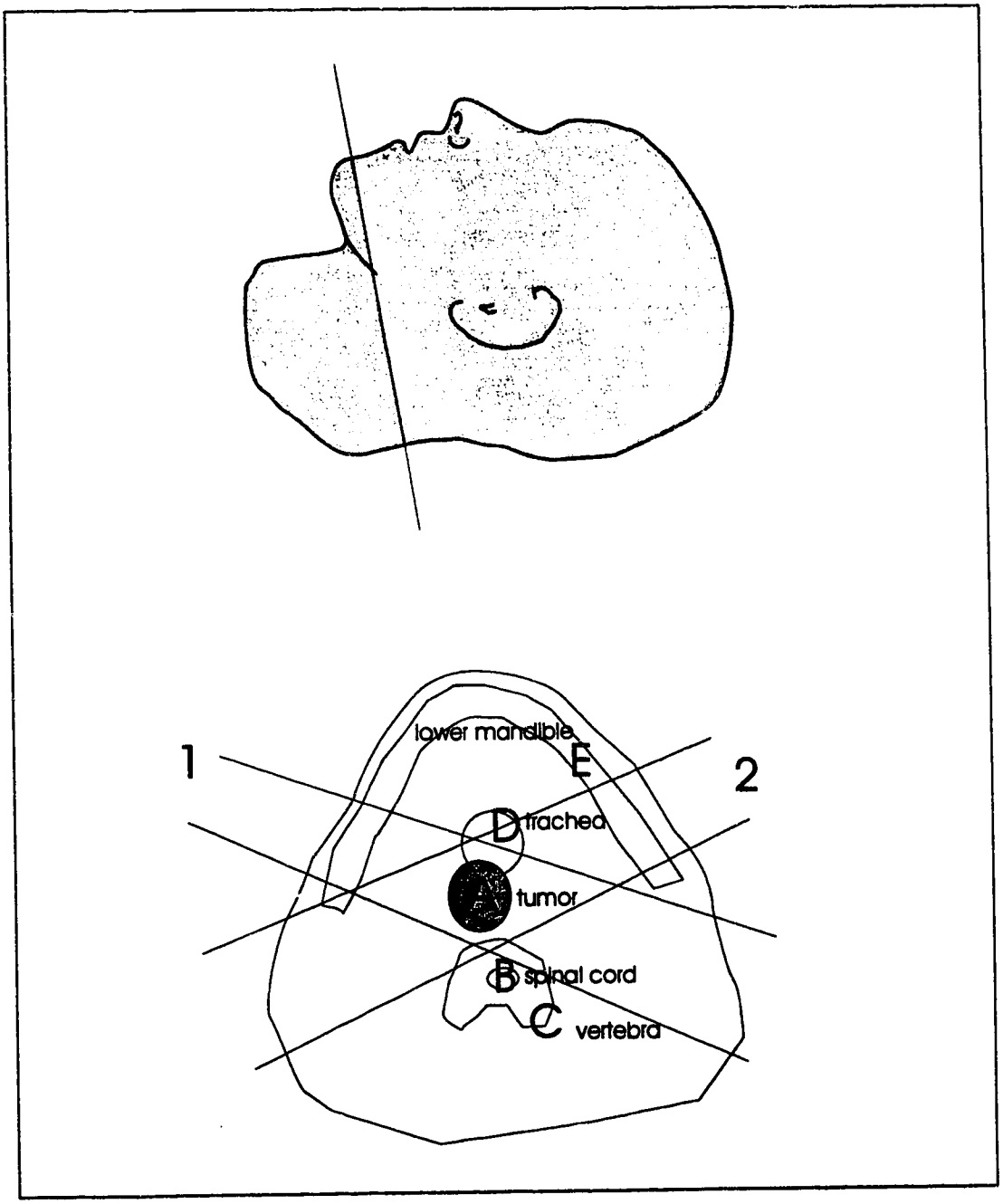

Figure 1.1 Example of a dosimetry application in the head and neck region. The treatment is planned on contours of the patient anatomy taken in the plane of the slice indicated in the upper diagram. In the lower diagram, hypothetical radiation beams 1 and 2 are superimposed on the contours. A calculation of the dose distribution resulting from this arrangment of beams would reveal its efficacity at providing adequate treatment. The optimal beam configuration is then arrived at iteratively by rearranging beams and recalculating the dose distribution.

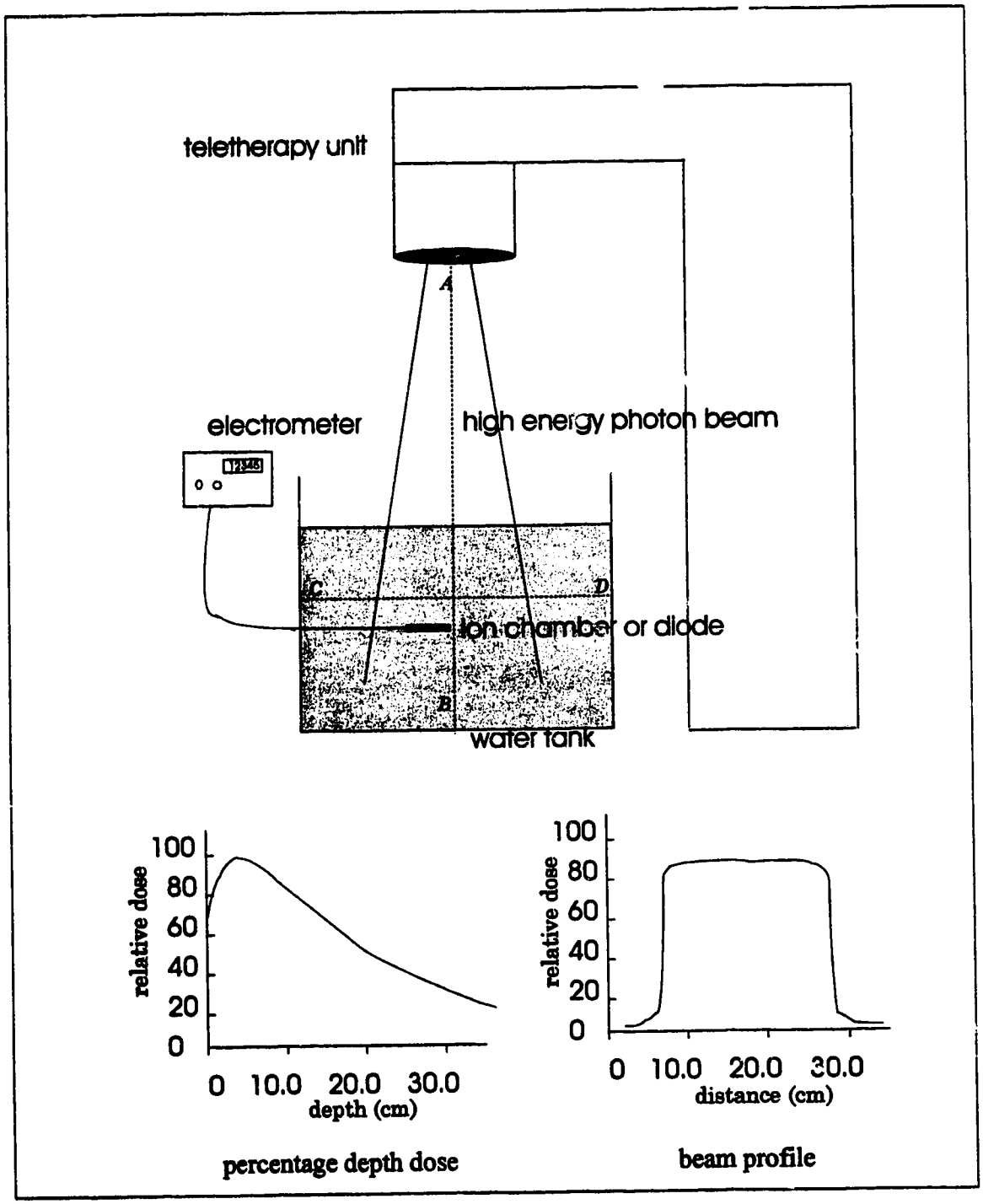

Figure 1.2 Schematic representation of some standard dosimetric data sets acquired for use in external beam treatment planning algorithms. The measurement geometry is indicated in the upper figure. Percent depth dose is measured along the central beam axis AB, while beam profiles are measured at a particular depth parallel to the line CD.

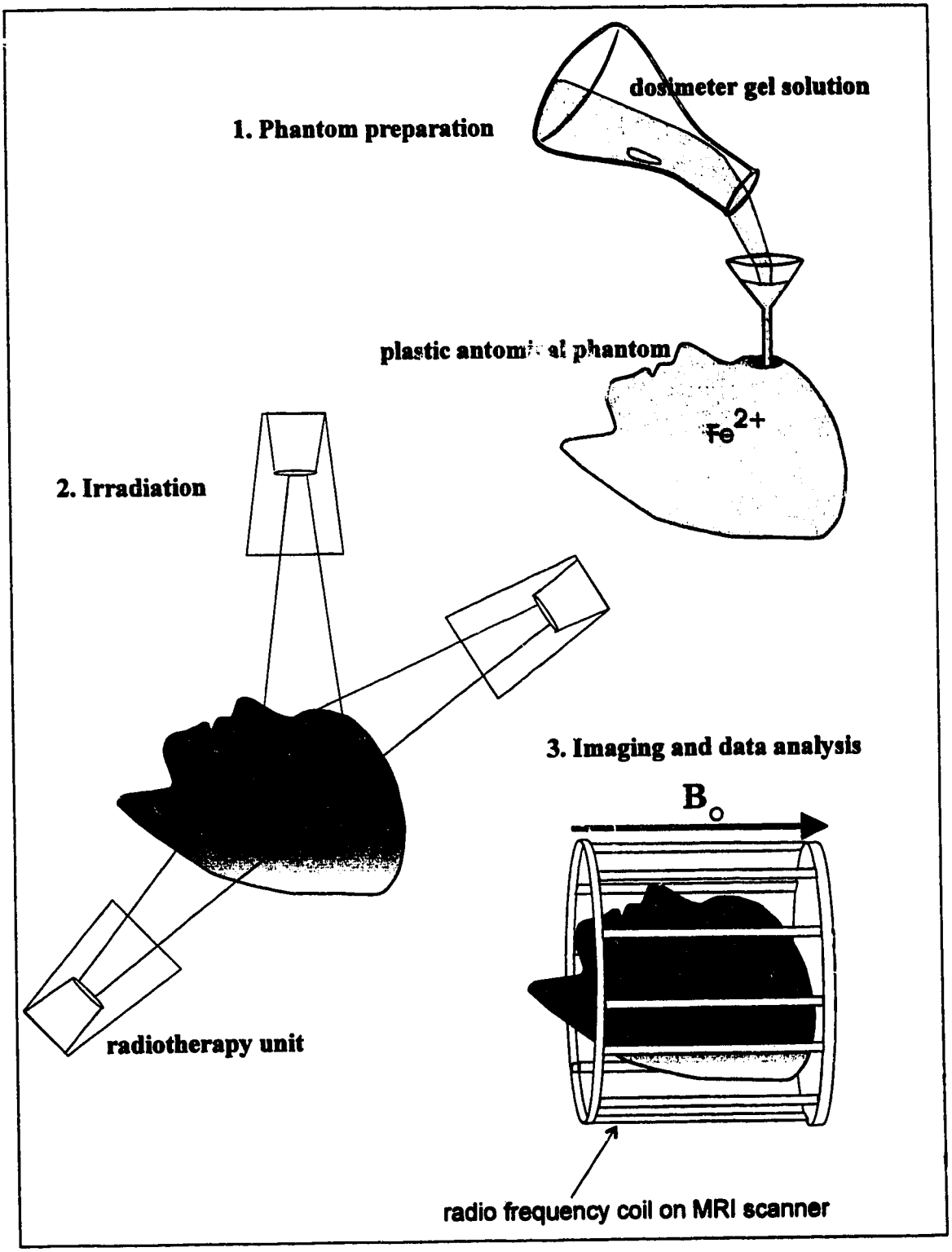

Figure 1.3 Schematic representation of the steps involved in the ferrous sulphate gel- MRI dosimetry technique.

Chapter 2

Theoretical foundations

2.1. Dosimetry of ionizing radiation

The physical and chemical changes occurring in absorbing materials as a result of photon and electron interactions allow the absorbed dose to specialized dosimetry media to be deduced. To understand the conversion from dosimeter reading to dose it is instructive to review the primary modes of interaction of high energy photons and electrons with matter. Photons are referred to as indirectly ionizing since a photon does not directly create a trail of ionized atoms along its path in a medium. At most, a photon can directly ionize only one atom through the photoelectric process or a small number of atoms through Compton scattering processes. However, photon interactions result in energy transfer to electrons which then proceed to create multiple ionizations and excitations along their paths. Electrons, by way of Coulombic interactions, are directly ionizing.

The photoelectric effect, coherent and incoherent scattering and pair production are the primary photon interactions of interest in the therapeutic energy range from ~ 250 keV to ~ 20 MeV. Electrons set in motion as a result of these processes can lose energy through soft or hard collisions with atomic electrons. Soft collisions result in local absorption of small amounts of energy whereas hard collisions can result in energetic knock-on electrons carrying energy away from the incident electron track. Elastic collisions with atomic nuclei will also occur but do not contribute to dose deposition. Bremsstrahlung interactions of electrons with atomic nuclei and electrons result in loss of energy by the electron that is carried away from the site of interaction by photons. The ionizations, excitations, breaking of molecular bonds and heat produced in the medium due to the above processes yield measurable quantities related to dose in dosimeter materials. In a patient these same processes lead to biological damage.

2.1.1 Photon interactions

The dose delivered by a photon beam is the energy transferred (per unit mass) to the medium in the volume of interest, minus the energy carried away from this volume by photons and electrons of high enough energy to escape. The energy

transferred to the medium (ΔE_{tr}) in a small thickness of absorber (Δx) for photons of energy $h\nu$ is given by [Johns and Cunningham 1983]

$$\Delta E_{tr} = \overline{E}_{tr}\mu(Z, h\nu)N\Delta x\,, \qquad 2.1$$

where μ is the linear attenuation coefficient giving the probability of photon interaction per unit absorber thickness Δx. N is the number of incident photons and $\overline{E}_{tr}$ is the average energy transferred per interaction. Z is the atomic number of the absorber, assumed for now to be a pure element. μ is a sum of attenuation coefficients from the three dominant processes: the photoelectric effect, Compton scattering and pair production, discussed below. Attenuation coefficients are derived from basic atomic interaction cross sections (barns atom^{-1}) by multiplying by (N_a/M) x 10^{-24} (cm^2 g^{-1}) (b atom^{-1})$^{-1}$, where N_a is Avogadro's number and M is the atomic mass. Attenuation coefficients may be expressed on a per electron, per atom or per gram basis, the most common being the mass attenuation coefficient (μ/ρ), given by the linear attenuation coefficient divided by the density ρ of the absorbing material.

For dosimetry purposes, mass energy transfer coefficients (μ_{tr}/ρ) and mass energy absorption coefficients (μ_{en}/ρ) have been defined. The mass energy transfer coefficient describes the amount of energy transferred to charged particles (electrons in this case) and is given by the mass attenuation coefficient multiplied by the average energy transferred to an electron as a result of the photon interactions taking place. (μ_{tr}/ρ) is particularly relevant to measurements of ionization produced in air. The mass energy absorption coefficient describes the amount of energy absorbed or deposited locally as a result of photon interactions and is therefore the quantity most relevant to measurement of dose in a medium. $(\mu_{en}/\rho) \leq (\mu_{tr}/\rho)$, the difference being that energy carried away by bremsstrahlung and annihilation photons (as a result of pair production). The radiation yield fraction g is defined such that

$$\frac{\mu_{en}}{\rho} = \frac{\mu_{tr}}{\rho}(1-g). \qquad 2.2$$

The photoelectric effect is responsible for the strong dependence of dosimeter response on atomic number at low photon energies. In this process, a photon is absorbed by an atom, with the ejection of an electron of energy

$$E_e = h\nu - BE\ . \qquad 2.3$$

Here, *BE* is the electron binding energy of the absorbing atom. To satisfy conservation of momentum requirements, the photoelectric effect occurs on bound electrons and the nucleus absorbs the recoil momentum. For photon energies above the K-shell binding energy of the material, an approximate interaction cross section (cm^2 $atom^{-1}$) is given by [Attix 1986]

$$\varphi_{photo} \cong k\frac{Z^n}{(h\nu)^m}, \qquad 2.4$$

where n ranges from approximately 4 to 5 for $h\nu$ ranging from 0.1 MeV to 3 MeV, and m ranges from approximately 3 to 1 over the same energy range. k is a constant independent of photon energy or material. For the mass attenuation coefficient, the Z dependence is reduced by a factor of Z. It is evident that photoelectric interactions are favoured in high atomic number materials and for lower photon energies.

For materials composed of a variety of elements, an effective atomic number for the photoelectric effect, Z_{eff}, is given by the electron fraction weighted average of atomic numbers of the constituent elements [Attix 1986]

$$Z_{eff} = \left[\sum \frac{f_i \times (Z/A)_i}{\sum f_j \times (Z!A)_j} \cdot Z_i^a\right]^{1/a}. \qquad 2.5$$

A is the atomic mass number, f_i the mass fraction for element i, and a depends on the energy spectrum of the beam. To a good approximation, body tissues can be considered to be water-equivalent in terms of absorption of photons and electrons. Using equation 2.5 with a = 3.5, the effective atomic number of water is 7.51 [Johns and Cunningham 1983].

In order for a dosimeter material to absorb energy in a manner similar to water in the photon energy range where the photoelectric effect is important, its effective atomic number must be close to that of water. A comparison of Z_{eff} for various dosimeter materials in Table 2.1 reveals an advantage of the ferrous sulphate gel material over other dosimeters mentioned in Section 1.1. For radiographic film, silver bromide is combined with gelatin forming an emulsion having a Z_{eff} somewhat lower than that of silver bromide alone.

Table 2.1 Comparison of effective atomic numbers for various dosimeter materials

dosimeter	absorbing material	Z_{eff}
	water	7.51
ionization chamber	air	7.78
diode	silicon	14
TLD	lithium fluoride	8.31 (Li=3, F=9)
MRI Fricke-gel	ferrous sulphate gelatin (4% gelatin, 0.05 M H_2SO_4, 1 mM $FeSO_4$)	7.48
radiographic film	silver bromide	(Ag=47, Br=35)

The dominant interaction for medium energy photons (0.1 MeV to 10 MeV) is the Compton interaction. In this process, an incident photon is inelastically scattered from a loosely bound atomic electron. In general the collision can be treated as if the electron were not bound; the binding becoming important only for low photon energies. At low photon energies however, the photoelectric effect dominates the total interaction cross section so that in most cases the unbound electron assumption is adequate. The Klein-Nishina cross section per unbound electron for the Compton interaction is given by [Attix 1986]

$$\sigma = k'\left\{\frac{1+\gamma}{\gamma^2}\left[\frac{2(1+\gamma)}{\zeta}-\frac{1}{\gamma}\ln(\zeta)\right]+\frac{1}{2\gamma}\ln(\zeta)-\frac{1+3\gamma}{\zeta^2}\right\}, \qquad 2.6$$

where k' is a constant, γ is the ratio of photon energy to the rest mass energy of the electron ($h\nu/m_ec^2$) and $\zeta = 1+2\gamma$. Since γ and ζ depend only on the photon energy and not the atomic number of the medium, tissue equivalence of dosimetry materials is not

determined by the Compton interaction. Z will enter into the mass attenuation coefficient through the factor $N_a \cdot Z/A$, but Z/A is ~1/2 for almost all elements except hydrogen. The Compton effect contributes to a changing photon energy spectrum in the absorbing medium.

Other scattering processes also occur at the photon energies of interest, such as coherent Rayleigh scattering where the atom re-radiates the incident photon. Since this process does not lead to absorption of energy by the medium or changes in photon energy, it is not of significant interest in dosimetry.

Pair production involves the transformation of a photon, in the field of a nucleus, to an electron-positron pair. The energy threshold for photons to undergo pair production is 1.02 MeV, the sum of electron and positron rest mass energies. The remaining incident photon energy is shared as kinetic energy between the electron and positron. Any combination of kinetic energy division is possible except for the forbidden case where one particle gets zero kinetic energy. A similar process occurring in the field of an atomic electron is referred to as triplet production. The total pair production interaction cross section per atom is given approximately by

$$\tau = k'' Z^2 f(h\upsilon, Z) \qquad 2.7$$

where f is a slowly decreasing function of Z and an increasing function of photon energy, and k'' is a constant. The Z dependence of the mass attenuation coefficient τ / ρ is reduced to Z. The triplet production cross section may be approximated by replacing Z^2 above by $Z(Z+1)$. Pair production interactions create a relatively less dramatic dependence on atomic number for high energy photons than the photoelectric effect does for low energy photons.

On average it requires about thirty interactions of the above types for a typical (4 MeV) photon to transfer all of its energy to electrons in an absorbing medium [Johns and Cunningham 1983]. The relative contributions to the total mass attenuation coefficient from each of the above processes for two materials is shown in Figure 2.1. Water is compared with molybdenum (having an atomic number of 42, representative of the effective atomic number of silver bromide), in order to emphasize the effects of Z_{eff} at various photon energies. Mass attenuation coefficients for compounds or mixtures are calculated using Bragg's rule [Attix 1986]

$$\left(\frac{\mu}{\rho}\right)_{mix} = \sum_i \left(\frac{\mu}{\rho}\right)_i f_i \qquad 2.8$$

where f_i is the mass fraction of element i.

Bragg's rule holds equally well for $(\mu_{tr}/\rho)_{mix}$ and requires a slight modification for $(\mu_{en}/\rho)_{mix}$ such that

$$\left(\frac{\mu_{en}}{\rho}\right)_{mix} = \left(\frac{\mu_{tr}}{\rho}\right)_{mix} (1 - g_{mix}), \qquad 2.9$$

where

$$g_{mix} = \sum_i f_i g_i \ . \qquad 2.10$$

Mass energy absorption coefficients for water, Fricke gelatin and silicon are compared in Figure 2.2. The data for Fricke gel match the water data very well and it is expected that absorbed dose measurements in this material should closely represent dose in water. This is supported by Monte Carlo calculations of dose deposition in Fricke gel [Chan *et al.* 1993] calculated for 6 MV and 15 MV photon beams. For comparison in Figure 2.2, energy absorption in silicon is seen to differ substantially from that in water, particularly for photon energies below 1 MeV.

2.1.2 Electron interactions

Since electrons in motion in a medium are responsible for dose deposition through multiple interactions along their tracks, the dependence of electron interaction cross sections on the properties of the absorbing medium are important from the dosimetry point of view. The distance of closest approach (or impact parameter, b) of the electron to a target atom determines the type of interaction that will take place. If $b >> a$ where a is the classical electron radius of the atom, soft collisions with atomic electrons will result in small deflections and small energy losses. For $b \sim a$, hard or knock-on collisions are likely, where the target electron is ejected from the atom. As a result of hard collisions, energetic electrons can carry energy away from the incident electron tracks, as well as cause characteristic x-rays to be produced as the atomic vacancy is filled. Finally, for $b << a$, the electron will likely undergo elastic collision with the nucleus, with a change in direction but very little energy loss. A small percentage (2-3%) of the time during a close encounter with the nucleus, the electron will be decelerated and emit bremsstrahlung radiation.

The rate of energy loss by electrons in a medium is described by the stopping power dT/dx, or mass stopping power $(1/\rho)dT/dx$, where T is the kinetic energy of the electron and x is absorber thickness. The total stopping power is the sum of both collisional and radiative stopping powers and depends on the mass, charge and energy of the incident particle as well as the atomic number and density of the absorbing medium.

The mass collision stopping power for electrons is given by [ICRU 1984]

$$\left(\frac{dT}{\rho dx}\right)_c = \kappa\left[\ln\left(\frac{\tau^2(\tau+2)}{2(I/m_oc^2)^2}\right) + F(\tau) - \delta - 2\frac{C}{Z}\right], \qquad 2.11$$

which combines Bethe's formulation for soft collisions with the Moller cross section for hard collisions [Fraunfelder and Henley 1974]. A similar formula exists for positron interactions which should be considered when pair production is important. $\kappa \propto (Z/A)/\beta^2$, where $\beta = v/c$ with v being the electron speed. $\tau \equiv \frac{T}{m_oc^2}$, where m_oc^2 is the electron rest mass energy, and I is the mean ionization potential of the atoms of the absorbing material. F is a slowly varying function of electron energy only. The last two terms δ and $2C/Z$ are the density correction and shell correction, respectively, which are discussed in more detail elsewhere [Attix 1986]. The dependencies on κ, I, and C/Z lead to decreases in mass collisional stopping power for high-Z materials compared with low-Z materials. I is roughly proportional to Z with stronger dependence at low Z. Z/A and hence κ, tend to decrease slightly going to higher Z. The density of the medium becomes important when comparing gases with liquids or solids, due to the polarization effect. In condensed media, polarization of atoms near an electron track serves to reduce energy transfer to more distant atoms, reducing the overall mass collisional stopping power.

For radiobiology and microdosimetry and to some extent in dosimetry, the more relevant stopping power is the restricted mass collision stopping power, also known as the linear energy transfer (*LET*) for the charged particles produced in the medium. *LET* is that part of the mass collision stopping power which includes all soft collisions plus hard collisions for which the delta-rays (low energy electrons) produced carry away energy less than a cutoff value Δ. Δ is chosen according to the particular application. *LET*, symbolized as L_Δ, is usually expressed in keV/μm such that

$$L_\Delta = \frac{\rho}{10}\cdot\left(\frac{dT}{\rho\, dx}\right)_\Delta . \qquad 2.12$$

For compounds and intimate mixtures, mass collision stopping powers and restricted stopping powers can be calculated using Bragg's rule (given in Equation 2.8 for attenuation coefficients). Mass collision stopping powers for water, Fricke solution and radiographic film, calculated using Bragg's rule, are shown in Figure 2.3.

The bremsstrahlung interaction is analogous to reverse pair production, in that a decelerating electron in the field of a nucleus produces a photon. A similar interaction in the field of an electron is analogous to reverse triplet production [Fraunfelder and Henley 1974]. Bremsstrahlung results in radiative loss of energy away from the point of interaction and leads to reduced absorbed dose in the vicinity of the electron track. The interaction cross section for bremsstrahlung is given by the pair production cross section in Equation 2.7. Of note is the Z^2 dependence, making bremsstrahlung more important in high-Z materials for electrons.

2.1.3 Cavity theory

Given that the material properties of the dosimeter often differ significantly from the tissue in which one wishes to determine absorbed dose, a model relating dose in the dosimeter to dose in tissue must be used. Some types of dosimeter, such as ionization chambers, can be modeled using cavity theory. A sensitive volume or cavity, surrounded by a dosimeter wall, is embedded in the medium of interest. The size of the cavity determines which of several different theories must be applied. The simplest of these is the Bragg-Gray theory which can be applied when the cavity is small enough not to perturb the charged particle fluence crossing it, and all dose deposited in the cavity results from those charged particles crossing it. When the dosimeter wall is thick enough to stop all charged particles originating outside the wall, and is at least as thick as the range of secondary charged particles produced in the wall, the dose to the medium D_m is given by [Attix 1986]

$$D_m = D_g \frac{\overline{(\mu_{en}/\rho)_m}}{\overline{(\mu_{en}/\rho)_w}} \times \frac{{}_m\bar{S}_w}{{}_m\bar{S}_g} \quad , \qquad 2.13$$

where the subscripts m, w, and g refer to the medium, wall and cavity gas respectively. D_g is the dose to the cavity gas, the $\overline{(\mu_{en}/\rho)}$ are the mass energy absorption coefficients averaged over the photon energy spectrum and the ${}_m\bar{S}$ are the mass stopping powers averaged over the charged particle energy spectrum. D_g is calculated from the charge

collected, the energy required to produce an ion pair in the gas, and the mass of gas in the collecting volume. In practice some of these quantities are determined indirectly by cross calibration with a dosimetry standard such as a free-air ionization chamber.

Although the Bragg-Gray cavity theory summarized above applies mainly to gas-filled ionization chambers, the concepts required to convert any dosimeter response to dose in the medium of interest are based on similar principles. In particular, the need to match the dosimeter wall and cavity material to the medium of interest in terms of mass attenuation coefficients and stopping powers is evident. Since the energy spectra of photons and electrons in the medium at the point of measurement can only be approximated at best, the most reliable way to ensure accuracy in the dose conversion calculation is to match the dosimeter material and wall material as closely as possible to the medium in which dose is to be measured. One of the advantages of measuring dose with the MRI Fricke gelatin method is that, in the cavity theory model, the dosimeter material itself comprises the cavity, wall and medium of interest and is essentially water-equivalent in terms of density and atomic number.

2.2 NMR relaxation theory

Nuclear magnetic resonance (NMR) was first discovered in 1946 [Bloch *et al.* 1946, Purcell *et al.* 1946] and has rapidly developed as a technique for probing the properties of materials at the molecular level. Almost three decades after the discovery of NMR the possibility of spatially encoding the signal using magnetic gradients to produce images was pointed out [Lauterbur 1973]. Magnetic resonance imaging (MRI) has now become a useful diagnostic medical tool. The signal intensity in MRI images is dominated by processes governing the spin-lattice and spin-spin relaxation rates of the mobile water protons, and by proton density. In particular, the relaxation of water hydrating large molecules or paramagnetic centres strongly influences relaxation rates of water protons within the entire sample. It is these properties that allow the distinction to be made between various tissue types within the body as well as between diseased and normal tissues. Changes in some of these properties may be used to produce images of radiation dose distributions within materials. The fundamentals of NMR theory can be found in many good references [Abragam 1961, Slichter 1980]. The introduction given here is meant to outline basic relaxation theory as applied to the ferrous sulphate gel dosimeter.

In equilibrium at room temperature T, a population of N spin-1/2 nuclei (e.g. water protons) placed in a steady magnetic field $\mathbf{B}_0$ oriented along the z axis, can be described by the Boltzmann distribution

$$\frac{N^-}{N^+} = e^{-\frac{\hbar\omega_0}{kT}} \approx 1 - \frac{\hbar\omega_0}{kT}. \qquad 2.14$$

N^+ and N^- denote the number of spins in the upper and lower energy states respectively. The lower energy state is that for which the dipole moment of the particle is aligned with the applied field $\mathbf{B}_0$, and the upper energy level is occupied by particles with dipole moments anti-aligned with $\mathbf{B}_0$. ω_0 is the Larmor frequency of precession for a nucleus immersed in $\mathbf{B}_0$ and is given by

$$\omega_0 = \gamma B_0, \qquad 2.15$$

where the gyromagnetic ratio γ is the ratio of nuclear magnetic moment μ to spin angular momentum $\hbar\mathbf{I}$. k is the Boltzman constant and $\hbar$ is Planck's constant divided by 2π.

In this equilibrium situation, due to the excess of spins aligned with $\mathbf{B}_0$, the sample will have a net magnetization $\mathbf{M}_0$ in the z-direction. To first order, $\mathbf{M}_0$ is given by

$$\mathbf{M}_0 = N\gamma^2\hbar^2 I(I+1)\frac{\mathbf{B}_0}{3kT} = \chi_0\mathbf{B}_0, \qquad 2.16$$

where χ_0 is the static nuclear susceptibility of the material.

A system of such spins may be excited by application of a transverse magnetic field $\mathbf{B}_1$ rotating at angular frequency ω,

$$\mathbf{B}_1(t) = B_1(\cos(\omega t)\hat{\mathbf{i}} - \sin(\omega t)\hat{\mathbf{j}}) , \qquad 2.17$$

where $\hat{\mathbf{i}}$ and $\hat{\mathbf{j}}$ are unit vectors in the x and y directions in the laboratory frame. The vector sum of $\mathbf{B}_1$ and $\mathbf{B}_0$ forms the effective magnetic field $\mathbf{B}_{eff}$. It is often convenient to view the system from the frame of reference rotating at the $\mathbf{B}_1$ frequency ω, this frame denoted by the subscript ρ. Along the z_ρ direction (which coincides with the z direction), the static field is reduced to B_0-ω/γ. When the resonance condition $\omega = \omega_0$ is satisfied, the static field in the rotating frame vanishes. As a result, in the rotating frame $\mathbf{B}_{eff} = \mathbf{B}_1$, and $\mathbf{M}_0$ precesses about $\mathbf{B}_1$ at frequency γB_1. The degree of peturbation can be controlled by the amplitude and duration of the applied radiofrequency (RF) pulse. By choosing B_1 and t appropriately, $\mathbf{M}_0$ can be brought to lie along the y_ρ axis. An RF pulse satisfying these conditions is termed a 90° pulse. Similarly a 180° pulse is one that inverts $\mathbf{M}_0$ such that it lies along the $-z_\rho$ direction. Upon removal of the perturbation pulse, the spin system will relax back to equilibrium with time constants characteristic of the material.

Although quantum mechanical treatment of a system of spins is required to fully describe both excitation and relaxation effects [Abragam 1961], the phenomenological equation introduced by Bloch in 1946 summarizes the excitation and relaxation processes for systems that are highly mobile at a molecular level, such as liquids. The Bloch equation states

$$\frac{d\mathbf{M}}{dt} = \gamma\mathbf{M}\times\mathbf{B} - \{M_x\hat{\mathbf{i}} + M_y\hat{\mathbf{j}}\}/T2 - \{M_z - M_0\}\hat{\mathbf{k}}/T1 . \qquad 2.18$$

Here $\mathbf{M}$ is the net magnetization created by the alignment of nuclear spins, $\mathbf{B} = \mathbf{B}_1 + \mathbf{B}_0$, where $\mathbf{B}_1$ is the magnetic field associated with the excitation pulse, $\hat{\mathbf{i}}$, $\hat{\mathbf{j}}$ and $\hat{\mathbf{k}}$ are unit vectors in the x, y and z directions respectively, and z is the longitudinal direction

determined by the main magnetic field $\mathbf{B}_0$. *T1* and *T2* are the characteristic relaxation times of the longitudinal and transverse components of the magnetization. Since the MRI dosimeter is based upon quantitation of the relaxation rate as a function of absorbed dose, a more detailed description of these relaxation processes is in order.

2.2.1 Spin-lattice relaxation

The characteristic time for recovery of $\mathbf{M}_z$ to $\mathbf{M}_0$ is known as *T1*, the spin-lattice or longitudinal relaxation time. Specifically, *T1* is the time required for $\mathbf{M}_z$ to recover to $(1/e)\ \mathbf{M}_0$, partially reestablishing thermal equilibrium between the spin system and the lattice. The lattice refers to a quantum mechanical system, having a quasi-continuous spectrum of energy levels, associated with vibrations and rotations of all other nuclei within the sample. Spin-lattice relaxation is associated with stimulated transitions between upper and lower energy states induced by transverse electromagnetic fields fluctuating at the Larmor frequency. Such fluctuating fields result predominantly from the complex rotational and translational motions of the magnetic dipole moments associated with the nuclei, atoms and molecules of the medium. In addition to dipole-dipole coupling, other interactions are important for some spin systems. For spins > 1/2, the electric quadrupole moment can interact with fluctuations in the electric field gradient tensor. Contact interactions can play a role in the interaction between two unlike spins, such as an unpaired electron in a paramagnetic ion and a water proton, when there is a finite probability for overlap of the wavefunctions of the two particles. In addition to the main Zeeman coupling between an applied magnetic field and a nuclear spin, in a molecule a small corrective term may be required to account for a shift of the Larmor frequency of the nuclear spin due to orbital angular momentum associated with electrons in the molecule. If this chemical shift is anisotropic, under rotational tumbling of the molecule it becomes a relaxation mechanism for the nuclear spins. The spin-1/2 nuclei normally observed in MRI are the protons in water molecules, although NMR experiments are not limited to aqueous systems. Since the relaxation rate of water protons is directly affected by their molecular environment, useful information about the structure and dynamics of this environment can often be deduced from solvent proton relaxation rates.

From a system of two like spins, for example the two protons in a water molecule, the theory may be expanded to incorporate two unlike spins, for example a water proton and a unpaired electron of a paramagnetic ion. For a two-spin system, there are four possible energy eigenstates. Using ket notation, where $|-\rangle$ represents the higher

energy eigenstate with eigenvalue +1/2 and $|+\rangle$ represents the lower energy eigenstate with eigenvalue -1/2. The possible energy eigenstates may be represented as $|--\rangle$, $|++\rangle$, $|+-\rangle$, $|-+\rangle$. The possibilities for transitions between states are nicely summarized in a diagram introduced by Solomon [Solomon 1955] and reproduced in Figure 2.4. In Figure 2.4a the W's represent the transition rates between two states joined by an arrow. Evidently, the value of each W will depend on the identity of the two particles considered. The two important cases relevant to the ferrous sulphate dosimeter will be discussed below.

In the case of like spins (e.g. two water protons in bulk water), the observable longitudinal NMR relaxation rate will be proportional to the rate of change of the ensemble of both z components of spin angular momentum, $d\langle I_z + I'_z\rangle / dt$. Associating I_z with the first of the pair and I'_z with the second, we have

$$\langle I_z\rangle \propto (N^{--} + N^{-+}) - (N^{+-} + N^{++}) \qquad 2.19$$

and

$$\langle I'_z\rangle \propto (N^{--} + N^{+-}) - (N^{-+} + N^{++}) \ , \qquad 2.20$$

where the N's represent the occupation numbers of each state. Combining these and taking the time derivative one obtains

$$\mathrm{d}\langle I_z + I'_z\rangle / \mathrm{dt} = -2(W_1 + W_2)(\langle I_z + I'_z\rangle - \langle I_0 + I'_0\rangle), \qquad 2.21$$

where the time derivative of the occupation numbers in terms of the W's is obtained by reference to Figure 2.4a using the fact that $W'_1=W_1$, since the spins are identical. W_0 does not appear in Equation 2.21 since this transition does not result in a change of energy of the spin system and therefore does not contribute to longitudinal relaxation. When equation 2.21 is compared with the Bloch equation (Equation 2.18), noting that $\langle I_z + I'_z\rangle \sim M_z$ and $\langle I_0 + I'_0\rangle \propto M_0$, the longitudinal relaxation rate $R1$ is given by

$$R1 = 1/T1 = 2(W_1+W_2) . \qquad 2.22$$

In the case of unlike spins I and S (i.e. water proton and paramagnetic ion), we are only concerned with the water proton relaxation $d\langle I_z\rangle / dt$. The paramagnetic centre, having its own independent relaxation mechanisms, is negligibly affected by

interactions which induce NMR relaxation [Abragam 1961] so that $\langle S_z \rangle = \langle S_0 \rangle \cong$ constant, making $d\langle S_z \rangle / dt \cong 0$. If the proton is taken as the second of the pair in ket notation, then transitions W'_1 do not contribute to proton relaxation. Also, the W_0 transitions can now produce a change in energy of the spin system since the particles are no longer identical. Taking the time derivative of Equation 2.19, using the W's from Figure 2.4a and comparing with the Bloch equation, we have

$$R1 = W_0 + 2W_1 + W_2 = 1/T1 \quad . \tag{2.23}$$

The transition rates between states (the W's) may be determined using the density matrix approach or first order perturbation theory [Shankar 1984], by assuming that interactions leading to relaxation are only small perturbations to the main Zeeman energy levels. The transition probability per unit time between states i and j, represented by W_{ij}, is given by

$$W_{ij} = \frac{1}{\hbar^2} \left| \int_{-\infty}^{\infty} \langle m_j | \mathcal{H}(t') | m_i \rangle \exp\{-i\omega_{ij} t'\} dt' \right|^2 \quad , \tag{2.24}$$

where ω_{ij} is the frequency difference between the two Zeeman energy levels of the spins in $\mathbf{B}_0$, i.e.

$$\omega_{ij} = \frac{E_j - E_i}{\hbar} \quad . \tag{2.25}$$

Equation 2.24 is also known as Fermi's Golden Rule No. 2 [Frauenfelder and Henley 1974] for transition rates between nuclear states.

Calculation of transition rates requires specification of the interaction Hamiltonian $\mathcal{H}$ coupling the spins to the lattice. The dominant interaction is the magnetic dipole-dipole interaction, the form of which is discussed in more detail in Section 2.2.3. It is usually possible to expand the Hamiltonian $\mathcal{H}$ as a sum of products of time-independent spin operators A_k and time-dependent spatial components $F_k(t)$, as

$$\mathcal{H} = \sum_k A_k F_k(t). \tag{2.26}$$

With the Hamiltonian in this general form, Equation 2.24 can be written

$$W_{ij} = \frac{1}{\hbar^2}\sum_k |\langle m_j|A_k|m_i\rangle|^2 \int_{-\infty}^{+\infty} \langle F_k(t')F_k^*(t)\rangle \exp\{-i\omega_{ij}(t'-t)\}dt' \quad . \qquad 2.27$$

The terms

$$G_k(t'-t) = \langle F_k(t')F_k^*(t)\rangle \qquad 2.28$$

are autocorrelation functions since the F_k are random functions of time due to the rotation and translation in Brownian motion. The integral terms are then recognized as Fourier transforms of the autocorrelation functions giving the spectral density functions $J_k(\omega_{ij})$,

$$J_k(\omega_{ij}) = \int_{-\infty}^{+\infty} G_k(\tau)\exp\{-i\omega_{ij}(\tau)\}d\tau \quad , \qquad 2.29$$

where $\tau = (t'-t)$. The spectral density functions contain information about the frequencies associated with the relative motion of the interacting pairs of spins within the material. The J_k are therefore strongly related to sample temperature, structure and composition as well as resonant frequency. Autocorrelation functions are often assumed to be exponential [Abragam 1961] such that

$$G_k(\tau) = G_k(0)\exp\{\frac{-\tau}{\tau_c}\} \quad , \qquad 2.30$$

The spectral distributions are then Lorentzians

$$J_k(\omega_{ij}) = G_k(0)\frac{2\tau_c}{(1+\omega_{ij}^2\tau_c^2)} \quad . \qquad 2.31$$

The key parameter in these equations is the correlation time τ_c that characterizes the time scale of the dynamics relevant to the type of perturbation being studied, for example rotational and translational motions and electron spin relaxation of paramagnetic ions. τ_c specifies the time interval for which $F(t)$ and $F(t+\tau_c)$ become sufficiently dissimilar that they may be considered unrelated.

Using Equation 2.31 the W's are determined to be

$$W_0 = C_0\tau_c \qquad 2.32a$$

$$W_1 = C_1\left(\frac{\tau_c}{1 + \omega_0^2\tau_c^2}\right) \qquad 2.32b$$

$$W_2 = C_2\left(\frac{\tau_c}{1 + 4\,\omega_0^2\tau_c^2}\right) \qquad 2.32c$$

The C's contain all constants arising from the $G_k(0)$' s and terms in front of the integral in Equation 2.27. The relaxation rate in the case of like spins is then given by

$$R1 = 2\left[C_1\left(\frac{\tau_c}{1 + \omega_0^2\tau_c^2}\right) + C_2\left(\frac{\tau_c}{1 + 4\,\omega_0^2\tau_c^2}\right)\right]. \qquad 2.33$$

In the case of unlike spins the ω_{ij} take on values different from the like-spin case. For the W_0 transition where both spins flip in the opposite sense to one another, the net energy change ΔE is proportional to the difference in Larmor frequency for the two spins, $\Delta E = \hbar\,(\omega_{01}-\omega_{02})$. For W_1 where only the proton flips, $\omega_{ij} = \omega_{01}$, while for W_2 , where both spins flip in the same sense, the change in energy is $\hbar(\omega_{01}+\omega_{02})$. Thus

$$W_0 = C'_0\left(\frac{\tau_c}{1+(\omega_{01}-\omega_{02})^2\tau_c^2}\right) \qquad 2.34a$$

$$W_1 = C'_1\left(\frac{\tau_c}{1 + \omega_{01}^2\tau_c^2}\right) \qquad 2.34b$$

$$W_2 = C'_2\left(\frac{\tau_c}{1 + (\omega_{01}+\omega_{02})^2\tau_c^2}\right), \qquad 2.34c$$

where the C' terms are different from the C terms in Equations 2.31. $1/T1$ is then calculated from Equation 2.23.

$$R1 = C'_0\left(\frac{\tau_c}{1+(\omega_{01}-\omega_{02})^2\tau_c^2}\right) + 2\,C'_1\left(\frac{\tau_c}{1 + \omega_{01}^2\tau_c^2}\right) + C'_2\left(\frac{\tau_c}{1 + (\omega_{01}+\omega_{02})^2\tau_c^2}\right). \qquad 2.35$$

In the case of a proton (Larmor frequency ω_{01}) and paramagnetic ion (Larmor frequency ω_{02}), further simplification of Equation 2.35 can be done by noting that $\omega_{02} >> \omega_{01}$.

2.2.2 Spin-spin relaxation

Similar conceptual development of the transverse relaxation, i.e. the decay of the transverse magnetization M_{xy} to its equilibrium value, is possible, however the situation is fundamentally different from the longitudinal relaxation. Spin-spin relaxation does not require a net transfer of energy from the spin system to the lattice but only internal transfers from spin to spin, conserving energy within the spin system. Eigenstates and eigenvalues of the transverse angular momentum can be defined as

$$I_{x,y}|\alpha\rangle, \quad I_{x,y}|\beta\rangle, \quad S_{x,y}|\alpha\rangle, \quad S_{x,y}|\beta\rangle \quad . \tag{2.36}$$

The four eigenstates of the pair are then

$$|\alpha\alpha\rangle, \quad |\beta\beta\rangle, \quad |\alpha\beta\rangle, \quad |\beta\alpha\rangle \quad . \tag{2.37}$$

These are not eigenstates of the energy but rather of the transverse components of the spin operators (I_x or I_y) [Solomon 1955]. They form an orthogonal set, and transitions between them (as shown in figure 2.4 b) lead to spin-spin relaxation. In order to calculate transition rates between eigenstates of the transverse angular momentum, these eigenstates can be expanded as linear combinations of the energy eigenstates, for example

$$|\alpha\alpha\rangle = \sum_i a_i|m_i\rangle, \text{ and } |\beta\beta\rangle = \sum_j b_j|m_j\rangle \quad . \tag{2.38}$$

The transition rates, U_{ab}, between initial and final states are then calculated by the same method as the longitudinal rates using

$$U_{ab} = \frac{1}{\hbar^2}\left|\int_{-\infty}^{+\infty}\sum_{ij}\langle m_i|\,\mathcal{H}|m_j\rangle a_i b_j \exp\{-i\omega_{ij}t'\}dt'\right|^2 . \tag{2.39}$$

Again, calculation of the U's requires specification of the interaction Hamiltonian to be discussed in the next section. Transverse relaxation rates may be obtained by methods similar to those used to determine Equations 2.22 and 2.23 [Solomon 1955], resulting in

$$R2 = 2(U_1 + U_2) \tag{2.40}$$

for like spins, and

$$R2 = (U_0 + 2U_1 + U_2) \tag{2.41}$$

for unlike spins.

2.2.3 Dipole-dipole interaction

For spin-1/2 particles, the dominant interaction is between the magnetic dipole fields of the particles. The strength of the interaction depends on the dipole moments created by the spin of the particles as well as the inter-particle vector **r**. The magnetic field **b** at a position specified by **r** relative to a magnetic dipole of moment μ_I (= $\gamma\hbar\mathbf{I}$), is given by

$$\mathbf{b} = \frac{\mu_0}{4\pi r^3}[3(\mu_I \cdot \hat{\mathbf{r}})\hat{\mathbf{r}} - \mu_I] \ , \tag{2.42}$$

where $\hat{\mathbf{r}}$ is the unit vector in the direction of **r** and μ_0 is the permeability of free space. The interaction Hamiltonian for a second dipole moment μ_S (= $\gamma\hbar\mathbf{S}$) interacting with this field is

$$\begin{aligned} \mathcal{H}_D &= -\mu_S \cdot \mathbf{b} \\ &= \frac{\mu_0}{4\pi r^3}[\mu_I \cdot \mu_S - 3(\mu_I \cdot \hat{\mathbf{r}})(\mu_S \cdot \hat{\mathbf{r}})] \end{aligned} \tag{2.43}$$

From Equation 2.35 and its analogue for *R2*, the relaxation rates for water protons (spin *I*) due to dipolar interaction with spin *S* (assumed to be a paramagnetic ion) are

$$\frac{1}{T1_{dip}} = \frac{2S(S+1)\hbar^2\gamma_I^2\gamma_S^2}{15r^6}\left[\frac{3\tau_c}{1+\omega_I^2\tau_c^2} + \frac{7\tau_c}{1+\omega_S^2\tau_c^2}\right] \tag{2.44}$$

$$\frac{1}{T2_D} = \frac{S(S+1)\hbar^2\gamma_I^2\gamma_S^2}{15r^6}\left[4\tau_c + \frac{3\tau_c}{1+\omega_I^2\tau_c^2} + \frac{7\tau_c}{1+\omega_S^2\tau_c^2}\right] \tag{2.45}$$

The correlation time τ_c relevant to the dipole-dipole interaction results from three processes: relative rotation of the two spins, translational motion, and electron spin relaxation of spin *S*. Assuming exponential autocorrelation functions, the rates for these processes are additive and the fastest component of the motion will dominate.

$$\frac{1}{\tau_c} = \frac{1}{\tau_r} + \frac{1}{\tau_e} + \frac{1}{\tau_s} \approx \frac{1}{\tau_r} + \frac{1}{\tau_e} \quad . \tag{2.46}$$

Reorientation in liquids takes place on a time scale of $\tau_r \sim 10^{-11}$ s and overshadows the effects of translational motion characterized by τ_s, which occurs on the order of 10^{-5} s [Koenig and Brown 1984]. These processes are highly dependent on sample temperature. The electron spin relaxation time τ_e is quite variable among paramagnetic species and can range from $\sim 10^{-9}$ s to $\sim 10^{-12}$ s. τ_e also increases with frequency according to

$$\tau_e = \tau_{e0}(1 + \omega_s^2 \tau_v^2) \quad , \tag{2.47}$$

where τ_v is a frequency-independent parameter typically $\sim 10^{-11}$s and τ_{e0} is the electron spin relaxation time at zero frequency [Koenig and Brown 1984].

2.2.4 Contact interaction

The contact interaction is important when there is a finite possibility of spatial overlap of two unlike spins, as in the case of a water proton closely attached to a paramagnetic ion. Here the perturbing Hamiltonian is given by

$$\mathcal{H}_C = \hbar A \, \mathbf{I} \cdot \mathbf{S} \quad . \tag{2.48}$$

The coupling constant A must be empirically determined, usually from measurements of the proton frequency shift resulting from the interaction.

$\mathcal{H}_C$ can again be written according in the form of Equation 2.26, where the spin operators are A_k and the lattice operators are F_k. Autocorrelation functions for electron spin relaxation are exponential (similar in form to those for rotational and translational motion) resulting in relaxation rates associated with the contact interaction given by

$$\frac{1}{T1_C} = \frac{2A^2}{3} S(S+1) \frac{\tau'_c}{1+(\omega_I - \omega_S)^2 \tau'^2_c} \qquad 2.49$$

$$\frac{1}{T2_C} = \frac{A^2}{3} S(S+1) \frac{\tau'_c}{1+(\omega_I - \omega_S)^2 \tau'^2_c} + \tau'_c \quad . \qquad 2.50$$

Since the contact interaction is isotropic, it is not affected by rotational motion of the spins. The correlation time depends only on the exchange time for water protons into and out of the inner hydration sphere of the ion, and the electron spin relaxation time, characterized by τ_s and τ_e respectively. The overall correlation time for the contact interaction (τ'_c) is given by

$$\frac{1}{\tau'_c} = \frac{1}{\tau_e} + \frac{1}{\tau_s} \quad . \qquad 2.51$$

The frequency dependence of τ_e plays an important role in the contact interaction for some paramagnetic species, resulting in *T1/T2* ratios much different from unity at high frequencies [Koenig and Brown 1984]. τ_e in paramagnetic species with non-zero orbital angular momentum (L) is usually very short due to spin-orbit coupling, making the contact interaction important mainly for L = 0 paramagnetic species such as the Fe^{3+} ion.

2.2.5 Relaxation of water hydrating paramagnetic ions

Water protons in pure water relax rather slowly due to dipolar interactions with other water protons. Protons in water hydrating paramagnetic ions relax very rapidly due to dipolar and contact interactions discussed in Sections 2.2.3 and 2.2.4. Including both the dipolar and contact interactions, proton relaxation rates in the hydration sphere of an ion $1/T1_M$ and $1/T2_M$ are given approximately by

$$\frac{1}{T1_M} = \frac{2\mu_I^2 \mu_S^2}{15\hbar^2 r^6} \left[\frac{3\tau_c}{1+\omega_I^2 \tau_c^2} + \frac{7\tau_c}{1+\omega_S^2 \tau_c^2} \right] + \frac{2A^2}{3} S(S+1) \frac{\tau_e}{1+\omega_S^2 \tau_e^2} \qquad 2.52$$

$$\frac{1}{T2_M} = \frac{\mu_I^2 \mu_S^2}{15\hbar^2 r^6} \left[4\tau_{c+} \frac{3\tau_c}{1+\omega_I^2 \tau_c^2} + \frac{7\tau_c}{1+\omega_S^2 \tau_c^2} \right] + \frac{A^2}{3} \left[S(S+1) \frac{\tau_e}{1+\omega_S^2 \tau_e^2} + \tau_e \right] \qquad 2.53$$

Very rapid relaxation in this situation is primarily a result of the large magnetic moment of the electron, μ_S, which is approximately 658 times that of the proton, due to the ratio of electric charge to mass. In addition, the electron paramagnetic relaxation of the ion, with longitudinal relaxation rate $1/\tau_e$, provides an additional pathway to relaxation not available in bulk water.

2.2.6 Fast exchange in Fricke gel systems

Fricke gels provide at least three different environments between which water protons may migrate. These include bulk water, paramagnetic ion hydration, and hydration of the macromolecules of the gelling agent. If the exchange rate is rapid in comparison with the relaxation rates in each environment, the net water proton relaxation rate will be a weighted sum of the inherent relaxation rates of water in each phase [Schreiner *et al.* 1991]

$$\frac{1}{T2} = \sum_i f_i \frac{1}{T2_i} \quad . \tag{2.54}$$

The $1/T2_i$ are inherent relaxation rates in each site and the f_i are the fractions of water protons in each site.

Combining the ion hydration sites (Fe^{2+} and Fe^{3+}), bulk water and gelatin hydration sites, the overall relaxation rate in a Fricke gel is given by

$$\frac{1}{T2} = f_w \frac{1}{T2_w} + f_g \frac{1}{T2_g} + f_{2+} \frac{1}{T2_{(2+)}} + f_{3+} \frac{1}{T2_{(3+)}} \quad , \tag{2.55}$$

where the subscripts w and g refer to bulk water and gel and the subscript M in Equation 2.52 is replaced by (2+) or (3+) for the ferrous and ferric ions respectively. The factors f_{2+} and f_{3+} are given by

$$f_{2,3+} = q \frac{[Fe^{2,3+}]}{[H_2O]} \quad , \tag{2.56}$$

where q is the water coordination of the ion representing the number of water molecules in direct contact with the ion. The molarity of water $[H_2O]$ is 55.6 moles L^{-1} and q for

both Fe^{2+} and Fe^{3+} is 6 at pH ~ 1 [Koenig and Brown 1984]. The fast exchange model has been validated for *R1* in Fricke gels by [Audet and Schreiner 1994].

Ion relaxivity $\Re 2$ is defined as the change in *R2* per mM of added ion such that

$$\Re 2 = \frac{q \cdot 10^3}{55.6}\left[\frac{1}{T2_M}\right]. \qquad 2.57$$

The difference between the ion relaxivities for Fe^{2+} and Fe^{3+} ions forms the basis for Fricke NMR dosimetry.

2.2.7 Dephasing due to frequency shift

In the presence of a paramagnetic ion, water protons experience a shift $\Delta\omega_{01}$ in their resonant frequency. The frequency shift may arise due to anisotropy in the spin *g*-factor or due to the contact interaction. When mixing of the frequency shifted spins occurs, the transverse magnetization decreases due to loss of phase coherence among the spins [Koenig and Brown 1984]. The importance of the frequency shift for transverse relaxation depends on both the main field strength which affects $\Delta\omega_{01}$, and the rate of proton exchange into and out of the region where the shift is induced.

In addition to paramagnetic ions, inhomogeneities in $\mathbf{B}_0$ also lead to dephasing of transverse magnetization. Because this type of dephasing is not related to the chemical nature of the material, but to the characteristics of the magnet itself, it is desirable to compensate for it in some way. When the field variations are static and diffusion of the spins throughout the field gradient is slow, $\delta\mathbf{B}_0$ dephasing may be reversed by a 180° flip of the magnetization. If diffusion is rapid, such as in liquid samples, dephasing will not be reversible by this method since spins will move to different $\mathbf{B}_0$ regions between pulses. Also, for intentionally-imposed gradients used for frequency encoding in the imaging process, equal and opposite gradients may be imposed prior to signal acquisition to compensate for dephasing induced by the applied gradient fields. These effects will be described in more detail in Chapter 3.

2.3 Radiation chemistry of the Fricke dosimeter

The essential chemical change induced in the ferrous sulphate dosimeter is the conversion of Fe^{2+} to Fe^{3+} in proportion to dose. Detailed descriptions of the radiation chemical reactions are available in the literature [Swallow 1973]. Oxidation of ferrous ions is brought about by indirect effects of radiation, predominantly via the radical intermediates e_{aq}, H , OH and hydrogen ions formed during the radiolysis of water. Molecular products H_2 and H_2O_2 are also important. The main equations summarizing the oxidation processes are [Swallow 1973]

$$\begin{aligned} &Fe^{2+} + OH \rightarrow Fe^{3+} + OH^- \\ &H + O_2 \rightarrow HO_2 \\ &Fe^{2+} + HO_2 \rightarrow Fe^{3+} + HO_2^- \\ &HO_2^- + H^+ \rightarrow H_2O_2 \\ &Fe^{2+} + H_2O_2 \rightarrow Fe^{3+} + OH + OH^- \end{aligned} \qquad 2.58$$

The net yield of Fe^{3+}, $G(Fe^{3+})$, is given by

$$G(Fe^{3+}) = 2G(H_2O_2) + 3G(H) + G(OH) \quad , \qquad 2.59$$

where $G(x)$ represents the radiation chemical yield of the individual radiolysis product x. Although the radiation chemical yield given in moles J^{-1} is formally correct in terms of SI units, the G value given in ions $(100\ eV)^{-1}$ is often quoted for historical reasons.

The importance of oxygen for the production of Fe^{3+} is evident from Equations 2.57. Under well oxygenated conditions, $G(Fe^{3+}) = 15.6 \pm 0.2$ ion $(100\ eV)^{-1}$ whereas in the absence of oxygen, the ferric ion yield drops to approximately 8.1 ion $(100\ eV)^{-1}$ [Fricke and Hart 1966]. Trace organic impurities can lead to spontaneous oxidation of Fe^{2+} resulting in unreliable Fe^{3+} yields and reduced shelf-life of Fricke solution. Addition of NaCl to the solution helps to eliminate instability due to trace organic impurities but results in a slight dose rate dependence at very high dose rates [Fricke and Hart 1966].

The sensitivity of the technique is limited by the small yield of Fe^{3+}. This may be enhanced by doping the solution with organic acids or alcohols which set up chain oxidation reactions. It has been demonstrated [Geisselsoder *et al.* 1963] that the addition of benzoic acid enhances the yield by a factor of four over the standard Fricke solution. Radical production on agarose gelling agent in the ferrous sulphate gel

dosimeter is also known to enhance the yield of Fe^{3+} [Olsson 1991]. For systems with enhanced Fe^{3+} yields, both oxygen and Fe^{2+} will be depleted more rapidly, and dose response curves will saturate more quickly than for undoped ferrous sulphate dosimeter solution.

The dose range may be extended in a variety of ways. The linearity in response drops off at high doses either due to depletion of oxygen, depletion of Fe^{2+} or both. With continuous reoxygenation and increased initial [Fe^{2+}] to 50 mM, the linear dose range may be extended to 10^4 Gy. Under these conditions it has been reported that the Fe^{3+} yield is constant to 40% oxidation of the ferrous ion [Fricke and Hart 1966]. The linear dose range may also be extended to higher doses (at the expense of raising the minimum detectable dose) by intentionally decreasing $G(Fe^{3+})$. This may be done by adding cupric sulphate to the ferrous sulphate solution resulting in a decrease in yield to 0.66 ions/100eV at pH 2. Using this dosimeter solution the linear dose range may be extended to 10^5 Gy. Energy, dose rate, and temperature effects have also been extensively studied [see references in Fricke and Hart 1966].

The fraction x of Fe^{2+} converted to Fe^{3+} is given in terms of the G value as

$$x = \frac{\Delta M}{M} = \frac{D \cdot G \cdot \rho}{9.65 \times 10^6} \quad . \qquad 2.60$$

M is the initial molarity of the Fe^{2+} ion, ΔM is the molarity change induced by radiation, D is the absorbed dose in Gy, G is given in Fe^{3+} ions $(100\ eV)^{-1}$ and ρ is the density of the material in kg m^{-3}.

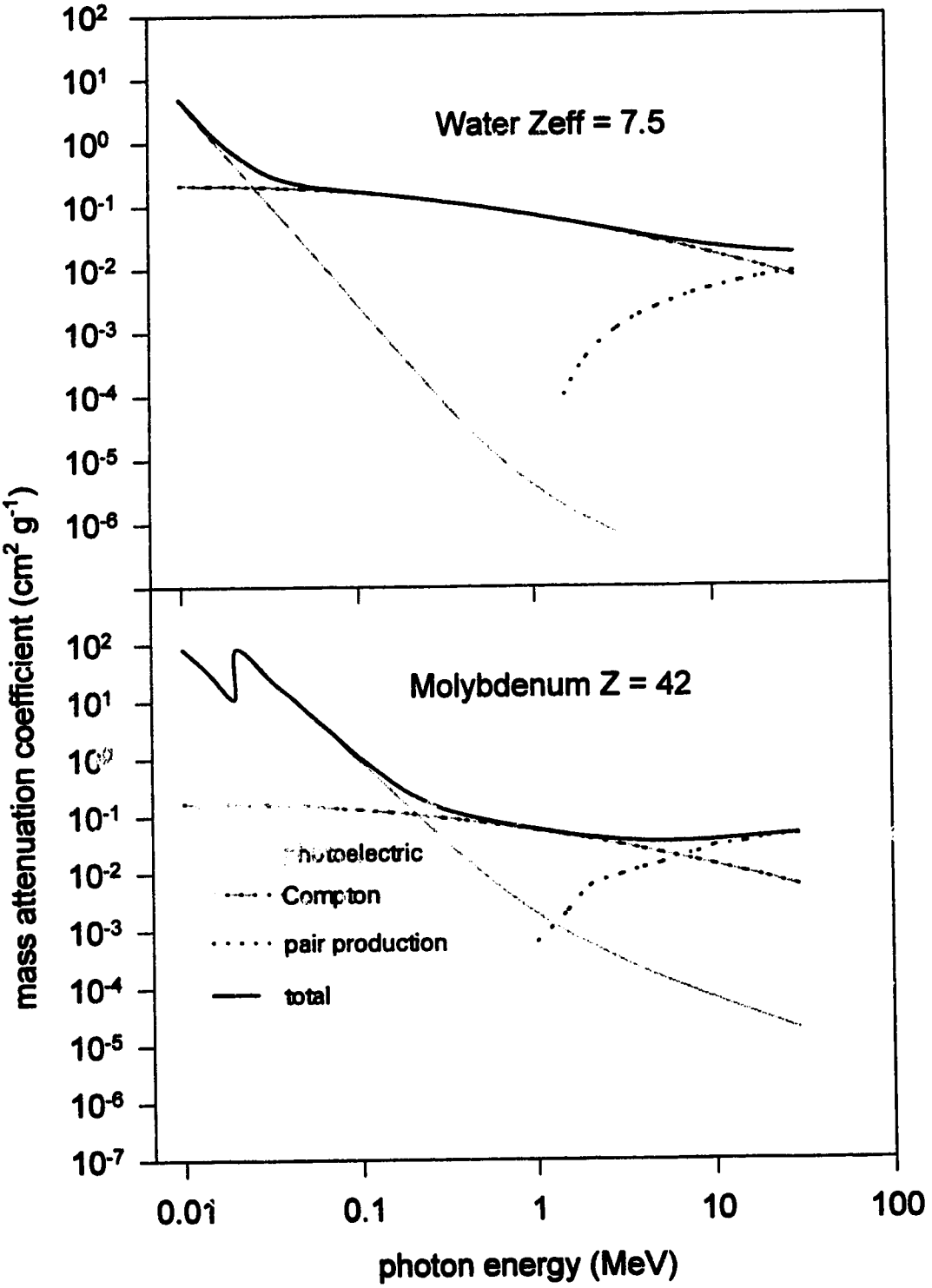

Figure 2.1 Mass attenuation coefficients for water and molybdenum. Data were taken from [Hubbell 1969].

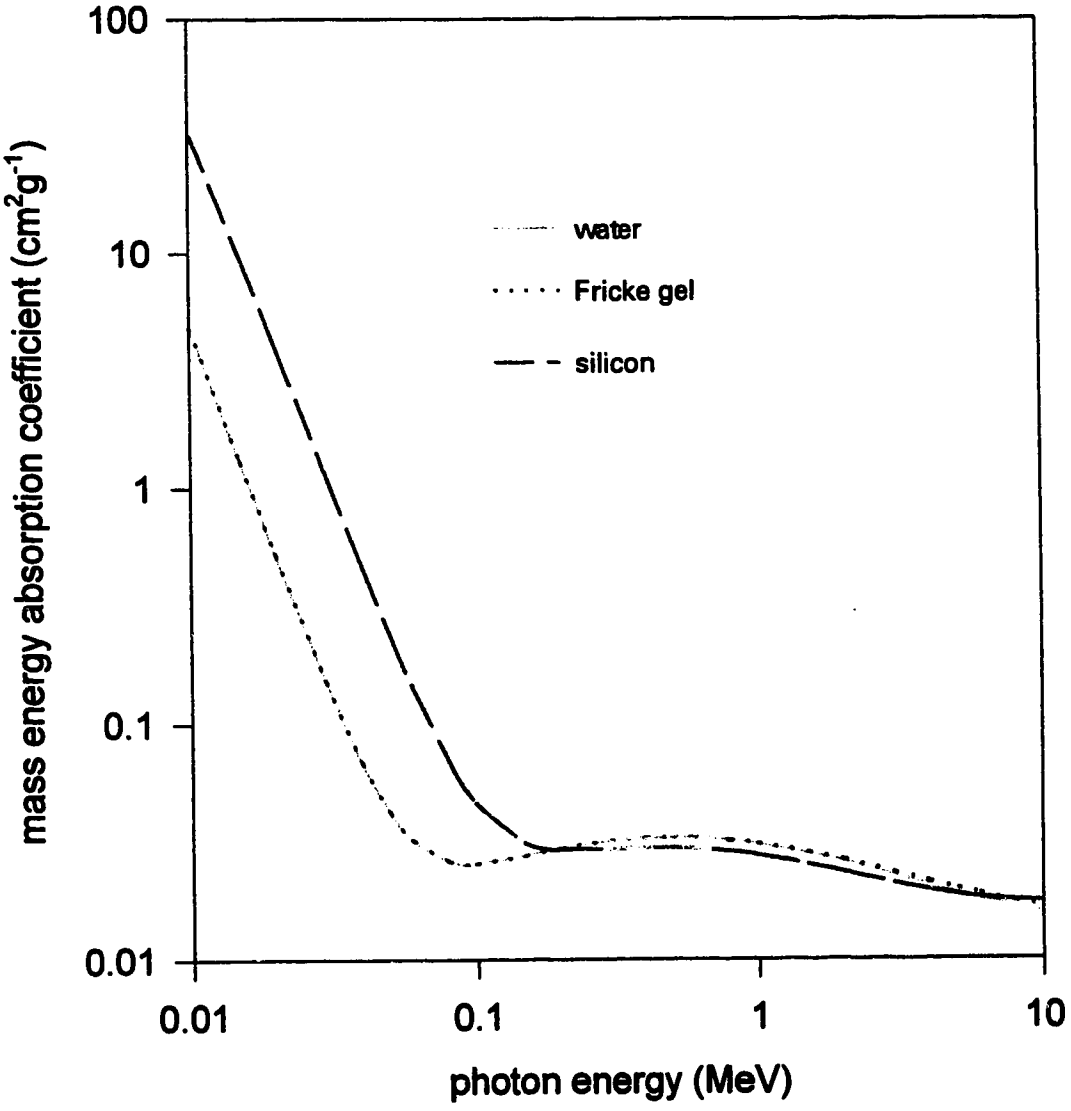

Figure 2.2 Mass energy absorption coefficients for water, Fricke gel and silicon. Data were taken from [Hubble 1969]. Fricke gel data was calculated according to Bragg's rule using 4% gelatin, 0.05 MH_2SO_4 and 1mM $FeSO_4$.

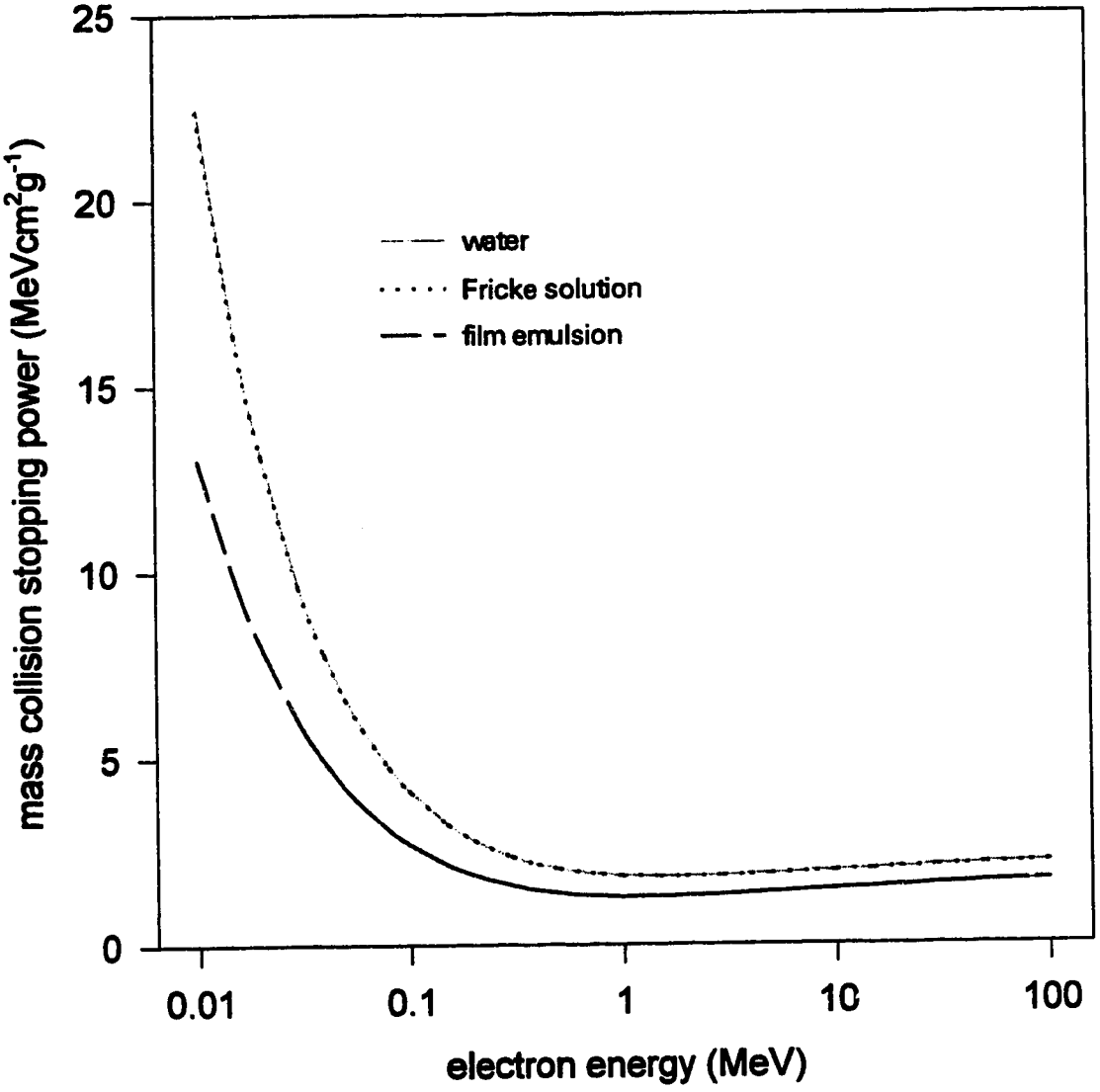

Figure 2.3 Mass collision stopping powers for water, Fricke solution and radiographic film emulsion caluculated using Bragg's rule. Data were taken from [ICRU 1984]. The Fricke solution was 1 mM $FeSO_4$, 0.4 M H_2SO_4.

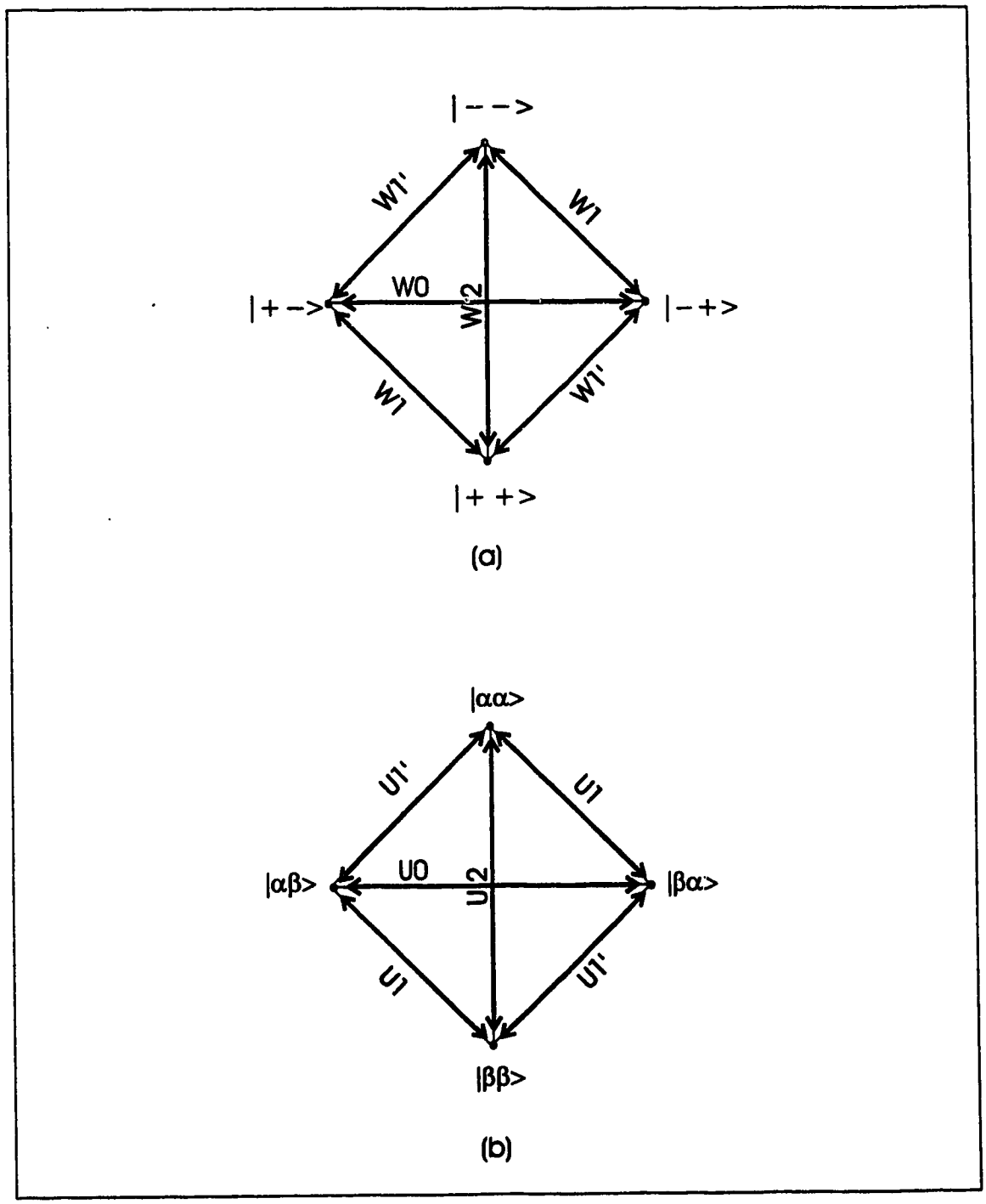

Figure 2.4 Eigenstates of the longitudinal (a) and transverse (b) angular momentum for a system of two spins. The W's and U's represent transition rates between states joined by an arrow (adapted from [Solomon 1957]).

Chapter 3

R2 measurement methodology

In this chapter, the basic techniques employed for measuring *R2* in both the spectrometer and the imaging settings are discussed, serving to introduce the reader to the pulse sequence teminology used in the remainder of the thesis. In prepartion for the discussions to follow in Chapter 5, the formation of MR images using Fourier transform methods, the effects of non-ideal RF pulses and other issues with direct bearing on image quality are discussed.

3.1 Spectrometer protocol

To measure the rate of transverse relaxation, spin echo sequences are commonly used. Figure 3.1 shows a schematic representation of the spin-echo technique. The magnetization is tipped into the transverse plane with a 90° pulse about the x-axis. Local perturbations in the main B_0 field cause adjacent spins to resonate and precess at slightly different frequencies, leading to rapid dephasing and decay of the transverse signal. The time constant associated with this fast transverse signal decay is represented by $T2^*$. To remove the effects of dephasing caused by non-uniformities associated with the magnet system, [Hahn 1950] devised a method of rephasing the spins by applying a 180° pulse after a time interval τ. As a result of the 180° pulse, the direction of phase accumulation for each spin is reversed and rephasing occurs. At a time τ following the 180° pulse, rephasing is complete and the transverse magnetization forms an echo having an amplitude representative of the true *T2* decay of the sample. Different points on the *T2* decay curve can be sampled by repeating the sequence using different values of τ. The time at which the echo appears, following the initial excitation pulse, 2τ, is represented by *TE*, while the time between successive 90° excitation pulses is the repetition time, *TR*.

The signal amplitude for a Hahn echo will be a function of the material in terms of *T1*, *T2* and proton density ρ, the timing parameters *TE* and *TR* and the properties of the receiver chain of the MRI system. In the ideal case, with negligible diffusion of the spins and perfect tip angles across the sample, the signal amplitude *S* for a Hahn echo is given by [Dixon and Esktrand 1982]

$$S(T1,T2,\rho,TE,TR) = k\rho\left[1-2e^{-\left[\frac{(TR-\frac{TE}{2})}{T1}\right]}+e^{-\left[\frac{TR}{T1}\right]}\right]e^{-\left[\frac{TE}{T2}\right]} \quad . \qquad 3.1$$

The constant k collectively accounts for system properties such as receiver coil sensitivity and amplifier gains. Normally for $T2$ estimation, long TR values are chosen to reduce the contribution from $T1$ dependent factors.

The Hahn spin echo (SE) technique only works well when the system-induced dephasing of the spins is reversible. In the presence of significant diffusion or flow of solvent protons occurring over time TE, spin dephasing due to field inhomogeneities is not reversible. Also, obtaining many points on the $T2$ decay curve is time consuming since the repetition time is ideally at least 8 $T1$ to allow adequate recovery of the longitudinal magnetization.

By applying a train of identical 180° pulses separated by time intervals 2τ during the same excitation period, the $T2$ decay curve can be sampled many times for more accurate estimation of $T2$ [Carr and Purcell 1954]. The Carr-Purcell (CP) sequence can be represented as 90x, τ, 180x, 2τ, 180x, 2τ...., where 90x represents a 90° pulse applied about the x-axis in the rotating frame. Not only does the CP sequence reduce the total scan time, but the time period during which diffusion must be negligible is reduced to the time between echoes as opposed to the time from the initial 90° pulse to the 180° pulse, as in the SE case. For multi-echo sequences, (TR-TE/2) and TR in Equation 3.1 are replaced by [TR-(N-1/2)TE] and [TR-(N-1)TE] respectively, where N is the total number of echoes, since the longitudinal recovery time is now the time between the last refocussing pulse and the next 90° pulse. The signal amplitude at echo n is given by

$$S(n,T1,T2,\rho,TE,TR) = k\rho\left[1-2e^{-\left[\frac{(TR-(N-\frac{1}{2})TE)}{T1}\right]}+e^{-\left[\frac{TR-(N-1)}{T1}\right]TE}\right]e^{-\left[\frac{nTE}{T2}\right]} \quad . \qquad 3.2$$

In Equation 3.2 ideal 90° and 180° pulses are assumed. The drawback to using the CP sequence is that small errors in the 180° pulses are cumulative and tip angles stray progressively further from 180° along the pulse train, resulting in large errors in $T2$ estimation. To help rectify this problem, it was proposed [Meiboom and Gill 1958] that the 180° pulses should be applied about the y-axis, which would still produce rephasing

but would help to compensate for the effects of imperfect tip angles. The Carr-Purcell-Meiboom-Gill (CPMG) sequence commonly used today is 90x, τ, 180y, 2τ, 180y, 2τ.... as shown in Figure 3.2. This sequence is often adequate for obtaining *T2* data from a relatively small set of echoes when monoexponential decay is expected and B_0 and RF homogeneity are good. However, when a large number of echoes is required or when B_0 and RF distortions (or phase glitches) are severe, the CPMG sequence also leads to errors in the estimation of *T2* [Hughes 1977,Vold *et al.* 1973].

Figure 3.3 illustrates how imperfect RF refocussing pulses in a CPMG sequence create a spin echo artifact. An imperfect 180° pulse at time τ splits the transverse magnetization creating an anomalous longitudinal component and two transverse components. An echo is formed at time 2τ as the main transverse component M_y refocusses. The echo is of reduced amplitude due to magnetization lost to M_x and M_z. The next imperfect 180° pulse tips a portion of the longitudinal magnetization into the transverse plane. The following 180° pulse refocusses this anomalous component as well as the main component, and the echo formed contains both correct and anomalous information. The anomalous components, known as stimulated echoes, become *T1* weighted while in the longitudinal plane and corrupt the pure *T2* dependence of the transverse echo amplitudes. The result is a baseline drift having *T1* dependence which increases in severity with the number of echoes and degree of tip angle imperfection. A second side effect of imperfect RF pulses is a discrepancy between even and odd signal amplitudes. This arises from the fact that anomalous transverse components partially refocus with the even-numbered main echoes. This causes adjacent even and odd echo amplitudes to oscillate above and below the mean echo amplitude.

The stimulated echo problem can be largely overcome by using a phase cycling scheme and signal averaging [Menon 1991]. By alternating the 90° pulses for subsequent repetitions about the positive and negative x axis, the main echoes will alternately refocus about the positive and negative y-axis (giving rise to positive and negative signals). However, the stimulated echoes that originate in the longitudinal direction after the imperfect pulse will always refocus along the same axis. By subtracting the data in the odd numbered sequence acquisitions from the even ones, the baseline drift can be removed. The most compact version of this sequence is represented by 90x, τ, 180y, 2τ, 180y, 2τ..., 90-x, τ, 180y, 2τ, 180y, 2τ... . However, it is noted that this does not eliminate the even-odd echo discrepancy; the best success is obtained when many closely spaced echoes are used. The phase-alternated CPMG sequence described by [Menon 1991] was used for all spectrometer *T2* data acquisition for this thesis.

Additional techniques for removal of stimulated echoes have been discussed [Majumdar *et al.* 1986, Crawley and Henkelman 1987] in relation to imaging sequences. These involve the application of gradient **B** fields along the longitudinal direction just prior to and just following the RF refocussing pulses. These gradient fields serve to dephase the longitudinal magnetization which would otherwise go on to form stimulated echoes. Further discussion of such techniques follows in Section 3.3.1.

3.2 Imaging protocol

The transition is made from the spectrometer protocol to the imaging protocol by means of gradient magnetic fields $\mathbf{G}_x = (\partial B_z / \partial x)\hat{\mathbf{i}}$, $\mathbf{G}_y = (\partial B_z / \partial y)\hat{\mathbf{j}}$, and $\mathbf{G}_z = (\partial B_z / \partial z)\hat{\mathbf{k}}$ superimposed on the main magnetic field $\mathbf{B}_0$. Spatial encoding and image reconstruction in MRI are described in many references [AAPM 1992 and references contained therein]. The techniques relevant to the creation of spatial distributions of *R2* used in this study will be discussed here.

Data can be acquired either in successive two-dimensional (2D) slices or as a 3-dimensional data set. The situation is best described starting with 2D data acquisition. A basic 2D single-slice CPMG pulse sequence is shown in Figure 3.2.

3.2.1 Slice selection

By superimposing a gradient $\mathbf{G}_z$ along the direction of the main field $\mathbf{B}_0$, spins at different z locations are forced to precess at different frequencies according to

$$\omega(z) = \gamma (B_0 + G_z z) \qquad 3.3$$

If this gradient is applied during RF excitation, spins at a particular z location (slice) can be selectively excited by choice of the central frequency and bandwidth of the RF pulses. For example, if spins between z_1 and z_2 are to be selectively excited, the ideal applied pulse in the frequency domain would be a square wave centered at

$$\omega = \gamma [B_0 + G_z \frac{(z_1 + z_2)}{2}] \qquad 3.4$$

with width $\Delta\omega = \gamma|G_z|(z_2-z_1)$. The inverse Fourier transform (FT) of the pulse in the frequency domain gives the pulse shape in the time domain. For a square frequency domain pulse the ideal time domain pulse shape is the sinc-modulated pulse which in practice must be truncated, leading to some error in the slice profile. In practice single pulses are sometimes replaced by composite excitation pulses in an attempt to improve slice profiles [Crawley and Henkelman 1987]. The width of the pulse in the time domain is inversely related to its bandwidth so that for very narrow frequency pulses, very long time pulses are used. In contrast, for wide frequency bands, very short (hard) pulses are used. In spin-echo sequences, the slice selection gradient is turned on only during the excitation and refocussing pulses. However, to help remove the effects of dephasing of the transverse magnetization due to the presence of the gradient, an equal and opposite gradient is often applied just following excitation, prior to the refocussing pulse.

3.2.2 Frequency encoding

Once a slice has been selectively excited, encoding in the two other orthogonal directions must be accomplished. By application of a gradient G_x along the x-axis during the signal acquisition period, nuclei in the excited slice will be forced to precess at different frequencies according to

$$\omega(x) = \gamma(B_0 + G_x x) \tag{3.5}$$

Precession of the magnetization induces a signal in the receiving coil, varying at the precessional frequency. The detected signal will be composed of a range of frequencies from magnetizations at different x locations given by

$$\gamma(B_0 + G_x x-) \le \omega \le \gamma(B_0 + G_x x+) \tag{3.6}$$

where $x-$ and $x+$ indicate the upper and lower boundaries of the sample in the x-direction. The signal acquired in the time domain can be represented by an integral over all frequencies arising from the sample,

$$\begin{aligned} S(t) &= \gamma G_x \int_{x-}^{x+} A(x)\exp\{-i\gamma(B_o + G_x x)t\}dx \\ &= \gamma G_x \exp(i\gamma B_o t)\int_{x-}^{x+} A(x)\exp(-i\gamma G_x x t)dx \end{aligned} \tag{3.7}$$

When this signal is demodulated to remove the carrier frequency γB_0, it is recognized as the FT of the function $A(x)$ with the conjugate variable $k_x = (1/2\pi)\gamma G_x t$.

Taking the inverse FT of $S(t)$ one obtains the amplitude of the signal as a function of the x location

$$A(x) = \int_{t-}^{t+} S(t)\exp(i2\pi k_x x)dk_x \quad . \qquad 3.8$$

Since frequency encoding is applied during signal acquisition, the x direction is referred to as the readout direction. $t+$ and $t-$ are the upper and lower time limits of the sampling window, chosen to include all frequencies arising from the sample. Any signal at frequencies outside the sampling window (defining the field of view, FOV) will appear aliased at lower frequencies (lower x positions) in the image. Dephasing induced by the readout gradient can be compensated for by applying G_x for half the sampling time prior to the 180° retocussing pulse so that rephasing will be complete at the center of the sampling interval.

3.2.3 Phase encoding

In order to encode the y-dependence of the signal, a technique similar to frequency encoding is used, with the gradient now applied prior to readout. The y gradient is applied for a time interval T to shift the relative phases of spins at different y locations, and removed prior to readout. The demodulated signal is now

$$S(t,T) = \int_{y-}^{y+}\int_{x-}^{x+} A(x,y)\exp(-i\gamma G_y yT)\exp(-i\gamma G_x xt)dxdy \qquad 3.9$$

where y+ and y– are the upper and lower boundaries of the sample in the y-direction. Equation 3.9 is recognized as the two-dimensional FT of the function $A(x,y)$ with the conjugate variables

$$k_x = (\gamma/2\pi)G_x t \qquad 3.10a$$

$$k_y = (\gamma/2\pi)G_y T \qquad 3.10b$$

representing the spatial frequency content in the image. The variables x, y, k_x and k_y are actually discrete and in practice the integration signs are replaced with summation signs. $A(x,y)$ can be recovered by performing the discrete 2D inverse FT of the demodulated signal. The 2D FT is separable into summations over k_x and k_y independently, enabling calculation by successive applications of a 1D FT. MRI images are created by repeating the acquisition sequence for different values of k_y to sample k-space line by line. The value of k_y is fixed by switching G_y to correspond to a particular line in k-space prior to signal acquisition. The signal then produces one line in the pre-image matrix. A matrix is constructed from successive rows each acquired for a different value of k_y by changing the gradient G_y until k-space has been adequately sampled. Small values of k correspond to slowly varying intensity changes whereas large values represent sharp edges or boundaries in the image. A 1D FT is now performed first on the rows, then on the columns of this pre-image matrix to reconstruct the final image.

Three-dimensional volume data acquisition is accomplished by performing phase encoding in the z direction instead of slice selective excitation. A three-dimensional matrix is built up from repetitions of the imaging sequence performed for different G_z and G_y values. The 3D FT is then accomplished by successive applications of a 1D FT along the x,y, and z directions.

T2 can be calculated from the envelope formed by the echo amplitudes of a multiple spin-echo sequence. The characteristic timing parameters of this sequence are again *TE*, the spacing between echoes, and *TR*, the spacing between successive 90° excitation pulses. The suitability of Equation 3.1 to imaging echo amplitudes has been discussed by Hardy *et al.* 1985]. Since the minimum number of repetitions required to produce an image equals the number of lines in the image (m), the minimum imaging time is equal to m x *TR*. Therefore, a compromise between total imaging time and *T2* integrity in the image intensity must often be made.

3.3 Imaging artifacts affecting *T2* determination

3.3.1 Stimulated echoes

As discussed in Section 3.1, the formation of stimulated echoes due to variations in tip angle across a sample inhibit accurate determination of *T2* from a multi-spin echo sequence. In the imaging regime this problem is more severe than in the spectrometer case for several reasons. Sample volumes in imaging are usually much

larger than in spectroscopy and therefore RF attenuation within the sample can become significant [Bottomley and Andrew 1978]. Using a semi-infinite planar phantom model, the magnetic induction **B** in an LIH (linear, isotropic, homogeneous) medium must satisfy the wave equation

$$\nabla^2\mathbf{B} - \varepsilon\mu\frac{\partial^2\mathbf{B}}{\partial t^2} - \frac{\mu}{\rho}\frac{\partial\mathbf{B}}{\partial t} = 0 \qquad 3.11$$

where ε is the permittivity, μ the permeability and ρ the resistivity of the medium. If the phantom is subjected to a sinusoidal magnetic induction field (i.e. excitation pulse),

$$\mathbf{B}(x \geq 0) = B_0 \exp(i\omega t)\hat{\mathbf{z}} \qquad 3.12$$

then within the medium

$$\mathbf{B}(x \geq 0) = B_0 \exp[-K_I x + i(\omega t - K_R x)]\hat{\mathbf{z}}. \qquad 3.13$$

K_R and K_I are the real and imaginary parts of the wave number in the medium. K_R represents $2\pi/\lambda$, where λ is the RF wavelength, and gives rise to a change in phase with position in the material. $1/K_I$ is the distance over which the amplitude of the field is attenuated by a factor $1/e$ (the skin depth of the material). K_R and K_I are given by

$$\begin{aligned} K_R &= \omega\left(\frac{1}{2}\varepsilon\mu\left\{\left[1+\left(\frac{1}{\rho^2\varepsilon^2\omega^2}\right)\right]^{\frac{1}{2}}+1\right\}\right)^{\frac{1}{2}} \\ K_I &= \omega\left(\frac{1}{2}\varepsilon\mu\left\{\left[1+\left(\frac{1}{\rho^2\varepsilon^2\omega^2}\right)\right]^{\frac{1}{2}}-1\right\}\right)^{\frac{1}{2}} \end{aligned} \qquad 3.14$$

Both the resistivity and relative permittivity of a medium decrease with increasing resonant frequency [Bottomley and Andrew 1978], contributing to a decreasing skin depth and increasing phase shift as frequency is increased. In many tissue types, the skin depth is approximately 10 cm at the 64 MHz imaging frequency used here [Bottomley and Andrew 1978]. This can have serious implications for quantitative imaging of larger samples on the order of 20 cm diameter required for external beam radiotherapy dosimetry. For example, a pulse producing a 90° angle of tip at the surface will only produce a 33° tip angle at one skin depth which occurs near the center of the sample. For a cylindrical phantom model, the variation in RF amplitude with position is less severe

than for the planar model since the curvature of the surface can produce some RF refocussing [Bottomley and Andrew 1978].

More relevant to the measurements made in this thesis is an analytic solution describing quadrature RF fields in tissue, produced by birdcage resonators [Foo *et al.* 1991]. It is demonstrated that as the body size is increased, the RF propagation characteristics are increasingly influenced by the dielectric characteristics of the body. Power deposition in the phantom is dominated by conductivity (skin depth effects) at some body sizes and permittivity at other body sizes. It is expected that for Fricke gels having a high conductivity (owing to both ferrous ions and sulphuric acid), RF attenuation for medium to large size phantoms would be quite severe. This has been demonstrated [Maryanski *et al.* 1994], with the tip angle at the centre of a 20 cm diameter phantom being reduced to less than 25% of the tip angle near the surface.

The sensitivity pattern of the RF coil also determines the uniformity of tip angle across the sample. In imaging, large samples occupying a large fraction of the coil volume can extend into regions of inhomogeneous coil sensitivity. Examples of coil sensitivity patterns for a birdcage resonator typical of the body and head coils used in this thesis are found in [Schenk 1992]. In most cases, it should be possible to ensure that the phantom lies within the most homogeneous volume of the coil.

Not only are the causes of stimulated echoes more numerous in imaging than in spectroscopy, but they produce more severe *T2* distortion in the final calculated *T2* image [Zur *et al.* 1987, Majumdar *et al.* 1986, Crawley and Henkelman 1987, Fransson *et al.* 1993]. Since a stimulated echo originating from longitudinal magnetization will have seen one less refocussing 180° pulse than the main echo, a phase difference of 180° exists between the main echo and stimulated echo at the time of refocussing. The image reconstruction algorithm interprets two signals 180° out of phase to lie at $+y$ and $-y$ locations. The stimulated echo image is therefore manifest as a *T1* weighted ghost image mirrored about the phase encoding direction and superimposed on the main image. The main echo image intensity is also correspondingly reduced. Signals arising from different parts of the image are therefore reconstructed at the same location, mixing *T2* and *T1* information from different pixels. Also, the stimulated echo superimposed on the n^{th} main echo contains signal originating from the $(n-2)^{th}$ main echo, so that the spatially reversed echo is also temporally displaced. It is readily seen why imperfect tip angles throughout the phantom can seriously inhibit the quantitative determination of *T2* from multi-echo imaging sequences.

Several techniques can be employed to remove stimulated echoes from multi-echo imaging sequences. As mentioned at the end of Section 3.1, this can be done

by judiciously applying "crusher" gradients along the *z* direction before and after the 180° refocussing pulses. Since the *z*-gradients will have no effect on the magnetization of interest in the transverse plane, they induce a phase shift only for those components of magnetization returning to or coming from the longitudinal direction, which are the source of *T1*-weighted stimulated echoes. The induced phase shifts prevent the stimulated longitudinal magnetization from refocussing to form an echo at the correct time once it is returned to the transverse plane by subsequent imperfect 180° pulses.

Phase cycling the 90° and 180° RF pulses as described in Section 3.1 is also effective in imaging. With the use of quadrature coils an intentional phase shift simulates the addition or subtraction of even and odd signal acquisitions required to cancel stimulated echoes [Graumann *et al.* 1986]. Evaluation of the phase alternation phase shift (PHAPS) technique is discussed by [Fransson *et al.* 1993].

A third technique to eliminate stimulated echo artifacts is to avoid the use of multi-echo sequences altogether by doing a single Hahn echo within each repetition interval. This technique would suffer the same limitations as described in Section 3.1 for spectrometer data acquisition.

Even with the removal of stimulated echo phase artifacts, determination of *T2* will be impaired by the loss of signal from the main echoes in regions of imperfect tip angle, as well as by the even-odd echo discrepancy. Since the signal loss will vary as a function of position within the FOV, *T2* calculation on a uniform phantom will result in a non-uniform *T2* distribution, with shorter *T2*'s calculated in regions of imperfect tip angles.

The method employed in this thesis to avoid the problems associated with imperfect tip angles differs somewhat from those described above. MRI dosimetry requires the measurement of changes in $1/T2$ as opposed to absolute *T2* values. The new approach to accurately measuring changes in $1/T2$, introduced in this thesis, will be described in detail in Chapter 5.

3.4 Signal to noise considerations

The minimum detectable dose in MRI dosimetry can be defined as the dose required to cause a change in *R2* ($\Delta R2$) equal to 3 standard deviations of the noise level in the final calculated $\Delta R2$ distribution. Assuming that the random noise is Gaussian distributed, this gives a >99% probability that the variation in *R2* is not due to background noise. It is therefore essential that the noise in each echo of the sequence is

kept to a minimum in order that the noise propagation throughout the *R2* calculation remain within reasonable limits.

The intrinsic signal-to-noise ratio (*SNR*), ψ_I, is the ratio of the signal (per unit volume) to the electrical noise from random, thermally-generated noise currents within the entire sample. In addition, losses in the RF coil and additional noise from the amplifier and receiving chain contribute to the overall noise. ψ_s represents the *SNR* (per unit volume) taking into account the hardware induced noise [Edelstein *et al.* 1986]. Since the noise in NMR images comes from electronic sources, it is independent of pixel size, while the signal is proportional to pixel size. This is quite different from other imaging modalities such as x-ray CT or SPECT (single photon emission tomography) where the noise in any pixel is proportional to the square root of the signal (the signal or number of events being proportional to pixel area). If the matrix size is doubled (say from 256^2 to 512^2) in CT for example, SNR_{512} is reduced to 1/2 SNR_{256} while in MRI, SNR_{512} is reduced to 1/4 SNR_{256}. This clearly has strong implications for the choice of image acquisition parameters.

The noise voltage spectral density υ_s arising from heat dissipation in the sample is given (in V^2/Hz) by the Johnson noise formula [Edelstein *et al.* 1986]

$$\upsilon_s^2 = 4R_s kT \quad , \tag{3.15}$$

where k is Boltzman's constant and T is the absolute temperature. The sample resistance $R_s \propto \omega^2 \propto B_0^2$, and therefore $\upsilon_s \propto B_0$.

The signal S induced in the receiver coil depends on the precession of the magnetization such that

$$S \propto \frac{d\mathbf{M}}{dt} \propto \omega M \tag{3.16}$$

where **M** is the magnetization. Since both M and ω are proportional to B_0, the signal is proportional to B_0^2. Thus ψ_I is proportional to B_0 and $\psi_s \cong \psi_I$ at high frequencies where coil losses are small [Edelstein *et al.* 1986].

To obtain the total *SNR* for a voxel in the final image, ψ_s must first be multiplied by the voxel size. Voxel size is given by the pixel area A times the slice thickness t. In addition, the *SNR* will be proportional to the square root of the total number of times the data is sampled. The total number of samples is given by the

product of the number of lines in the image, N, the sampling time, T_s, and the number of signal averages of the entire image, *NEX*. The voxel *SNR* is therefore given by

$$SNR = \psi_s At\sqrt{N}\sqrt{T_s}\sqrt{NEX} \quad . \qquad 3.17$$

From Equation 3.17, increasing the voxel size is the most efficient way to increase the *SNR*, however this obviously may compromise the spatial resolution in the image.

3.5 Geometric distortion

There are several potential sources of geometric distortion in MRI including linear scale errors in the gradient fields, inhomogeneities in the main field, chemical shifts, $\mathbf{B}_0$ eddy currents, gradient non-linearities and magnetic susceptibility variations in the object being imaged [Sumanaweera *et al.* 1993]. The first four of these can generally be minimized with correct calibration and setup of the system. The chemical shift is not an issue when dealing with homogeneous gels of the type used here. The last two are generally the more severe causes of geometric distortion in MRI.

Gradient field non-linearities in 2DFT MRI can have two side effects. In the transverse plane (plane of the slice), there can be some systematic warp in the image. Non-linearity in the slice selection direction results in a slice that is non-planar or potato-chip shaped. In-plane distortion can be corrected by algorithms taking into account known error fields associated with the gradients, but the potato chip effect is usually ignored [Sumanaweera *et al.* 1993].

The magnetic susceptibility associated with the sample being measured is relevant to MRI dosimetry at the air-phantom interface as well as in cases where inhomogeneities may be intentionally introduced for dosimetry purposes. The distortion arises because the field within a material of susceptibility χ is given by

$$B_0' = (1+\chi)B_0 \quad , \qquad 3.18$$

and therefore the amount a pixel shifts from its true location in the z direction (along the main field) is given by

$$\Delta z = \frac{B_0 \chi}{G_z} \quad . \qquad 3.19$$

From Equation 3.19 it is clear that for smaller gradients and stronger $\mathbf{B}_0$ fields, the measured shift for a given material will be more severe. Phantom contours (both external and internal due to inhomogeneities) can appear distorted in the z-direction and could affect image intensities through slice warping.

In light of the previous discussions, the experimental setups described in Chapters 4, 5 and 6 were designed to optimize the accuracy of measured *R2* values by minimizing artifacts and maximizing signal-to-noise ratios in both the NMR and MRI settings.

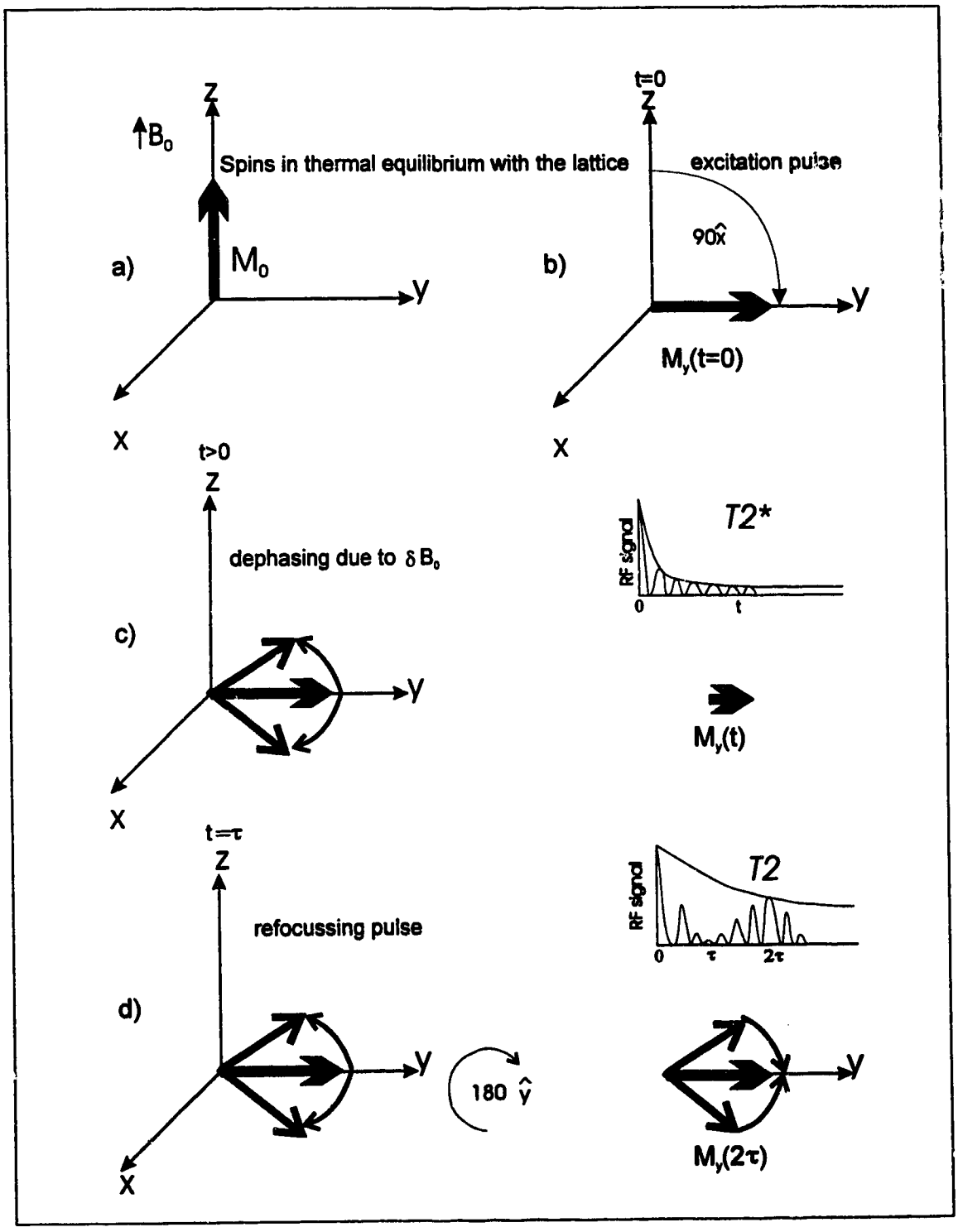

Figure 3.1 Schematic representation of the spin echo technique for measuring *T2*. The refocussing pulse shown in d) is characteristic of the CPMG sequence.

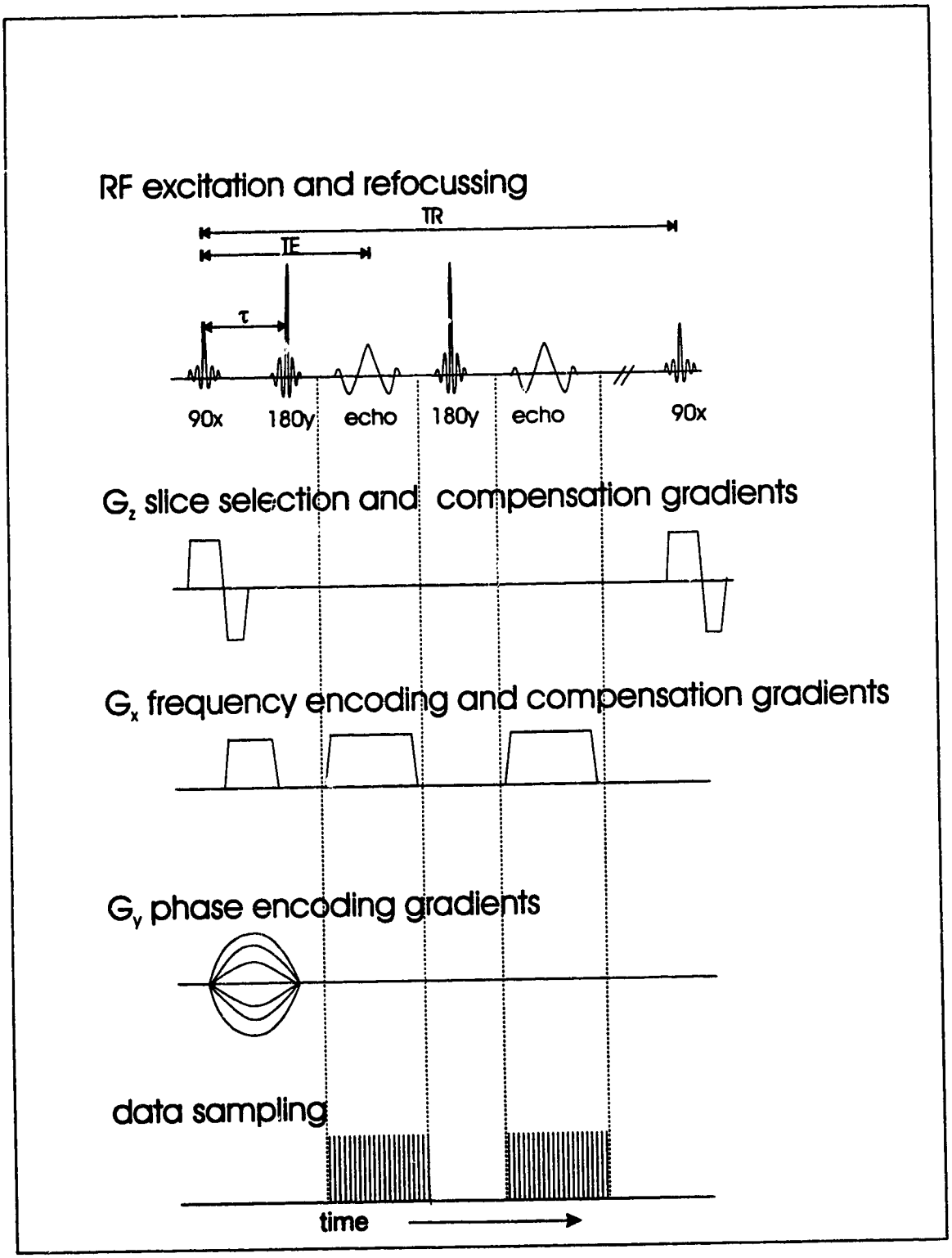

Figure 3.2 A single slice CPMG pulse sequence with imaging gradients and sampling window. Compensation gradients are applied to reverse dephasing induced by slice selection and frequency encoding gradients.

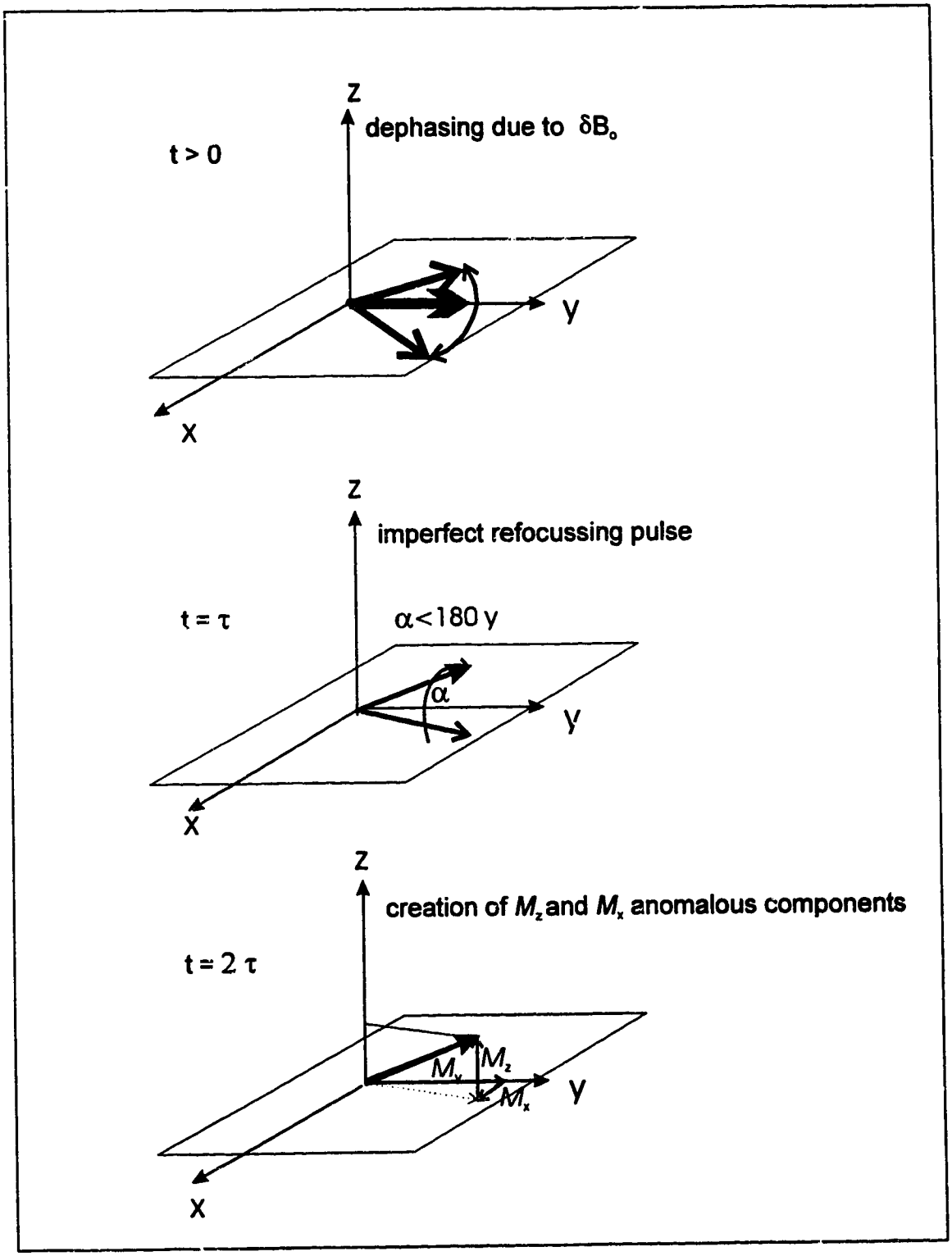

Figure 3.3 Creation of anomalous magnetization components M_z and M_x by an imperfect refocusing pulse in the CPMG pulse sequence.

Chapter 4

Experimental spin-spin relaxation rate investigation of the ferrous sulphate gelatin dosimeter[a]

In this chapter, the results of *R2* experiments designed to answer many of the questions outlined in Chapter 1 concerning the overall efficiency of the dosimeter are presented. A comparison of the frequency dependence of *R2* with that of *R1* in ferrous sulphate solutions is made. In addition, the effects of material composition on both dose response and ion diffusion in ferrous sulphate gels are explored. Data relating to sample size and temperature are also presented.

4.1. Materials and Methods

The gelatin used in this study was type A (acid cured) from porcine skin[b] (~300 bloom). All ferrous sulphate solutions were prepared using analytical reagent grades $FeSO_4$ and H_2SO_4[c] and distilled, de-ionized water. These solutions were mixed 4x final strength so that the product gel was made using 1 part ferrous sulphate solution to 3 parts gelatin solution. No NaCl was added to any of the gels used in this study. Gel preparation was carried out by soaking the required mass of gelatin powder in 3/4 of the final required volume of water at room temperature for 20 minutes until the gelatin was fully wetted. Heating and stirring at 45° C in a water bath was continued until the gel was melted. Microwave heating with intermittent stirring was subsequently found to produce gels identical to those prepared using the water bath method. Warm ferrous sulphate solution was added to the gelatin, and the gel was left undisturbed until all visible air bubbles were removed. pH was measured using a pH meter.

Irradiations were performed using 6 MV x-rays at dose rates ranging from 250 to 500 cGy min^{-1} and in some cases (see Figures 4.11 and 4.12) using an ^{192}Ir high dose rate brachytherapy source. For NMR measurements made at 100.1 MHz, borosilicate glass NMR sample tubes having a 5 mm inner diameter were filled with

---

[a] Sections of this chapter closely follow a previously published paper [Duzenli *et al.* 1994].

[b] Sigma Chemical Co.

[c] BDH Ltd.

Fricke gel and irradiated at the depth of dose maximum in a polystyrene block to provide full scatter and buildup conditions. Doses were delivered in 20 to 40 Gy fractions typically given 2 minutes apart.

NMR spin-spin relaxation times (*T2*) were measured using a Bruker 2.35 T (100.1 MHz) animal spectrometer.[a] A phase-alternated CPMG sequence [Menon 1991] with repetition time of 20 s and echo spacing of 1.6 ms with 4000 echoes was used. All relaxation curves were monoexponential down to the level of noise. Signal-to-noise ratios were typically 10^5 for gel samples in the 5 mm diameter NMR sample tubes. Measurements made at 64 MHz were carried out using a Philips 1.5 T imager[b] using a phase-alternated CPMG imaging sequence with echo spacing of 50 ms and repetition times from 2 to 3 seconds.

4.2 Frequency dependence of the dose response

Based on the dipolar terms $1/T1_{dip}$ and $1/T2_{dip}$ given in Equations 2.44 and 2.45 for proton relaxation rates in the hydration spheres of either the Fe^{3+} or Fe^{2+} ions, it was expected that dosimeter sensitivity would decrease with increasing $\mathbf{B}_0$ (and therefore increasing ω_s and ω_I). Several authors [Gore *et al.* 1984, Podgorsak and Schreiner 1992] have used the assumption that the contact interaction for both ions is negligible. This assumption is largely based on low frequency data available in the literature [Bloembergen 1957].

Using Equations 2.44 and 2.45 at a field strength of 2.35 T (100.1 MHz proton resonant frequency), the ratio of Fe^{3+} to Fe^{2+} relaxivities is predicted to be 21.3 for $\Re 1$ and 24.5 for $\Re 2$ (see Equation 2.57). The values of S are 5/2 and 4/2, leading to μ values of 5.9 μ_b and 4.9 μ_b for Fe^{3+} and Fe^{2+} ions respectively, where μ_b is the Bohr magneton. Values of τ_c were taken to be 1.5×10^{-12} s and 5.1×10^{-11} s for the Fe^{3+} and Fe^{2+} ions respectively [Gore *et al.* 1984]. A quantitative comparison of $\Re 1$ versus $\Re 2$ as a measure of dose in the Fricke dosimeter has been presented [Prasad *et al.* 1991]. However, some inconsistencies in these data (discussed later) raise questions as to the accuracy of their results. In order to help clarify the situation, the spin-lattice and spin-spin relaxivities were measured for both ions at the two available frequencies of 63.8 and 100.1 MHz. A sample of these data is shown in Figure 4.1 where the spin-spin relaxation rate is plotted as a function of increasing ion concentration. The relaxivity for each ion is

---

[a] Bruker CXP-100 Spectrometer
[b] Philips Gyroscan ACS Version 1.6

determined from the slope of the line. The experimental relaxivity data from this study as well as that available in the literature is included in Figure 4.2. It should be noted that some measurements [Gore *et al.* 1994, Vymazal *et al.* 1992] were performed at 37° C whereas all other measurements were performed at room temperature, which is assumed to be between 20° and 22° C.

For comparison, calculated relaxivities based on Equations 2.44 and 2.45 are also shown in Figure 4.2. Since the values for $1/r^6$ are not well determined, the dipolar terms have been scaled in order to match reference $\Re 1$ data of [Gore *et al.* 1984], these being $\Re 1 = 8.37\ s^{-1}\ mM^{-1}$ and $\Re 1 = 0.43\ s^{-1}\ mM^{-1}$ for Fe^{3+} and Fe^{2+} respectively, at 20 MHz. Although these measurements were performed at the higher temperature, good agreement with the $\Re 1$ data of Podgorsak and Schreiner [1991] indicates that temperature may not have a significant effect on relaxivity measurements in this range. This conjecture is also supported by the good agreement between other $\Re 2$ data of Vymazal *et al.* [1992] and the present study at 64 MHz. It is clear that the measured spin-spin relaxivity for the Fe^{3+} ion at the high frequencies studied here exceeds that predicted by the dipolar term alone. In fact a 50% to 100% enhancement in spin-spin relaxivity for Fe^{3+} over spin-lattice is observed from 64 MHz to 100 MHz. By contrast, the measured spin-lattice relaxivity for the Fe^{3+} ion and the relaxivities for the Fe^{2+} ion all agree well with the dipolar predictions.

The results of two authors [Prasad *et al.* 1991, Kron and Pope 1994] do not follow the trends of the other data presented in Figure 4.2. In the case of Prasad *et al.*, the fact that they present data showing $R1 > R2$ for the Fe^{2+} ion [see Figure 1a in Prasad *et al.*] sheds a negative light on their entire study. It is a well-established fact grounded both in theory and experiment that $R2 \geq R1$ for the same sample under the same conditions. Also, the concentrations of up to 120 mM for Fe^{2+} and 8 mM for Fe^{3+} studied by Prasad *et al.* far exceed those relevant to Fricke dosimetry. Despite these problems, the Prasad data do fall approximately within the experimental error of the other measurements. It has not been determined why the data of Kron and Pope for Fe^{3+} relaxivity is in such disagreement with the other data shown. Due to the hydroscopic nature of ferric salts, differences in water content are possible leading to discrepancies in the actual amount of ion present in a sample of a given mass. It is also noted that the ion relaxivity was measured in agarose gels as opposed to liquid. Another study [Schulz *et al.* 1990] using agarose Fricke gels showed a 30% enhancement in $R1$ sensitivity to dose at 85 MHz compared with 21 MHz although relaxivity was not measured. Increases in $R1$ at higher frequencies may be attributable to binding of the ion to the agarose macromolecule [Koenig *et al.* 1985] but at present there is insufficient evidence to draw

this conclusion. It is unfortunate that Kron and Pope chose not to study the ion relaxivity at the higher available field strength of 4.7 T (200 MHz).

In order to explain the Fe^{3+} spin-spin relaxivity data, a contact interaction contribution to $\Re 2$, based on Equation 2.50, has been fitted to the measured data. The relevant correlation time for the contact interaction is the electronic spin relaxation time for the paramagnetic ion, τ_e, which increases with frequency according to Equation 2.47, namely

$$\tau_e = \tau_{eo}(1+\omega^2\tau_v^2) \quad , \qquad 2.47$$

where τ_v is a frequency-independent parameter, typically $\sim 10^{-11}$ s, and τ_{eo} is the electron spin relaxation time at zero frequency [Koenig and Brown 1984]. A good fit to the data was obtained by setting $\tau_v = 10^{-11}$ s and $\tau_{eo} = 6.94 \times 10^{-10}$ s. The value of τ_{eo} was arrived at iteratively after fixing τ_v. A in equation 2.50 for the Fe^{3+} ion is taken to be 1.2×10^6 s^{-1} [Luz and Shulman 1965]. In addition to fitting the data from the present study, this model reproduces the frequency dependence of other *R2* data for Fe^{3+} [Vymazal *et al.* 1992] quite well above 30 MHz. It is noted that both the *R1* and *R2* data of Vymazal *et al.* at frequencies around 20 MHz appear to be shifted downwards with respect to the data of Gore *et al.* There may be some systematic difference in experimental procedure in the Vymazal study leading to this discrepancy.

The corresponding electron spin correlation times for the Fe^{3+} ion at 64 and 100 MHz based on the fit shown in Figure 4.2 are 5.5×10^{-9} s and 1.25×10^{-10} s respectively. Data in the literature for τ_e for the Fe^{3+} ion are scattered at best. The values of 4.7×10^{-11} s and 4.5×10^{-11} s for τ_e and τ_c for Fe^{3+} [Eisinger *et al.* 1962] are not consistent with a rotational correlation time of $\sim 10^{-11}$ s. A more acceptable range for τ_e is $\tau_e \geq 1.35 \times 10^{-10}$ s [Wishnia 1959]. More recently authors have quoted τ_e for Fe^{3+} as 10^{-10} - 10^{-11} s [Gore *et al.* 1992] and 10^{-9} - 10^{-10} s [Hendrick and Haake 1993]. An increasing electron spin correlation time has little effect on the dipolar terms, since the overall dipolar correlation time is dominated by rotational motion. Since *R1* is not dependent on the spectral density at zero frequency, as is *R2*, an increasing τ_e serves to decrease *R1* for the Fe^{3+} ion.

4.3 pH and gelatin concentration effects

Gelatin is one of several substances readily available as a gelling agent to stabilize the ferric ion distribution. The other commonly used agent is agarose, although the use of other synthetic polymers has also been reported [Hiraoka *et al.* 1993, deGuzman *et al.* 1989]. Gelatin was chosen because it was believed to have several advantageous properties compared with agarose. Gelatin has a relatively low melting point (~ 45° C) so that oxygen is not significantly depleted during careful phantom preparation. Agarose melts at ~ 90° C and must be reoxygenated during preparation. Also, the degrading effect of acid on gel molecules, which is enhanced by higher temperatures in agarose [Olsson 1991], should be less severe and more uniform in gelatin due to a smaller cooling rate gradient across larger phantoms.

Gelatin is produced by denaturation using one of a variety of techniques, from the natural polymer collagen, found in animal connective tissues, bone and skin. Gelatin sets via the formation of a network of relatively weak bonds, and unlike the insoluble covalent bonding found in crosslinking, the gel network is soluble in warm water. Gelatin can be made to crosslink by incorporating certain additives as used in tanning processes [Kozar 1965]. Gelatin is also a polyampholyte, acting as a base when dissolved in an acidic solvent or as an acid in a basic solvent. Since the Fricke solution is strongly acidic, it is expected that the addition of gelatin would result in increased pH of the solution. This is supported by measured data for pH vs gelatin concentration for different concentrations of sulphuric acid in a set of gels, shown on Figure 4.3. The consequences of increasing pH in the Fricke dosimeter are potentially multifold.

Increasing the pH can decrease the Fe^{3+} yield, due to the pH dependence of free radical production in water and on the gel molecules. Although the pH dependence of radical production in Fricke solution has been studied, radical production on gelatin itself, which provides a significant contribution to the total Fe^{3+} yield, must also be considered. Audet *et al.* [1994] have studied the dependence of Fe^{3+} yield in Fricke gelatin on acid concentration using spectrophotometry and *R1*.

Secondly, the relaxivity of the Fe^{3+} ion can decrease due to complexing of the ions which is known to occur at higher pH's, reducing the water coordination number of the ion. Both decreased ferric ion yield and ion complexing would reduce the sensitivity of the dose response.

A third possibility is that binding of the Fe^{3+} ions can take place at certain sites along the gelatin molecule depending on the pH conditions. This could have the effect of either increasing, by way of modification of rotational correlation times for the

ion, or decreasing, by way of reduced water proton access to the ion, the relaxivity of the ion. It is therefore difficult to predict what the net effect of ion binding would be on the dose response of the system. It has been estimated [Keller 1994], by assuming one carboxyl binding site per gelatin molecule, that binding of Fe^{3+} to gelatin should be negligible.

A potentially useful modification to the Fricke gel system is to increase the gel concentration. A stiffer gel will help maintain phantom shape when the orientation of the phantom is changed (e.g. during transport to the MRI scanner). Also, the pore size in gelatin is expected to be inversely related to gelatin concentration [Muhr and Blanshard 1982], so that the diffusion of iron ions throughout the gel may be reduced when the gelatin concentration is increased. The variation in gel structure with changes in gelatin and acid concentrations is therefore important, since the primary functions of the gel are to maintain the physical form of the phantom and reduce translational movement of the iron ions. The amino acids comprising gelatin can be hydrophilic or hydrophobic in nature due to charged or polar functional units [Veis 1964, Ward and Courts 1977]. Therefore, the forces that support the gel will depend on pH, the presence of ions and the electrolytic content of the solvent. Although a high acid concentration and low gelatin concentration might provide an enhanced dose response, these conditions could also lead to a soft gel with large pores that would not be suitable as an ion immobilization medium.

4.3.1 Gelatin hydration

Information about gelatin structure can be gained by examining how solvent proton NMR relaxation depends upon gelatin concentration and pH. In a fast exchange model [Maquet *et al.* 1989], solvent protons rapidly alternate between sites described as bulk water, bound water and structural water. It is known that in the gelled state there exist both individual gelatin molecules in random-coil configuration as well as some degree of renatured collagen-like helical structures.

Water bound to the surface of random-coil gelatin molecules or to the outer surfaces of helical structures at sites such as OH, NH_2, CO, CONH or ionic groups such as COO^- and NH^{3+}, is referred to as bound water. Bound water has a shortened relaxation time (T_b) over that in bulk water (T_w), with $T1_b \approx T2_b \approx 300$ ms [Maquet *et al.* 1989], at room temperature.

Two possible explanations have been given of the nature of structural water. Some water may be involved in the bridging bonds (network junctions) between

gelatin molecules in a helical structure. This structural water would be fairly immobile and have a very long correlation time such that $\omega_o\tau_c >> 1$. This would make the spin-spin relaxation time of the structural water ($T2_{st}$) much shorter, and the spin-lattice relaxation time much longer, than that of the bound water, thereby accounting for differences in *T1* and *T2* behaviour in gels during the setting period. An estimate of $T2_{st}$ is 0.2 ms [Maquet *et al.* 1989].

A second explanation of structural water is that growth of the gel network causes diffusion of preferentially ordered water molecules among the domains of partially-ordered gelatin macromolecules. Due to the anisotropic motion of this type of structural water, spin-spin relaxation rates would again be enhanced whereas *T1* would not be greatly affected. An estimate of the value of *T2* for this type of water is 1.5 ms [Maquet *et al.* 1989].

Regardless of the exact nature of the structural water, a three-site fast exchange model describing water proton relaxation in a gelatin gel can be proposed:

$$\frac{1}{T2_g} = \frac{(1-hc)}{T2_w} + \frac{hc}{T2_b} + (hc\chi)\left[\frac{1}{T2_{st}} - \frac{1}{T2_b}\right], \qquad 4.1$$

where c is the fractional weight of gelatin and χ is the fraction of structural water formed during the gelling process. $1/T2_w$ for the distilled, de-ionized water used here was 0.412 s^{-1}, and 0.435 s^{-1} with the addition of 0.15 M H_2SO_4. Since there is no single molecular size for gelatin but rather a distribution over a range of sizes, it is more common to refer to the mass of hydration water per gram of gelatin (h), rather than the number of hydrating water protons per macromolecule. A typical number for h is 45 g water g^{-1} [Maquet *et al.* 1989, Kozlov and Burdygina 1983]. It has been demonstrated that the fraction of helical gelatin χ increases with time during the gelling process, causing a gradual decrease in *T2* of the gel during this period. It is also anticipated that solvent pH and gelatin concentration can influence χ.

The fast exchange model was tested by measuring *R2* as a function of gelatin concentration by weight as shown in Figure 4.4. Rearranging Equation 4.1 as a function of c,

$$\frac{1}{T2_g} = \frac{1}{T2_w} + \left[\frac{1}{T2_b} - \frac{1}{T2_w} + \chi\left(\frac{1}{T2_{st}} - \frac{1}{T2_b}\right)\right]hc \qquad 4.2$$

it is evident that if χ is constant, then *R2* should increase linearly with gelatin concentration *c*. *R2* versus gelatin concentration was measured using two different solvents. For the first, de-ionized water only was the solvent. For the second, 0.15 M sulfuric acid was added to produce a pH of approximately 1.0 as required for the ferrous sulphate dosimeter. An acid concentration of 0.15 M H_2SO_4 was chosen since it produced the lowest pH for which 12% gelatin could set to a gel stiff enough to be used for large phantoms. A phantom mixture containing 12% gelatin was the maximum concentration achievable using our preparation technique.

The results in Figure 4.4 indicate that the neutral pH curve does not extrapolate to the measured relaxation rate for bulk water at zero gelatin concentration, and also deviates from linearity at higher gelatin concentrations. The amount of structural water, represented by the fraction χ, does not appear to remain constant but instead is a function of gelatin concentration. It is possible that an increasing degree of renaturation of the collagen helix is achieved at neutral pH when the inter-polymer distance is decreased as gelatin concentration increases. A second possible explanation is that the structural water is not in fast exchange but has a significant lifetime τ_{st} in the structural phase. This would lead to a modification of Equation 4.1 to read

$$\frac{1}{T2_g} = \frac{(1-hc)}{T2_w} + \frac{hc(1-\chi)}{T2_b} + \frac{hc\chi}{(1-hc\chi)}\frac{1}{(T2_{st}+\tau_{st})}, \qquad 4.3$$

[Ablett *et al.* 1978]. As *c* increases, the third term of this equation would result in non-linear behaviour of the relaxation rate as is found in some agarose gels.

The addition of 0.15 M acid to the gelatin produces a linear relationship between relaxation rate and gelatin concentration. The slope of the corresponding line from Figure 4.4 is 0.088 s^{-1} (% gelatin)$^{-1}$, and the intercept agrees with the bulk water value. This indicates that the fast exchange model with a constant fraction of structural water is adequate to describe the spin-spin relaxation behaviour of gelatin-water gels with concentrations to 12% gelatin by weight when 0.15 M H_2SO_4 is added. However at this acidity, only the 12% gelatin gel would be suitable for use as a dosimetry phantom material. Below this concentration the gels are too soft, and do not retain their shape well when the phantom orientation is changed.

The above findings could be relevant to the performance of gels in dosimetry applications. Ion diffusion rates in gels containing a significant degree of structural water (i.e. having a more rigidly constructed gel network) could differ from rates of ion diffusion in looser random-coil gelatin structures.

4.3.2 Ion relaxivity

There was some concern about how the ion relaxivities would be affected by the presence of gelatin in the gels. Ferric ions form complexes with reduced relaxivities when the pH is increased above $\Re 1$ for Fe^{3+} in solution decreases by ~ 9% when the pH is increased from 1.25 to 2 [Koenig *et al.* 1985]. Similar data for $\Re 2$ is not found in the literature, but a reduction in coordination number due to ion complexing would result in the same relative reduction in $\Re 2$ as in $\Re 1$. Studies of spin-lattice relaxivity in Fricke gelatin [Audet and Schreiner 1994] have led to the conclusion that the reduction in dose response sensitivity in gels with high gelatin concentration is due to ion complexing.

Spin-spin relaxation rate versus ion concentration for ferrous and ferric ions in solution and 12% gelatin (both with 0.15 M H_2SO_4), measured at 100.1 MHz, are shown in Figure 4.1. Similar data for 0.05 M H_2SO_4 liquid and 4% gelatin were also measured. In all cases, the relaxation rate increases linearly with ion concentration up to 1 mM. Within the accuracy of the measurements (ion concentrations accurate to ±2%), no significant difference in spin-spin relaxivity for either ion was measured for the gel samples compared with the liquid samples. Also, no significant difference between liquid samples with 0.15 M and 0.05 M H_2SO_4 was found. From these data $\Delta\Re 2$ is determined to be 13.4 ± 0.5 s^{-1} mM^{-1} for the combinations of gelatin and acid concentrations tested. This finding differs from that of Audet *et al.*[1994] who observed the spin-lattice relaxivity of Fe^{3+} to decrease with increasing gelatin concentration. Many differences including the measurement of *T1* as opposed to *T2*, different acid concentrations, different resonant frequencies and different preparation techniques could have contributed to the contrasting results. Also, Audet *et al.* [1994] systematically studied a wider range of gelatin concentrations than were studied here. In this study only those gels that were potential candidates for dosimetry in terms of gel stiffness and dose response sensitivity were tested. The intercepts of the gelatin curves in Figure 4.1 are shifted vertically by 0.9 ± 0.1 s^{-1} compared with the liquid curves. This is in good agreement with a 1.05 s^{-1} shift predicted using data from Figure 4.4.

4.3.3 Dose response curves in gels

The spin-spin relaxation rate in ferrous sulphate gelatin material will increase linearly with radiation absorbed dose provided that the presence of gelatin does not introduce spurious chemical reactions or interfere with the relaxivity of the ferric

ions. Upon irradiation, a fraction x of the ferrous ions will be converted to ferric ions. Using the fast exchange model in Equation 2.55, *R2* will be given by

$$R2 = \left\{ \frac{1}{T2_g} + f\left[\frac{1}{T2_M(2+)} - \frac{1}{T2_w} \right] \right\} + fx\left[\frac{1}{T2_M(3+)} - \frac{1}{T2_M(2+)} \right]. \qquad 4.4$$

Here f is the fraction of water protons originally hydrating ferrous ions prior to any oxidation of Fe^{2+} to Fe^{3+}. $1/T2_g$ is the relaxation rate of water protons in the gel without ferrous ions. $1/T2_M(2+)$ and $1/T2_M(3+)$ are the relaxation rates in the Fe^{3+} and Fe^{2+} hydration spheres given in Equations 2.52 and 2.53. This model assumes that water hydrating the ions comes from the bulk pool and that fast exchange of protons from the bulk water to the ionic hydration phases occurs. Also, it is assumed that the hydration numbers of both the Fe^{2+} and Fe^{3+} ions are the same. The validity of the fast exchange assumption for both ions in solution has previously been discussed [Podgorsak and Schreiner 1992] with reference to *R1*.

The fraction x is determined using Equation 2.59. The slope of the dose response curve, or sensitivity S, in $s^{-1}\,Gy^{-1}$, is then given by

$$S = (\Delta\Re 2)\cdot\frac{G\cdot\rho}{9.65\text{x}10^6}, \qquad 4.5$$

where

$$\Delta\Re 2 = \Re 2(Fe^{3+}) - \Re 2(Fe^{2+}) \qquad 4.6$$

is the difference in relaxivities between the Fe^{3+} and Fe^{2+} ions. According to Equation 4.4, the intercept of the dose response curve should increase with increasing gelatin concentration, by amounts corresponding to the data in Figure 4.3.

It is well established [Swallow 1973, Fricke and Hart 1966] that in the liquid Fricke system, lowering the pH enhances the chemical yield of Fe^{3+} ions. At higher pH's the reaction

$$Fe^{3+} + HO_2 \rightarrow Fe^{2+} + H^+ + O_2 \qquad 4.7$$

competes with the oxidation reactions, reducing the Fe^{3+} yield [Swallow 1973]. Also, the yields of intermediates H and H_2O_2, which participate in the oxidation reactions, are reduced at high pH [Swallow 1973]. The situation is complicated by the additional production of radicals on the gel molecules themselves, leading to an enhancement in the Fe^{3+} yield. This yield enhancement can also depend on the pH of the solvent. The Fe^{3+} yield can be determined from Equation 4.5 when the relaxivities and sensitivity are known. The *G* value in 5% and 10% gelatin, 0.20 M H_2SO_4 and 1 mM initial [Fe2+] has been determined to be 42 ± 1 ions $(100\ eV)^{-1}$ [Audet *et al.* 1993]. The generally accepted value for G in 0.4 M H_2SO_4 Fricke solution is 15.6 ± 0.1 ions $(100eV)^{-1}$ [Fricke and Hart 1966].

Dose response curves for various gelatin compositions are shown in Figure 4.5. The 8% and 12% gelatin curves have been shifted vertically upward by 1.0 and 3.0 s^{-1} respectively to make the curves more easily visualized. Sensitivities, densities and calculated *G* values are listed in Table 2.1. For the 12% gelatin and 0.15 M H_2SO_4 material, the calculated *G* value is in good agreement with $G = 42 \pm 1$ ions $(100eV)^{-1}$ found by Audet *et al.* [Audet *et al.* 1993]. Since the relaxivities of the ions showed no change between 0% and 12% gelatin for 0.15 M H_2SO_4, the range of sensitivities must reflect a changing *G* value. The range of *G* values may indicate that yield enhancement due to radical production on gelatin is quite sensitive to both acid and gelatin concentration. The actual intercept values for the 0.15 M H_2SO_4 dose response curves are 2.2, 2.8, and 3.6 ± 0.1 s^{-1} for 4%, 8% and 12% gelatin respectively. The shifts in the *R2* intercepts for the 8% and 12% gelatin materials relative to the 4% gelatin material are larger than the values of 0.35 and 0.70 s^{-1} predicted from Figure 4.3. This may be explained by spontaneous oxidation of Fe^{2+} during sample preparation which is more severe in the higher concentration gels (see Section 4.4.2). The uncertainty in fitting *R2* to the raw NMR data in Figure 4.5 was less than the size of the symbols on the graph. However, larger uncertainties in the data arise due to difficulties in sample preparation. For example, spontaneous oxidation effects and variations in sample size (see Sections 4.4.1 and 4.4.2) account for an uncertainty of ~ ± 3 % in sensitivity. It is possible to reduce this to ± 1% when particular attention is paid to sample size.

Table 4.1 Dose response characteristics for various gelatin and 1mM ferrous sulphate materials.

material	$S \pm 0.003$ (s^{-1} Gy^{-1})	ρ ($kg\ m^{-3}$)	$^*G \pm 3$ ions $(100\ eV)^{-1}$
0.05 M H_2SO_4, 4% gelatin	0.077	1045	55
0.15 M H_2SO_4, 4% gelatin	0.091	1055	62
0.15 MH_2SO_4, 8% gelatin	0.082	1095	54
0.15 M H2SO4, 12% gelatin	0.069	1135	44

* G values calculated using $\Delta\Re 2 = 13.4 \pm 0.5\ s^{-1}\ mM^{-1}$

4.3.4 Ion diffusion

Diffusion of ferrous and ferric ions following irradiation results in blurring of the measured dose distribution. Following irradiation, gradients in the concentration of both ions are set up. Random thermal motion of the ions then acts to wash out the gradients until a steady state of uniform concentrations of both ions is reached. Since the total number of Fe ions (Fe^{2+} + Fe^{3+}) is preserved during the radiochemical reactions, the initial gradients created for both ions are equal and opposite. However due to the more than 20 fold enhancement in relaxation rate for Fe^{3+} over Fe^{2+}, the diffusion of ferric ions dominates the blurring process.

Diffusion in gels has been the subject of many studies, particularly for application in the field of gel electrophoresis [Muhr and Blanshard 1982]. For MRI gel dosimetry, two studies have reported on determinations of ferric ion diffusion rates in agarose [Shulz *et al.* 1990, Olsson *et al.* 1992]. Both of these studies employed techniques for measuring diffusion rates for ions originating in a liquid reservoir, and either crossing or penetrating into a thin layer of the gel. For the purpose of comparing gel diffusion in the present study, the spread in a measured beam profile over time has been determined. In Figure 4.6 the measured beam penumbra created by phantom irradiation with an asymmetric 6 MV photon beam half-blocked to the central axis is shown. The measured penumbra is seen to spread out over the course of subsequent

measurements. The penumbra width (distance between the 80% and 20% level) vs post-irradiation time for various gels is plotted in Figure 4.7. From these data it is clear that with the addition of 0.15 M H_2SO_4 the gels become less efficient at limiting ion diffusion. The 12% gelatin is slightly better than the 4% gelatin in this regard. For the lower acid concentration of 0.05 M H_2SO_4, penumbral spreading occurs initially at a rate of 0.75 mm hr^{-1} and there is no significant difference between the 4% and 12% gels.

As noted by others [Olsson *et al.* 1992], ion diffusion can be modeled by convolving an initial distribution of ion concentration with a Gaussian point spread function, the width of the Gaussian being determined by the diffusion coefficient D and the time t over which diffusion proceeds. If the initial distribution is given by $C(x,t_o)$ and the Gaussian by

$$G(x,t) = \frac{1}{\sqrt{4\pi Dt}} exp^{-\frac{x^2}{4Dt}} \qquad 4.8$$

then the distribution after a time t is given by

$$C(x,t) = G(x,t) \otimes C(x,t_o) \qquad 4.9$$

where $\otimes$ indicates the convolution operation. Convolution is generally accomplished using the Fourier transform F such that $C(x,t) = F^{-1}\{F[C(x,t_o)] \cdot F[G(x,t)]\}$.

To simulate the effects of diffusion on the measured penumbra for the photon beam used in Figure 4.7 a beam profile (from diode measurements) with a 4.9 mm penumbra was used to represent $C(x,t_o)$. Convolution of this distribution with Gaussian spread functions was carried out for a time t = 2 hours post-irradiation for a range of diffusion coefficients. The penumbral width vs diffusion coefficient is plotted in Figure 4.8. Combining information from Figures 4.7 and 4.8, the penumbral spread in 4% and 12% gelatin gels with 0.05 M H_2SO_4 is consistent with a diffusion coefficient of 0.027 ± 0.005 $cm^2\ hr^{-1}$. Comparing this with the measured diffusion coefficient for Fe^{3+} ions in agarose gels, 0.019 ± .001 cm^2/hr [Schulz *et al.* 1990, Olsson *et al.* 1992, Kron *et al.* 1994], gelatin appears to offer no advantage over agarose in terms of limiting ion diffusion. However, as demonstrated by the applications in Chapter 6, the increased ion diffusion rate in gelatin does not pose a serious problem for most applications in Fricke gel dosimetry.

4.4 Oxygen and ferric ion concentration effects

It is known that the linear range of the dose response curve in both liquid Fricke and agarose ferrous sulphate gels [Podgorsak and Schreiner 1992, Olsson *et al.* 1989, Shulz *et al.* 1990] is limited by oxygen depletion at higher doses. Hydrogen atoms present in solution can either react with oxygen to form HO_2 which oxidizes Fe^{2+}, or directly oxidize Fe^{2+}. The rate constant for the reaction of hydrogen with oxygen is 2.0×10^{10} M^{-1} s^{-1} compared with 1.8×10^{7} M^{-1} s^{-1} [Swallow 1973] for the oxidation of Fe^{2+} by H. The former reaction will therefore dominate when oxygen is present. With reference to Equations 2.58, ferric ion yield is greatly enhanced in the presence of oxygen through the formation of HO_2, H_2O_2 and OH, which oxidize ferrous ions. Oxidation still takes place in the absence of oxygen via the reaction

$$H + Fe^{2+} \xrightarrow{H^+} Fe^{3+} + H_2 \quad . \qquad 4.10$$

For liquid Fricke it is known that the G value of Fe^{3+} is constant at 15.6 ± 0.2 ions $(100eV)^{-1}$ and independent of oxygen concentration for $[O_2] > 5\%$ $[Fe^{2+}]$ [Swallow 1973]. It has also been found using spectrophotometry that in a 1 mM air-saturated Fricke solution, oxygen becomes depleted when 80% of the ferrous ion has been oxidized to ferric [Fricke and Hart 1966]. Spin-lattice relaxation rate measurements on Fricke solutions [Podgorsak and Schreiner 1991] have demonstrated a linear increase in $R1$ with doses up to ~ 400 Gy, corresponding to a conversion of ~ 93% of ferrous to ferric ions. In oxygen-free Fricke solution, the G value is ~ 8.1 ions $(100eV)^{-1}$ [Fricke and Hart 1966].

When the ferric ion concentration builds up sufficiently in the absence of oxygen, hydrogen begins to reduce ferric ions to ferrous ions via the reaction

$$H + Fe^{3+} \rightarrow H^+ + Fe^{2+} \, . \qquad 4.11$$

The rate constant for this reaction is 9.5×10^{7} M^{-1} s^{-1} (at pH 2) [Swallow 1973] and therefore the process is slightly favoured over the reaction of Equation 4.10, but would not be significant in the presence of oxygen.

From the simplified summary given above, two facts emerge. First, the depletion of oxygen alone in the liquid Fricke system does not result in saturation of the dose response curve, but does reduce its slope by a factor of ~ 2. Secondly, when a

significant concentration of ferric ions has been produced and oxygen has been depleted, the dose response curve will saturate and an inflection point will be reached when ferric ion reduction occurs more rapidly than ferrous ion oxidation. The situation is significantly more complex in Fricke gels due to enhanced consumption of oxygen through reactions with the gelling agent, depletion of oxygen through heating during preparation and enhanced production of Fe^{3+} due to radical production on the gel.

4.4.1 Sample size and oxygen depletion

Oxygen depletion effects have recently been examined for gelatin ferrous sulphate [Keller 1994], where it was demonstrated that using fractionated doses, allowing oxygen diffusion into the samples between fractions, restored sensitivity at higher doses. N_2-purged Fricke gelatin showed a depressed dose response compared with aerated gels, saturating at a dose of ~50 Gy. Non-uniform oxygen distribution within gel samples arising from preparation conditions, or the exposure of a gel surface to air, will lead to an inhomogeneous dose response throughout the sample. One consequence of this is a marked dependence of the dose response curve on sample size. To investigate this effect, dose response curves were measured for two sample heights in 5 mm diameter NMR tubes. In the smaller samples the gel column was 2 mm high, and it was expected that oxygen from the air space above the gel could easily penetrate the sample during preparation and irradiation. In the set of larger samples the gel column extended the full length of the tube (~30 mm), well beyond the depth of oxygen penetration, and the signal from the bottom third of the tube was measured[a].

Dose response curves for the two sample sizes of 12% gel, 0.15 M H_2SO_4, 1 mM ferrous sulphate dosimeter are shown in Figure 4.9 The samples were prepared under normal atmospheric conditions, with no reoxygenation other than that due to diffusion of oxygen into the surface layer from the atmosphere. No dependence of dose on sample height could be ascertained from TLD powder measurements simulating the same sample sizes. The dose range was extended to 160 Gy, revealing a continuing linear relationship between *R2* and dose for the small samples up to 120 Gy. Using a G value of 44 ions $(100\ eV)^{-1}$ from Section 4.3.3, a dose of 120 Gy results in 62% conversion of Fe^{2+} to Fe^{3+}. Under ordinary laboratory conditions the concentration of oxygen in liquid Fricke in equilibrium with air is 2-3 x 10^{-4} M [Swallow 1973]. The

[a] The phase alternated CPMG sequence allows determination of R2 independent of sample size (Menon 1991) as indicated by the good agreement between R2 values for the small and large unirradiated samples.

equilibrium concentration of oxygen in the gel may differ from the equilibrium concentration in liquid depending on the partition coefficient for oxygen diffusion in gelatin. Also, oxygen reacts with gelatin and may undergo more rapid depletion in the gel. Considering these factors, the present results are quite consistent with the effects of oxygen depletion in liquid Fricke.

For the larger samples the dose response is non-linear, reaching a plateau at about 80 Gy and then descending slightly, in agreement with data for spin-lattice relaxation in 5% gels using ~ 5 mm [Audet *et al.* 1993] and ~50 mm [Hazle *et al.* 1991] sample heights. Following oxygen depletion, a steady state is reached where oxidation of ferrous ions and reduction of ferric ions occur at the same rates, resulting in a plateau in the dose response curve. The slightly negative slope beyond 120 Gy could be the result of the reaction of Equation 4.11 being favoured over that of Equation 4.10, but some other mechanism related to the presence of gelatin could also be present. For comparison, the dose response curve for 20 mL (30 mm in height) 1 mM ferrous sulphate, 12% gelatin samples measured on a 1.5 T imaging system is also shown in Figure 4.9. The effects of oxygen depletion are consistent for the two large sample curves. The fact that the slope does not go negative for the imaging samples could be a result of the plastic sample containers and larger surface area used in the imaging study, which allowed more oxygen to diffuse into the samples from the atmosphere compared with the spectrometer samples in glass NMR tubes. These results indicate that depletion of oxygen at depth in the sample plays an important role in determining the shape of the dose response curve. Unfortunately it is the large sample dose response that applies to phantom imaging situations, so that care must be taken to ensure that reproducible levels of oxygen are present throughout the gels during irradiation.

It is also noted that sample size effects have been reported for liquid Fricke [Podgorsak and Schreiner 1991]. Samples irradiated in 68 µl cells showed a 25% enhancement in dose response compared with samples irradiated in 10 ml vessels. The difference was attributed to enhanced oxidation of Fe^{2+} due to impurities from the vessel wall. Since the surface area to sample volume ratio for the smaller samples was ~ 4 x that for the larger samples, the former would have a higher impurity concentration. It is not likely that the sample size effects demonstrated in the present study are due to impurities from the sample container walls, considering that the gelatin itself provides a high impurity content. Also, intentionally introducing a small amount of organic impurity has a negligible effect on the dose response of Fricke gelatin (see Section 4.5).

An additional experiment demonstrates the relationship between sample size and dose response at high doses. By choosing a dose beyond the large sample

saturation dose, $R2$ was measured as a function of sample height. Without loss of generality the NMR sample tube can be considered to have two compartments: the top layer of the sample volume (V_A) is well aerated and responds to all doses up to 120 Gy with a constant average Fe^{3+} yield, while the less aerated lower layer of the sample (V_B) responds with a decreasing average Fe^{3+} yield as dose increases and oxygen becomes depleted. The resulting average concentrations of Fe^{3+} in the two regions are $[Fe^{3+}]_A$, and $[Fe^{3+}]_B$, respectively at a given dose. If the sample is left to equilibrate for a period of more than 12 hours after irradiation, diffusion of the ions throughout the entire volume, $V = V_A+V_B$, produces a uniform concentration of ferric ions $[Fe^{3+}]_{net}$ given by

$$[Fe^{3+}]_{net} = (V_A\,[Fe^{3+}]_A + V_B\,[Fe^{3+}]_B) / V. \qquad 4.12$$

Since the total sample volume V is varied but V_A remains constant, the above equation can be rearranged to read

$$R2_{net} \cdot h = R2_B \cdot h + h_A \cdot (R2_A - R2_B)\ , \qquad 4.13$$

where $R2_{net}$ is the final relaxation rate after equilibration, and $R2_A$ and $R2_B$ are the relaxation rates for regions A and B immediately following irradiation. V and V_A have been replaced by h and h_A, representing sample height and height of the well-aerated layer respectively. Figure 4.10 shows a plot of $R2_{net}$ versus h for samples irradiated to 120 Gy, measured 12 hours post irradiation. The data fall away from the line at a sample height of 2.5 mm, indicating that this sample was smaller than the well-oxygenated portion V_A of the larger samples. Using $R2_A = 11.0\ s^{-1}$ and $R2_B = 6.14\ s^{-1}$ from Figure 4.9, h_A is estimated from Figure 4.10 to be 3.1 mm. Based on these results, an effective depth of oxygen penetration of 3.0 ± 0.5 mm can be assigned as the depth over which the average yield of Fe^{3+} is constant up to 120 Gy. This highly sensitive layer may be the result of reoxygenation during irradiation or of higher levels of oxygen present following preparation. Due to their small size, these gel samples set quickly and were irradiated approximately 4-5 hours following preparation. If the surface layer is better oxygenated following preparation, further oxygen diffusion into the gel over time could result in a broadening of the well-oxygenated region. For large phantoms which require approximately a 12 hour setting period at room temperature, the layer of gel in equilibrium with the atmosphere would be greater than 3 mm. If the more sensitive layer is a result of reoxygenation during irradiation, then the thickness of the layer will be determined by the dose fractionation interval. One must also bear in mind that the rate of

oxygen consumption and penetration depth may depend on gelatin concentration, and that plastic phantom containers will allow oxygen penetration. To avoid enhanced sensitivity near phantom edges due to increased oxygen concentration it is therefore advisable to keep the dose as low as possible while maintaining an adequate contrast-to-noise ratio.

4.4.2 Ferric ion concentration

From Equation 2.60, assuming a constant ferric ion yield (in the presence of sufficient oxygen), the ferrous ion population will be totally depleted at a dose of

$$D = \frac{9.65 \times 10^6}{G\rho} . \qquad 4.14$$

Using G = 55 ions $(100eV)^{-1}$ and ρ = 1045 kg m^{-3} for the 4% gelatin, 0.05 M H_2SO_4 dosimeter material (see Table 2.1), the dose required to deplete the ferrous ion concentration completely would be 1.68 x 10^2 Gy. In gels, the ferric ion yield decreases with increasing dose due to oxygen depletion, thus increasing the dose required to deplete the ferrous ion population. Dose response curve inversion is shown in Figure 4.11, where change in relaxation rate has been measured around a high dose rate (HDR) ^{192}Ir brachytherapy source. The two data sets in Figure 4.11 represent relaxation rates for two different initial Fe^{2+} ion concentrations, measured along the perpendicular bisector of the source axis. Dose was calculated using the inverse square correction only (neglecting scattering and attenuation) based on a given dose of 17 Gy at a point 2 cm from the source. The dose corresponding to the maximum response is approximately 100 Gy for both curves. Depletion of the ferrous ion population is therefore not responsible for saturation and inversion of the dose response curve. If this had been the case, the 4 mM Fe^{2+} curve should have saturated at a dose equal to 4 times that required to saturate the 1 mM Fe^{2+} curve. Using a 1 mM 4% gelatin in a 6 mm thick slab cassette (to provide better aeration), a continued increase in *R2* for doses beyond 100 Gy is demonstrated in Figure 4.12. Dose response curve inflection at a dose of approximately 100 Gy in large phantoms can therefore reasonably be attributed to the synergistic effects of oxygen depletion and ferric ion reduction.

Other effects potentially contributing to changes in the dose response characteristics of Fricke gelatin very close to an HDR source are radiation damage to the gel itself and high dose rate. Radiation damage affecting *R2* in the gelatin has been assessed by irradiating the gel prepared without ferrous ion. The results showed no

measurable change in relaxation rate of the gel surrounding the ^{192}Ir catheter after a dose of 20 Gy was delivered to a point 2 cm from the source.

Dose rate effects have been documented for the liquid Fricke dosimeter [Fricke and Hart 1966]. At extremely high dose rates (~ 10^6 Gy s^{-1}) produced by pulsed electron beams, a reduction in ferric ion yield is observed. This occurs when electron tracks are produced in such close proximity that radical lifetime is reduced through inter-radical interactions, rather than radicals going on to participate in ferrous ion oxidation. The dose rates at 5 mm from the HDR sources used to obtain the data in Figures 4.11 and 4.12 were < 0.5 Gy s^{-1}, far below that required to alter the ferric ion yield in Fricke solution.

4.5 Benzoic Acid

The effects of adding benzoic acid on the dose response of the dosimeter gel are investigated here. It has been suggested [Appleby *et al.* 1987, Prasad *et al.* 1991] that the sensitivity of the ferrous sulphate gel dosimeter may be increased by addition of an organic acid. Although this has been demonstrated to work well for the liquid Fricke dosimeter [Prasad *et al.* 1991], it is not expected to have a similarly dramatic effect when the system already contains a large amount of organic impurity such as gelatin. In Figure 4.13, dose response curves are compared for 8% gelatin and liquid ferrous sulphate solutions, with and without addition of benzoic acid. The liquid dose response is enhanced by a factor of 2.3 with the addition of benzoic acid, whereas samples containing gelatin (4% and 12% gelatin samples were also measured but are not shown) show no increase in sensitivity. It is also evident that the liquid sensitivity is enhanced beyond the gel response, indicating that the gel itself may compete for radicals with the Fe^{2+} ion, although pH may also be a factor.

4.6 Spontaneous oxidation

For dosimetry purposes changes in the dose response curve due to spontaneous oxidation of Fe^{2+} are of interest, although for phantom studies ion diffusion will limit the interval between irradiation and imaging to a couple of hours. The dose response curves for ferrous sulphate gelatin 1 and 8 days after irradiation are shown in Figure 4.14. Samples were stored tightly capped to prevent dehydration, at room

temperature and shielded from ambient light. The dose response curve for ferrous sulphate solution with no gelatin showed no measurable change over the 8 day period. Increases in relaxation rates caused by spontaneous oxidation were approximately 2%, 3% and 4% per day for 4%, 8% and 12% gelatin respectively, during the first 8 days. These results are comparable to those for Fricke agarose systems [Olsson 1991, Schulz *et al.* 1990] and other measurements done on Fricke gelatin [Keller 1994]. The dose response curves closely maintain their original shape over the seven-day interval although a slight increase in the initial slope of the dose response curve is evident from the first to the second measurement. This effect has also been noted in ferrous sulphate agarose [Gambarini *et al.* 1994].

4.7 Ambient temperature

A change in temperature may often exist between the environment in which the gel is prepared and that of the MRI measurement. For example it has been observed that the bore temperature of the imager used in these studies is generally ~23° C whereas the lab temperature where the gel sets is ~ 21° C. Obviously a larger temperature discrepancy will exist if gels are set in a refrigerated atmosphere to enhance the setting rate. Temperature changes of this magnitude are known to have a negligible effect on the chemical yield in Fricke solution [Swallow 1973]. However, the effect on *R2* of changing temperature in Fricke gel is more severe. In Figure 4.15 the change in *R2* of unirradiated Fricke gel (4% gelatin, 0.05 M H_2SO_4, 1 mM Fe^{2+}) with change in temperature is shown. The 2 L phantom used in this study equilibrated from the refrigerator temperature of 5° C to the bore temperature of 23° C at a rate of 3-4 °C per hour. Measurements were done 2 days post-preparation at the 64 MHz imaging frequency over an 18-hour period. During this period a 1-2% increase in *R2* due to spontaneous oxidation would be expected, serving to partially counteract the temperature effect. The decrease in *R2* of 0.035 s^{-1} $°C^{-1}$ obtained by fitting the data in Figure 4.15 is therefore an underestimate of the effect of increasing temperature on *R2* in Fricke gelatin.

In dosimetry, where changes in dose on the order of 5% (or less) are significant, uniformity of temperature throughout the phantom is essential. Since a change in temperature of 3° C results in at least a 5% change in *R2* of unirradiated Fricke gel, care must be exercised to ensure that the phantom is maintained at the imaging temperature long enough to allow complete thermal equilibration to take place. The consequences of thermal disequilibrium of the phantom during imaging are shown in

Figure 4.16. Here, the irradiated phantom was initially imaged immediately following placement into the magnet bore and again 2 and 12 hours later. The difference in gel setting temperature and imaging temperature was ~ 3 °C. Although the effects of ion diffusion contribute to changes in profile at the beam edge, the vertical shift in profile between the first two measurements is obvious. The magnitude of the shift is also variable across the profile. There is very little shift in the $R2$ profile after the phantom remained in the bore for more than 2 hours.

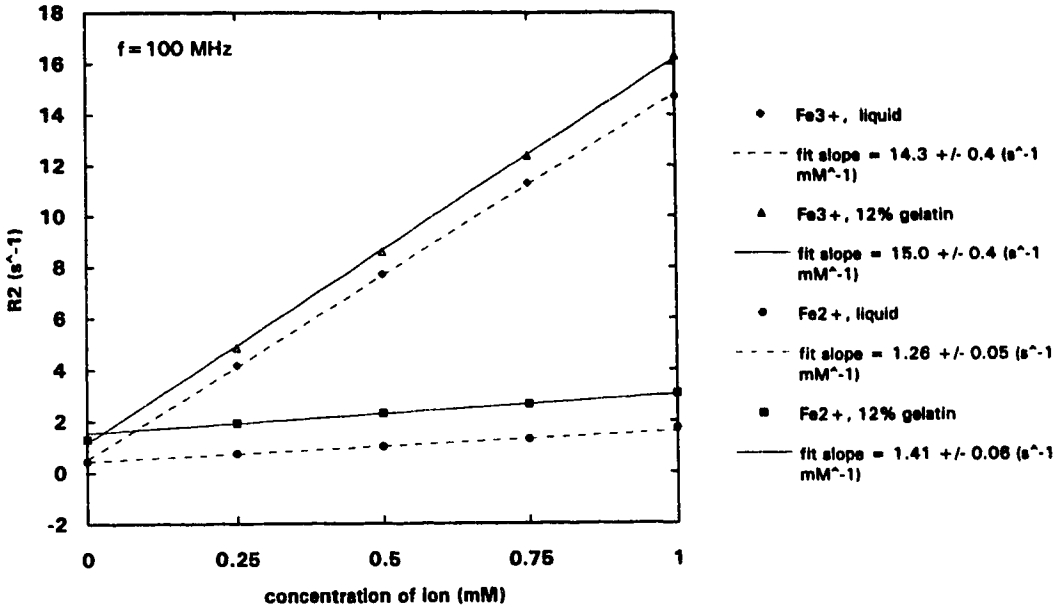

Figure 4.1 *R2* vs Fe^{2+} and Fe^{3+} ion concentrations for aqueous solution (indicated by liquid) and 12% gelatin, both with 0.15 M H_2SO_4.

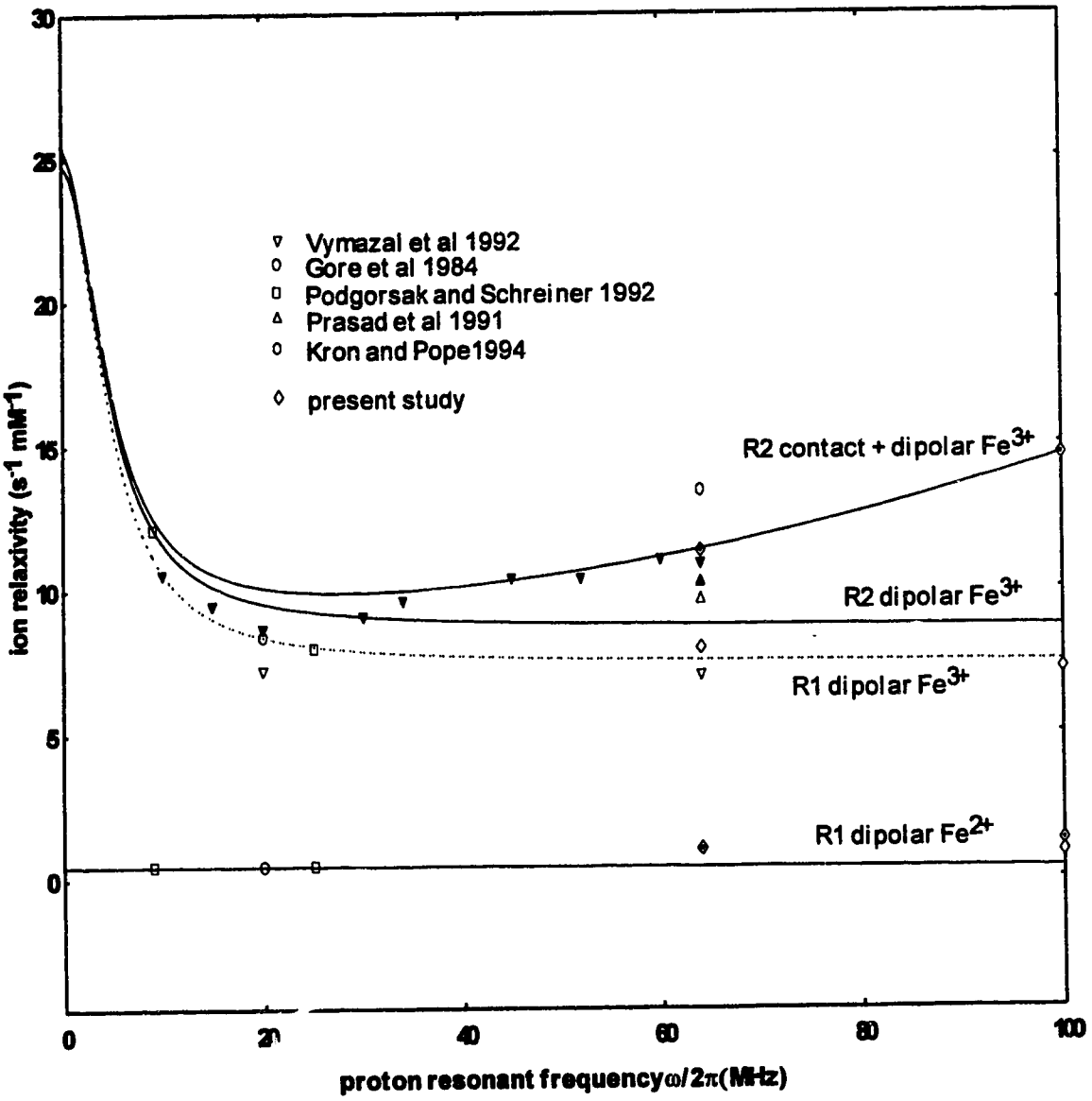

Figure 4.2 Frequency dependence of ion relaxivities for Fe^{2+} and Fe^{3+} in aqueous solution with pH ~ 1. The symbols represent measured data from various authors. Open symbols represent $\Re 1$ and symbols with a central + represent $\Re 2$. The lines are calculated using Equations 2.44, 2.45 and 2.53 with parameters given in the text.

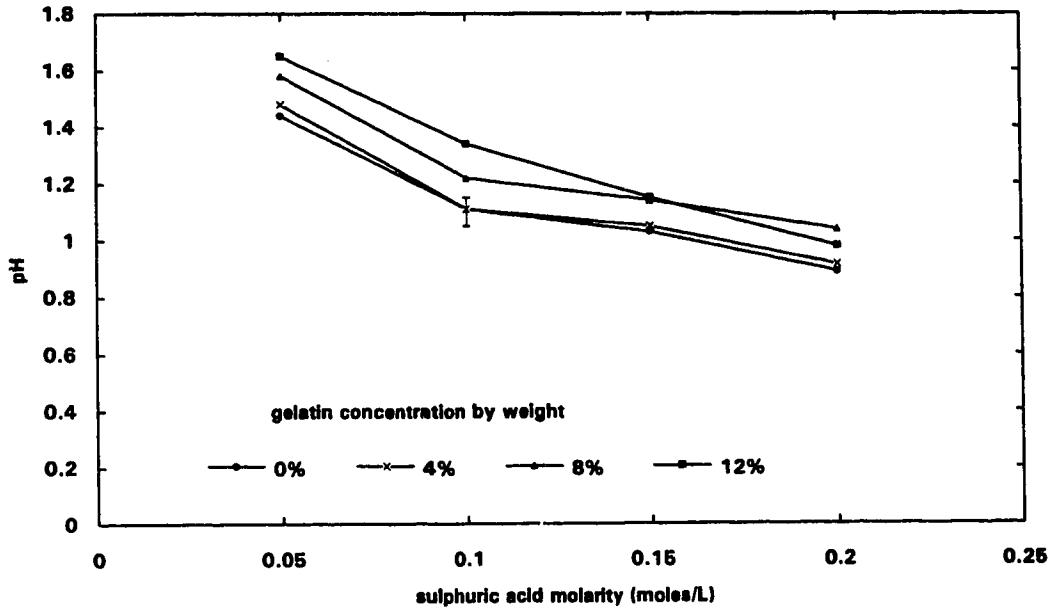

Figure 4.3 Variation in pH with gelatin and acid concentrations. Lines are drawn between data points to guide the eye. The error bar shown is representative of the error for all points on the graph.

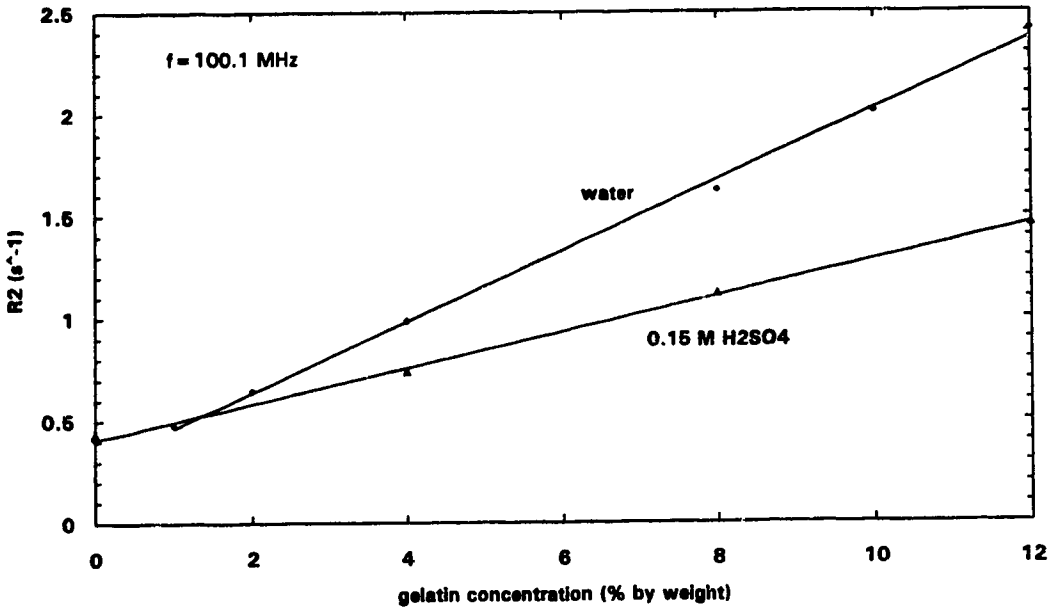

Figure 4.4 Relaxation rate versus gelatin concentration for two solvents. The data points for 0% gelatin are 0.412 s^{-1} for water and 0.435 s^{-1} for 0.15 M H_2SO_4. The water data deviates from linearity near the origin.

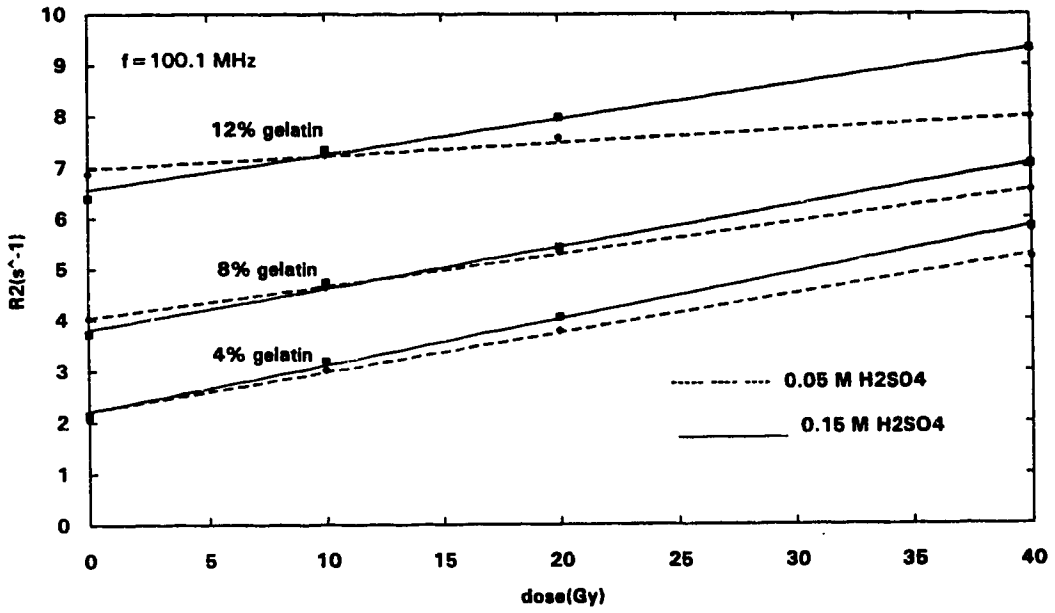

Figure 4.5 Dose response curves for various gelatin and H_2SO_4 combinations. The intercepts for the 8% gelatin and 12% gelatin curves have been shifted vertically by 1 and 3 s^{-1} to make the curves more easily visualized. The actual intercepts are 2.2, 2.8 and 3.6 s^{-1} for 4%, 8% and 12% gelatin respectively. Doses were delivered using 6 MV photons.

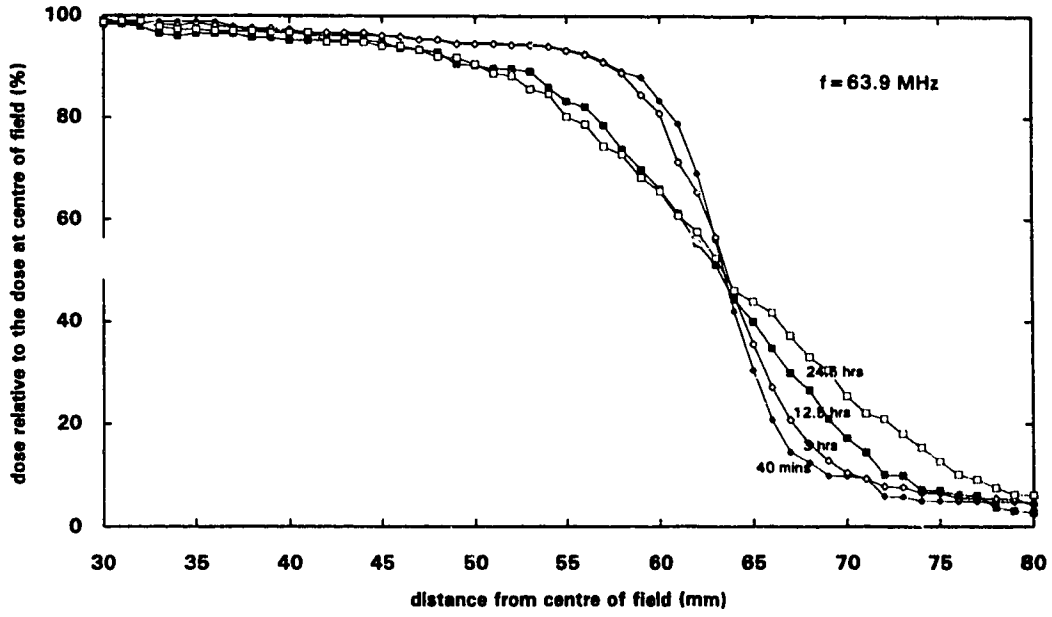

Figure 4.6 Spreading of the measured beam penumbra over time in the 4% gelatin, 0.05 M H_2SO_4 dosimeter material. Irradiation was performed using a 6 MV photon beam, half-blocked to the central axis, producing a 0.49 cm penumbra at the measurement depth of 10 cm. The surface of the phantom used for these measurements had a slight curvature, accounting for the gradual slope in the dose profile away from the centre of the field.

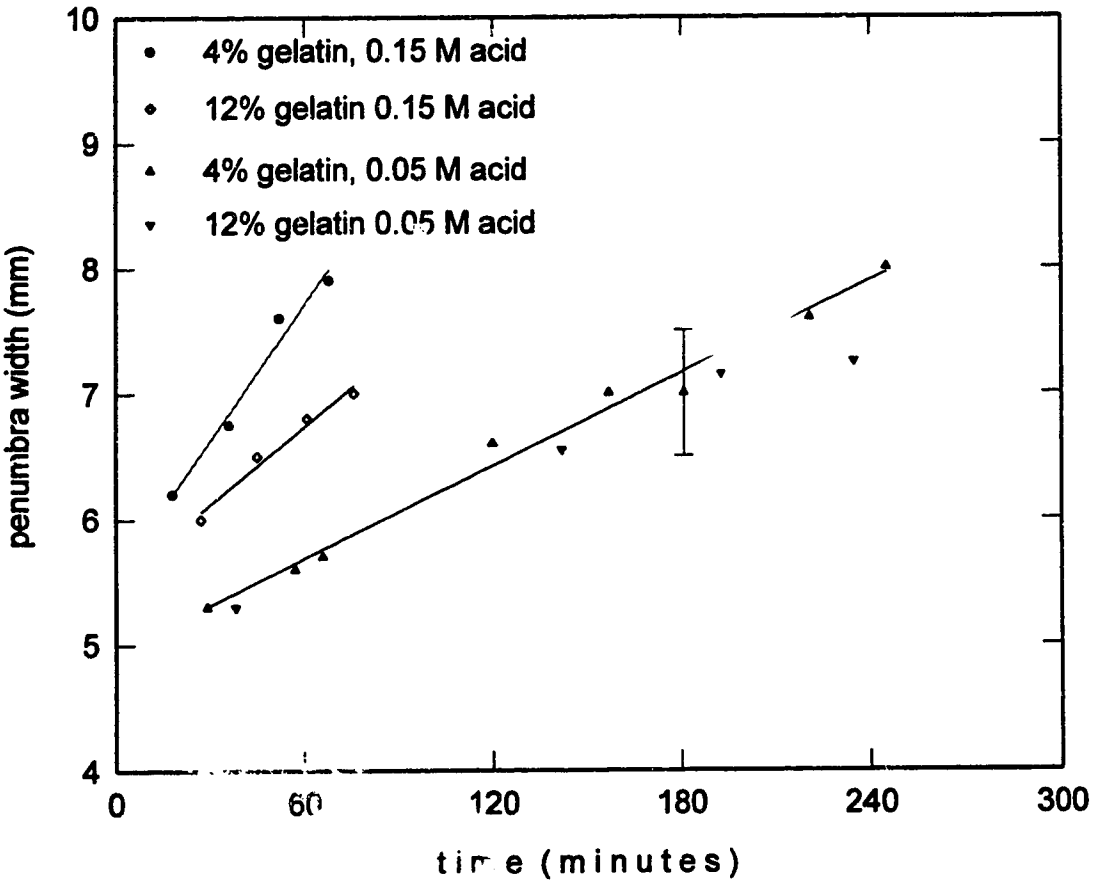

Figure 4.7 Width of the measured beam penumbra vs post-irradiation time in various dosimeter gels. The initial 0.49 cm beam penumbra was created using a half-blocked 6 MV photon beam. Penumbra width is the distance between 80% and 20% dose levels.

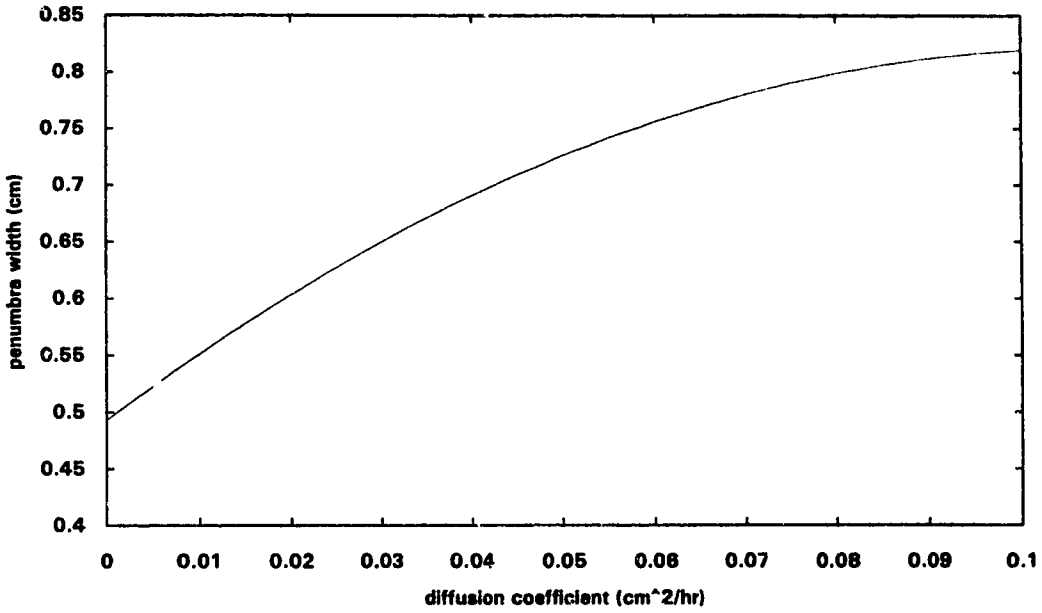

Figure 4.8 Calculated penumbra width 2 hours post-irradiation vs diffusion coefficient, obtained by convolution of an initial beam penumbra of width 0.49 cm with a time-dependent Gaussian spread function.

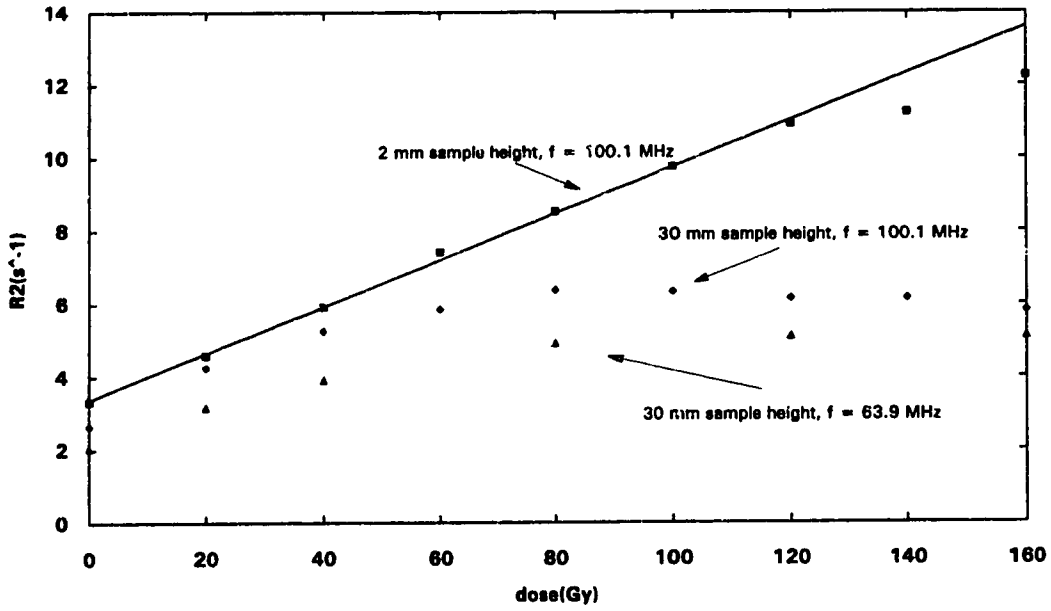

Figure 4.9 Sample size dependence of the dose response curve in 12% gelatin, 0.15 M H_2SO_4 Fricke gelatin. Dose was delivered using a 6 MV photon beam. Sample temperatures were 23° C at 63.9 MHz and 2° C at 100.1 Mhz. The 63.9 MHz data was acquired with a CPMG imaging sequence with TR = 2000 ms, TE = 50 ms and slice thickness of 5 mm.

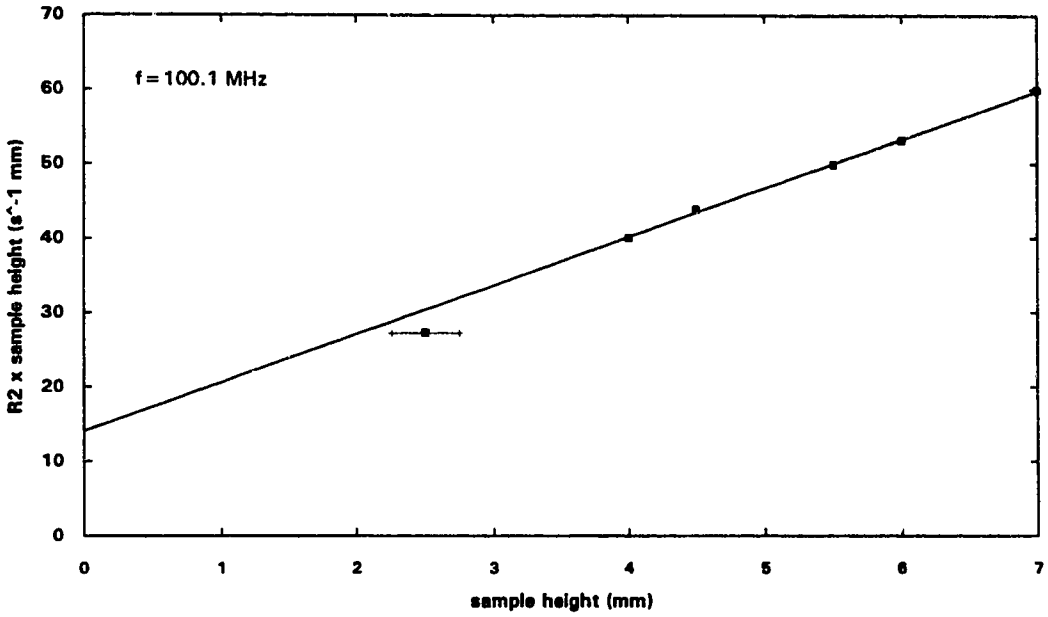

Figure 4.10 Variation in *R2* with sample height for a dose of 120 Gy. The material was 12% gelatin, 0.15 M H_2SO_4 and 1 mM $FeSO_4$.

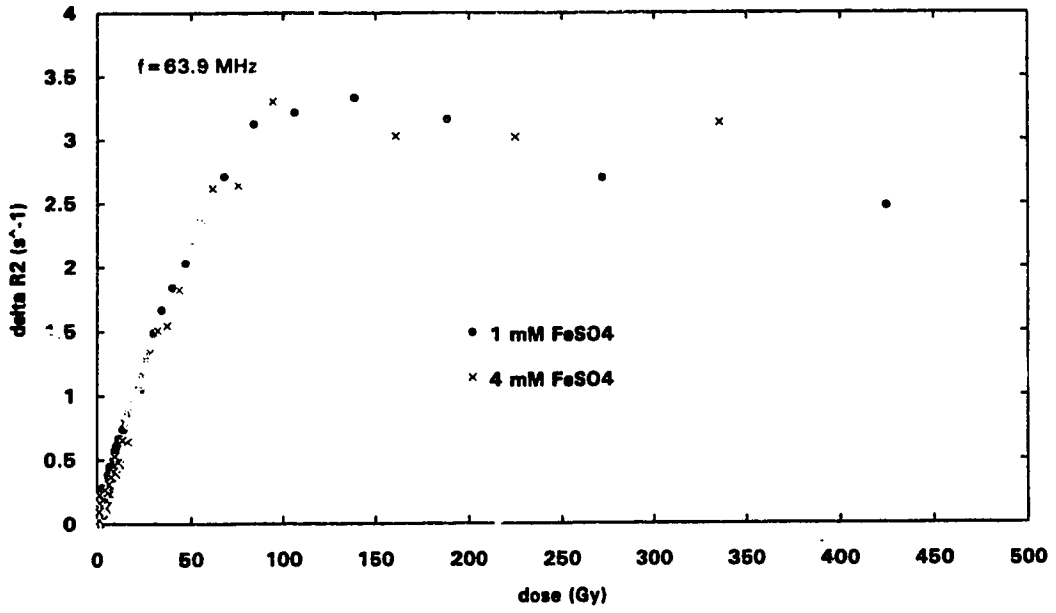

Figure 4.11 Comparison of dose response curves for an ^{192}Ir HDR source using two concentrations of ferrous ion. The material was 4% gelatin, 0.05 M H_2SO_4. Imaging at 63.9 Mhz was done using an 8 echo CPMG sequence with TR=2000 ms, TE = 50 ms and slice thickness of 5 mm.

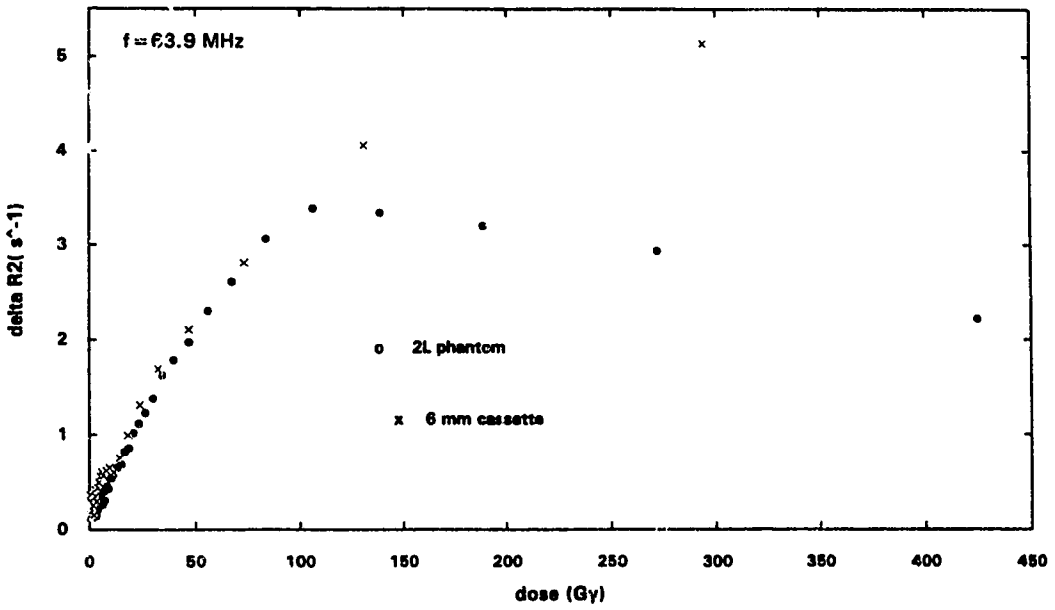

Figure 4.12 Comparison of dose response curves for an ^{192}Ir HDR source for two phantom configurations. Imaging at 63.9 MHz was done using an 8 echo CPMG sequence with TR = 2000 ms, TE = 50 ms and slice thickness of 5mm.

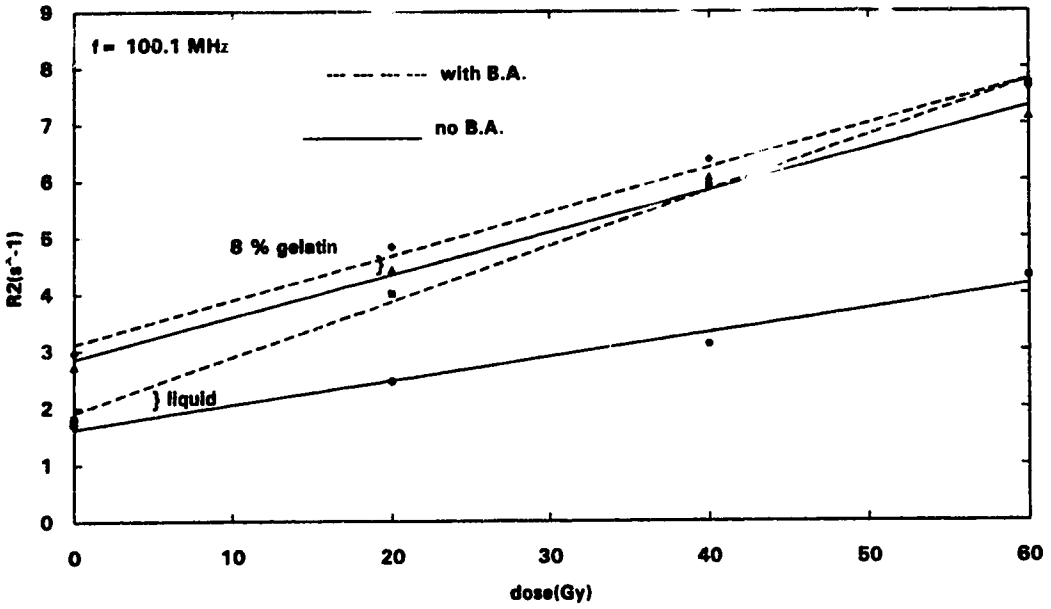

Figure 4.13 Comparison of the effects of adding benzoic acid (B.A.) to liquid Fricke and 8% gelatin, 0.05 H_2SO_4, 1 mM $FeSO_4$ Fricke dosimeter.

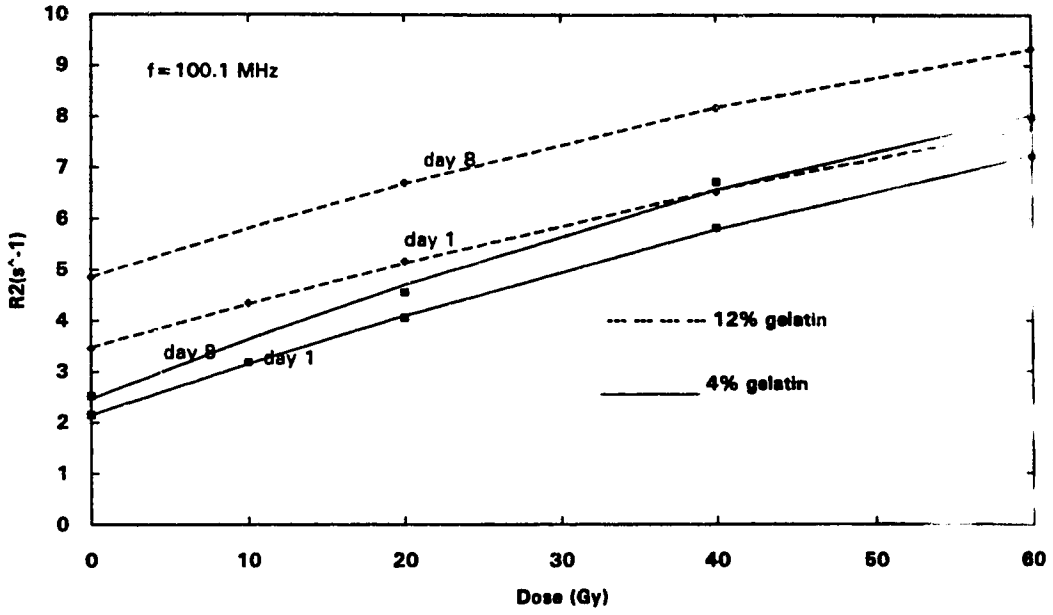

Figure 4.14 Change in dose response curves over time for 4% and 12% gelatin ferrous sulphate materials with 0.05 H_2SO_4 and 1mM $FeSO_4$.

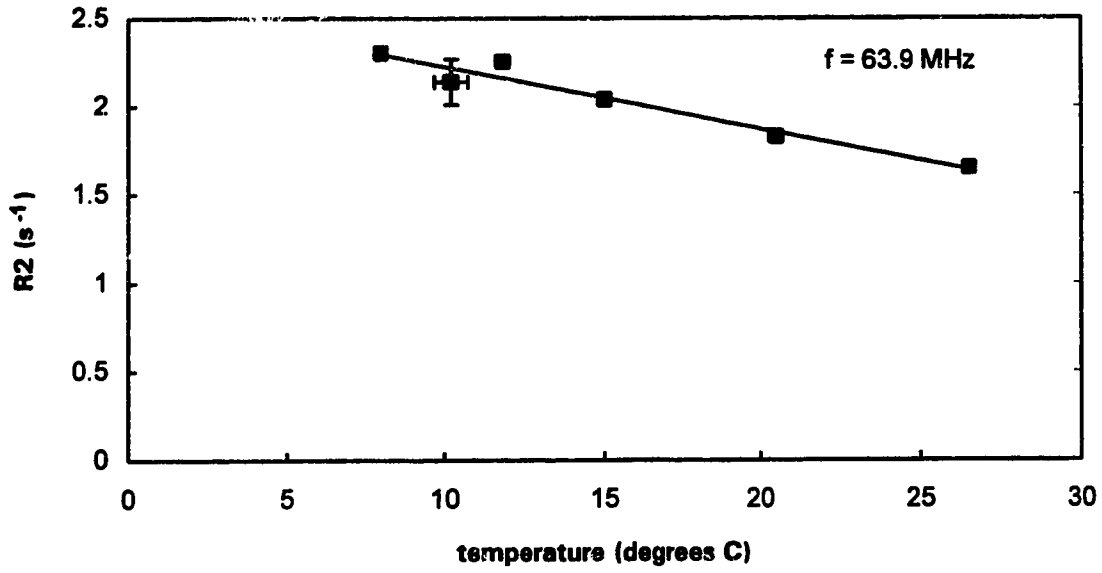

Figure 4.15 Variation in *R2* with temperature in unirradiated 4% gelatin, 0.05 MH_2SO_4, 1mM $FeSO_4$ dosimeter material. The line fitting the data is given by $R2(s^{-1}) = 2.58 - 0.035T$ where T is temperature in °C.

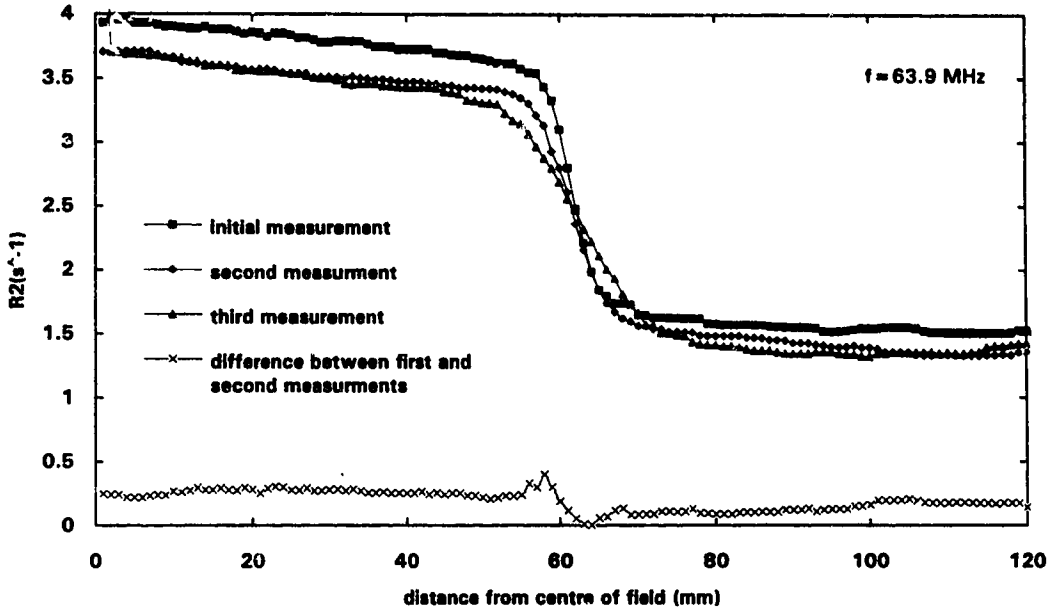

Figure 4.16 Temperature change effects on the *R2* profile across an irradiated phantom. Note that *R2*, not $\Delta R2$, was measured here. The phantom was prepared and irradiated at 20° C and initially imaged immediately after positioning in the bore of the magnet at ~23° C. The phantom was undisturbed in the bore and imaged a second time 2 hours later and a third time 12 hours later. A dose of ~ 40 Gy was delivered at the depth of measurement to the centre of the field.

Chapter 5

Corr g for imperfect tip angles in multi-echo pulse sequence MRI dosimetry[a]

5.1. Introduction

It has been demonstrated in Chapter 4 that *R2* is a more sensitive measure of dose than *R1* in the Fricke gel dosimeter. This is also true in polymer gel dosimeters [Maryanski *et al.* 1993, 1994]. Multi-echo sequences are considerably more efficient and accurate than single Hahn echo [Hahn 1950] sequences for the measurement of *R2*, which is an important consideration when the time scale for significant diffusion of ferric ions following irradiation is on the order of 1-2 hours. As described in Chapter 3, the accuracy of *R2* measurements in MRI is limited by the fact that non-uniformities in tip angle across a phantom lead to stimulated echoes when using multi-spin echo sequences [Majumdar *et al.* 1986, Crawley and Henkelman 1987, Fransson *et al.* 1993] such as the Carr-Purcell-Meiboom-Gill (CPMG) sequence [Carr and Purcell 1954, Meiboom and Gill 1958]. Repetition of imperfect refocussing pulses leads to rapid escalation of the number of unwanted echoes that refocus to form an image. For example, after the 8^{th} refocussing pulse there are 750 possible sources of unwanted echoes [Majumdar *et al.* 1986]. The result is that the spin-echo amplitudes which should otherwise decay exponentially, do not, and erroneous estimation of *T2* results. RF inhomogeneity is particularly severe for large phantoms, due to skin depth effects, when the phantom material has a high electrical conductivity, as is the case in the Fricke-gel dosimeter [Maryanski and Gore 1992].

5.2 Correction techniques

Several methods have been used for eliminating stimulated echoes arising from unwanted longitudinal magnetization [Majumdar *et al.* 1986, Crawley and Henkelman 1987, Maryanski and Gore 1992, Zur and Stokar 1987]. However, crusher-gradient schemes or phase alternation do not replace the signal lost from the primary echoes to the longitudinal direction, and the even-odd discrepancy is not corrected for. This is particularly important in MRI dosimetry where variations in *R2* on the order of

---

[a] Sections of this chapter closely follow a previously submitted paper [Duzenli and Robinson 1994].

5% are significant. The only method that completely avoids the stimulated echo problem employs a series of single Hahn echo sequences with a range of *TE* settings and a long *TR* [Maryanski and Gore 1992]. However, the drawbacks to using Hahn echoes have been outlined in Chapter 3. Also, on some commercial scanners[a] there is a limited range of *TE* settings beyond which single echoes are not available in clinical imaging mode. Since the relaxation times for the Fricke-gelatin dosimeter are typically between 400 and 800 ms, echoes out to at least 400 ms are required.

The commercial MRI system used in this study[a] does not eliminate reverse parity stimulated echoes when a single signal average is acquired. However for even numbers of signal averages, these echoes are effectively canceled as a result of phase alternation. This can easily be verified by enlarging the field of view (FOV) and shifting it off center in the phase encode direction by half the width of the phantom. The DC offset is also effectively removed using phase alternation. In the following discussion, it is assumed that reverse parity stimulated echoes and baseline have been removed. If it is not possible to implement a method to eliminate such echoes, the FOV can be enlarged and shifted such that the phase reversed echoes do not superimpose on the main image. However, this may reduce spatial resolution and possibly amplify spatial distortion and will not remove all unwanted echoes. Also, if a baseline offset is present the two-parameter fitting technique described below will not work.

Equation 3.2 describes the signal intensity for echo number n of a multi-echo sequence. In the case of non-uniform tip angles across the phantom, an echo modification factor $f(n,x,y,z)$ must be included, so that Equation 3.2 can be rewritten as

$$S(n) = f(n,x,y,z) \cdot k \cdot \rho \cdot P_1(T1,N,TE,TR)e^{-P_2 nTE}, \qquad 5.1$$

where P_1 includes the $T1$ dependent terms from Equation 3.2 and $P_2 = R2$. Due to the factor f, the echo amplitudes no longer decay exponentially with time constant $T2$. Strictly speaking the factor f may also have $T1$ and $T2$ dependence [Hughes 1977] but this is assumed to be small if the dominant stimulated echoes are removed. In Figure 5.1 the variation in echo amplitude as a function of echo number for an 8-echo CPMG imaging sequence is shown for two regions within the same phantom. Echo amplitudes are presented for two consecutive imaging sequences in Region 1 near the center of the phantom, and in Region 2 at the lower right corner of the phantom shown in Figure 5.4. In Region 1 very little distortion in image intensity was evident, whereas in Region 2

[a]Philips Gyroscan ACS Version 1.6

marked loss in signal intensity compared with the rest of the phantom was apparent. The discrepancy between even and odd echoes and the deviation from exponential behaviour in the data are evident. However, the reproducibility in echo amplitude and therefore f between the two scans for each region is good. Although both regions contained identical phantom material, the data in Region 2 clearly drop off much more rapidly than in Region 1. The resulting *R2* value from an exponential fit to the echo amplitudes in Region 2 would therefore be substantially higher than that for Region 1.

It has been proposed [Gambarini *et al.* 1994] that a position-dependent correction factor could be applied to *R2* values calculated by exponentially fitting echo amplitudes such as those shown in Figure 5.1. The use of such a correction factor is not supported by the discussion above. It might also be envisioned that subtraction of a pre-irradiation *R2* image from a post-irradiation *R2* image would remove the distortion. This will only be the case under the circumstance that the factor f accumulates by the same fraction for every echo, when it can be written as

$$f(n,x,y,z) = a(x,y,z)^n = e^{\ln[a(x,y,z)]n}. \qquad 5.2$$

In this form the factor f can be absorbed into the exponent in Equation 5.1. If identical spin-echo sequences are performed pre- and post-irradiation (with echo amplitudes *S(n)* and *S'(n)* respectively), two-parameter fits of the form

$$S(n) = A_1 e^{-A_2 n} \quad \text{and} \quad S'(n) = A_1' e^{-A_2' n} \qquad 5.3$$

can be done. Parameters A_1 and A_1' represent $k\rho P_1$ and $k\rho P_1'$, while A_2 and A_2' represent $ln[a] - P_2 \cdot TE$ and $ln[a] - P_2' \cdot TE$. The echo modification factor can then be eliminated and the change in *R2* arrived at by subtracting A_2' from A_2. However, the form of f described in Equation 5.2 is not valid in general [Hughes 1977] and, in particular, does not account for the even-odd echo discrepency. If only the even numbered echoes are used, the fit will be substantially better than if all echoes are used. This method is also subject to noise magnification arising from image subtraction.

The proposed echo correction method, introduced in this thesis, involves factoring out the non-uniformity in f by dividing each of the pre-irradiation echoes by its post-irradiation counterpart echo. For a given echo number n at position (x,y,z) in the phantom, the quotient of the pre- to post-irradiation echoes is given by

$$\frac{S(n)}{S'(n)} = \frac{P_1}{P_1'} e^{[-nTE\{R2-R2'\}]}. \qquad 5.4$$

A two-parameter exponential fit to the echo quotients of the form

$$\frac{S(n)}{S'(n)} = A_1 exp(-A_2 \cdot nTE) \qquad 5.5$$

can now be done to recover $R2 - R2' = A_2/TE$ and a $T1$-dependent factor $A_1 = P_1/P_1'$. This method requires no assumptions as to the behavior of $f(n,x,y,z)$, other than that it be reproducible for two separate sequences and independent of $T1$ and $T2$. Also, the value of A_1 can be estimated from TR, TE, N and the expected values of $T1$ and $T1'$, serving as a useful check on the accuracy of the fitting algorithm. Since image subtraction is not required, a high contrast-to-noise ratio in the final calculated image is maintained, and the uncertainty arising from fitting all echo quotients is reduced because the odd-even discrepancy is largely eliminated.

5.3 Results and discussion

Images were acquired on a 1.5 Tesla clinical MRI system[a]. Two signal averages of a 2DFT phase-alternated spin echo sequence with $n = 8$, $TE = 50$ ms, and $TR = 2000$ ms were acquired. The FOV was 256 mm, and the acquisition matrix size of 256 x 256 gave a pixel size of 1 x 1 mm with slice thickness of either 5 or 10 mm. Hereafter, this will be termed the *standard imaging sequence*. The phase encode direction was left to right. The experimental setup is indicated in Figure 5.2.

Figure 5.3 depicts the echo amplitudes and their pre- to post-irradiation ratios from Region 3 situated in the center of the 100% contour on Figure 5.4. A dose of ~ 30 Gy was delivered to this region. The first four echo quotients are well behaved, whereas some deviation from the straight line fit to the logrithms of the echo quotients is evident in the last four points. This could be indicative of a slight $T1$ or $T2$ dependence in the factor f resulting from incomplete removal of all stimulated components. Analyzing the data in several ways to determine the pre- to post-irradiation change in $R2$ reveals the superiority of the echo quotient technique. Results of linear least squares regression analyses on the natural logarithms of the echo amplitude data are tabulated in Table 5.1. For the echo quotient technique the values in columns 4 and 5 refer to $\Delta R2$. Although all

[a] Philips Gyroscan ACS Version 1.6

processing methods result in $\Delta R2$ values consistent with one another within statistical error, the echo quotient technique produces the result with the lowest uncertainty.

In Figures 5.4 and 5.5, iso-$R2$ curves for an irradiated phantom are compared with $\Delta R2$ curves determined using the echo quotient technique. MRI data were acquired using a 2 litre phantom containing standard Fricke-gelatin dosimeter gel. A two-parameter exponential fit to the echo quotients was done using an adaptation of the Marquart-Levenberg non-linear least squares regression algorithm [Press *et al.* 1988].

Table 5.1 Comparison of echo amplitude processing methods

data points used in fit	regression R	$R2$ (s^{-1})	standard error in $R2$ (s^{-1})	$\Delta R2$ (s^{-1})
pre-irradiation scan (all echoes)	0.988	1.82	0.116	
post-irradiation scan (all echoes)	0.995	3.57	0.146	1.75 ± 0.26
pre-irradiation scan (even echoes)	0.999	1.800	0.0331	
post-irradiation scan (even echoes)	0.999	3.500	0.0460	1.70 ± 0.08
echo quotients (all echoes)	0.998	1.746	0.0410	1.75 ± 0.04

In Figure 5.4, a maximum dose of 30 Gy was delivered to a depth of 2.8 cm along the central axis of a 12 MeV electron beam produced by a linear accelerator[a]. All $R2$ and $\Delta R2$ values were normalized to 100% at the depth of maximum dose. At the left, $R2$ curves calculated by an exponential fit to all echo amplitudes of the post-

[a] Varian Clinac 2300 CD, Varian Associates Inc., Palo Alto Ca., USA.

irradiation scan are shown. In this case severe distortion in the calculated values of up to 50% of the maximum *R2* value is present. At the right, $\Delta R2$ curves are shown for the same data, processed by the echo quotient technique with an identical echo sequence acquired prior to irradiation. Two observations can be made based on a comparison of the two results. First, the maximum distortion in $\Delta R2$ using the echo quotient technique is reduced to 10% of the maximum $\Delta R2$ value, near the edges of the phantom. This residual distortion occurs parallel to the phantom edges in the phase encode direction but is not apparent at the lower phantom edge. Secondly, the $\Delta R2$ lines are smoother than the *R2* lines, due to removal of the even-odd discrepancy in echo amplitudes. The standard deviation of $\Delta R2$ values within the 4% contour is 0.02 s^{-1}, compared to the maximum $\Delta R2$ of 1.73 s^{-1}. This would imply that the minimum detectable $\Delta R2$ is 0.06 s^{-1}, corresponding to a dose of approximately 1 Gy. Quantitative comparison of the isodose lines for this data follows in Chapter 6.

In Figure 5.5, a dose of 20 Gy was delivered to a depth of 1.5 cm on the central beam axis using a 6 MV, 45° dynamically wedged beam produced by the same linear accelerator[a]. The same phantom in the same position within the RF head coil as in Figure 5.4 was used. In Figure 5.5 all data were smoothed using a 5x5 point median filter to retain edge sharpness. The spatial reproducibility in *R2* distortion from Figure 5.4 to Figure 5.5 is apparent, although the relative severity of the distortion is greater in Figure 5.5, as a lower normalization dose was delivered and the region of interest for dose measurement now extends throughout the phantom volume. Also shown in Figure 5.5 is the $\Delta R2$ distribution calculated by subtracting *R2* values obtained by fitting the pre- and post-irradiation echoes separately. Quantitative evaluation of the dose distribution to follow in Chapter 6 indicates that the echo quotient technique provides the more accurate estimation of absorbed dose.

The total imaging time for the standard sequence used above was 17.1 minutes. Although this is doubled by the requirement for a pre-irradiation scan, only the post-irradiation imaging time is relevant to accurate dosimetry. For comparison, the time required to obtain the equivalent data using single Hahn echo sequences would be 8 x 256 x *TR*. *TR* would be chosen to be ~ 5 times the longest expected *T1* or approximately 3800 ms, giving rise to a total imaging time of ~ 130 min. Using image intensity as opposed to *R2* would require approximately the same total imaging time as the echo quotient technique, since the dose response curve is preferably obtained from a

---

[a] Varian Clinac 2300 CD, Varian Associates Inc., Palo Alto Ca., USA.

calibration scan done on a separate phantom during the same imaging session [Schreiner *et al.* 1994]. The potential advantage of using $\Delta R2$ over image intensity for dosimetry is that universal dose calibration curves for $\Delta R2$ can be obtained independently of the particular phantom setup being studied, whereas image intensity values have been shown to be highly dependent on the setup.

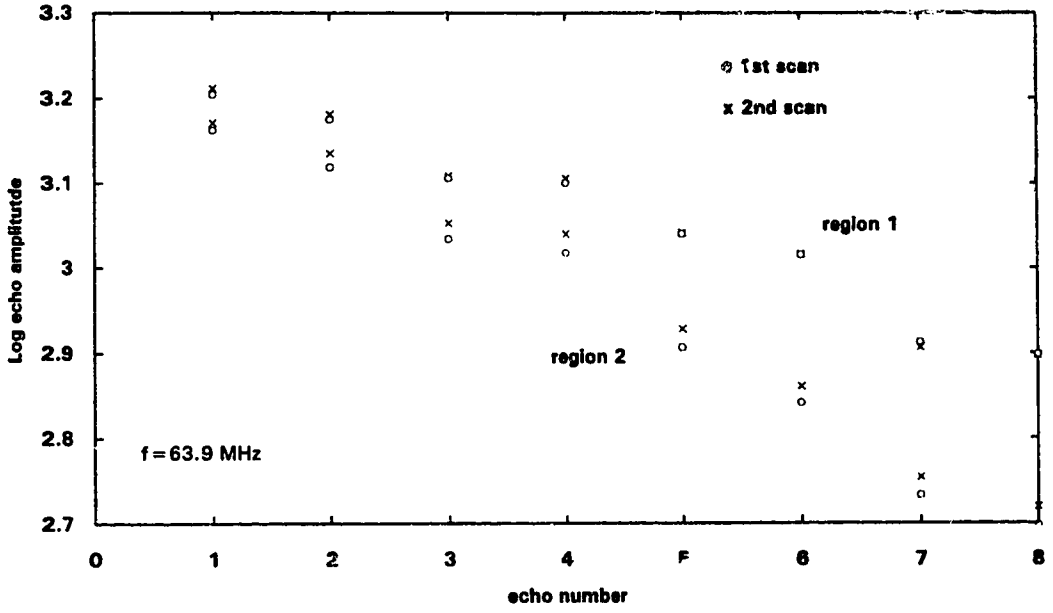

Figure 5.1 Echo amplitudes for two consecutive scans in two regions of a homogeneous unirradiated phantom. In Region 1 no significant intensity distortion due to tip angle problems was present whereas in Region 2 significant distortion was evident. The locations of these regions are indicated on Figure 5.4, where the same phantom was used.

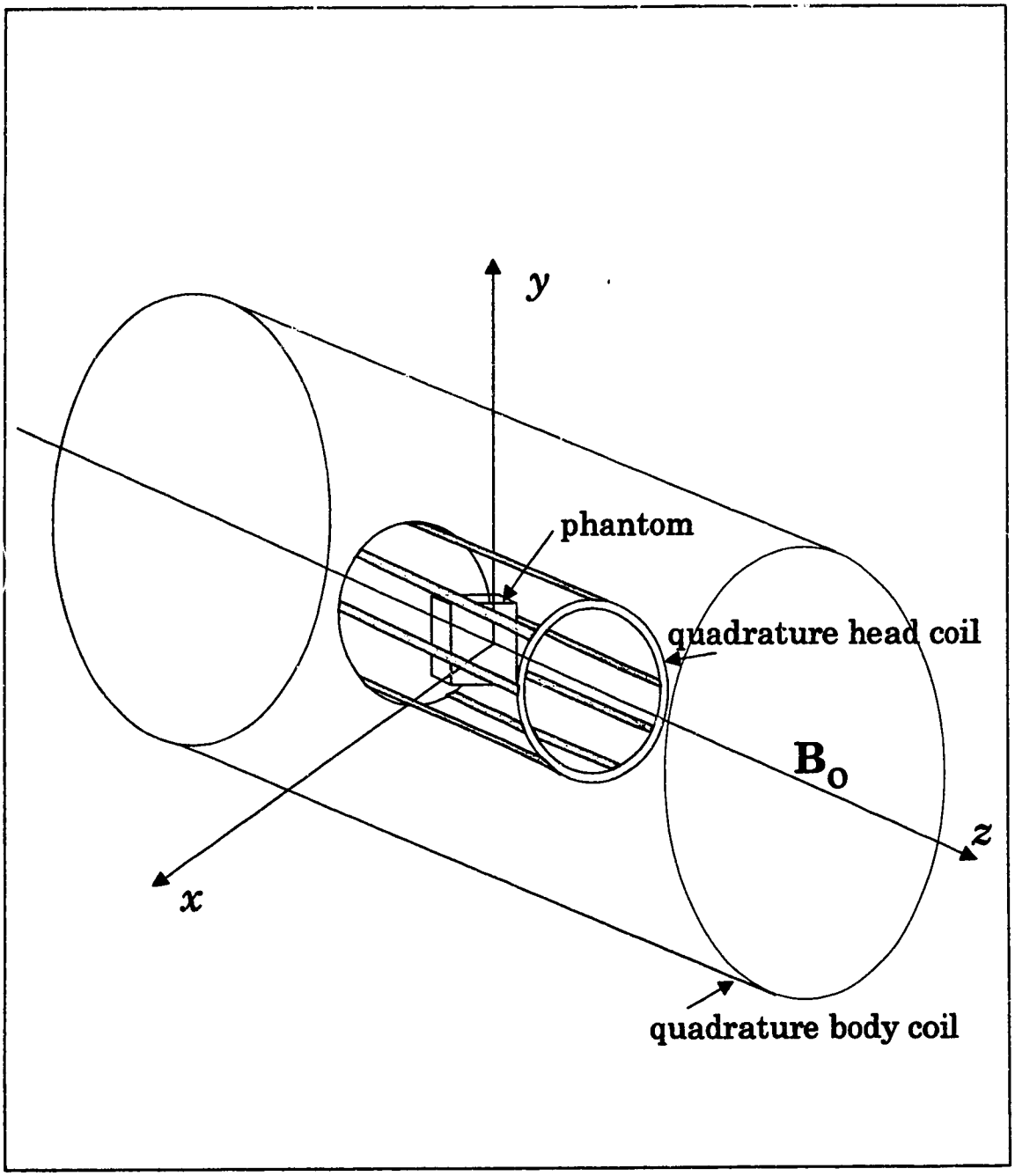

Figure 5.2 Schematic representation of imaging setup. The *z*-direction is defined by the main Bo field. The imaging planes are defined by the coordinate axes as follows:

x-y plane = transverse
y-z plane = sagittal
x-z plane = coronal

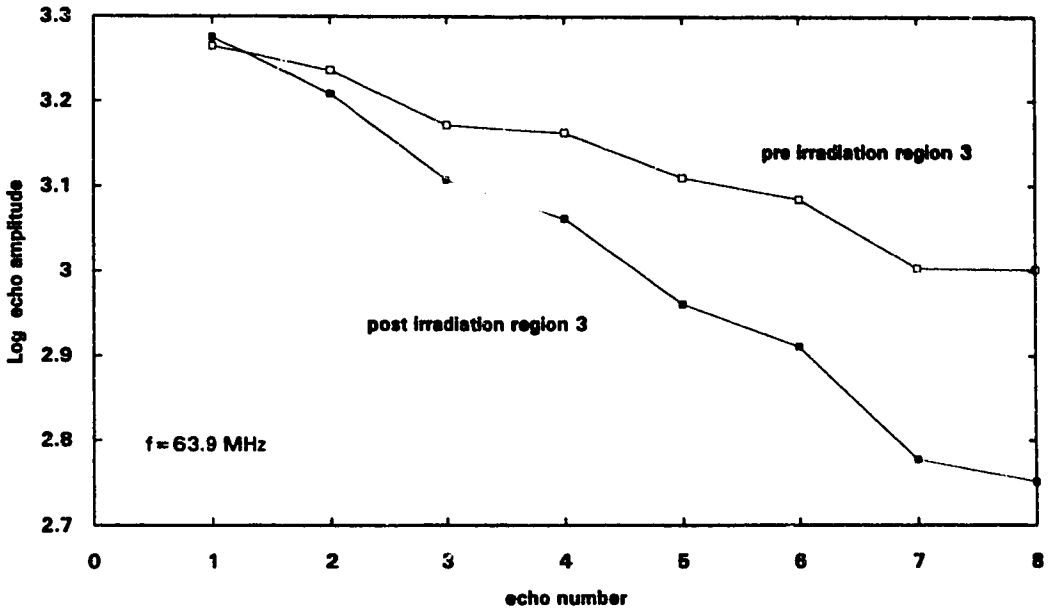

Figure 5.3a Echo amplitudes for pre- and post-irradiation scans in Region 3 (see Figure 5.4) irradiated to a dose of ~ 30 Gy. Lines have been drawn connecting data points to emphasize the even-odd discrepancy.

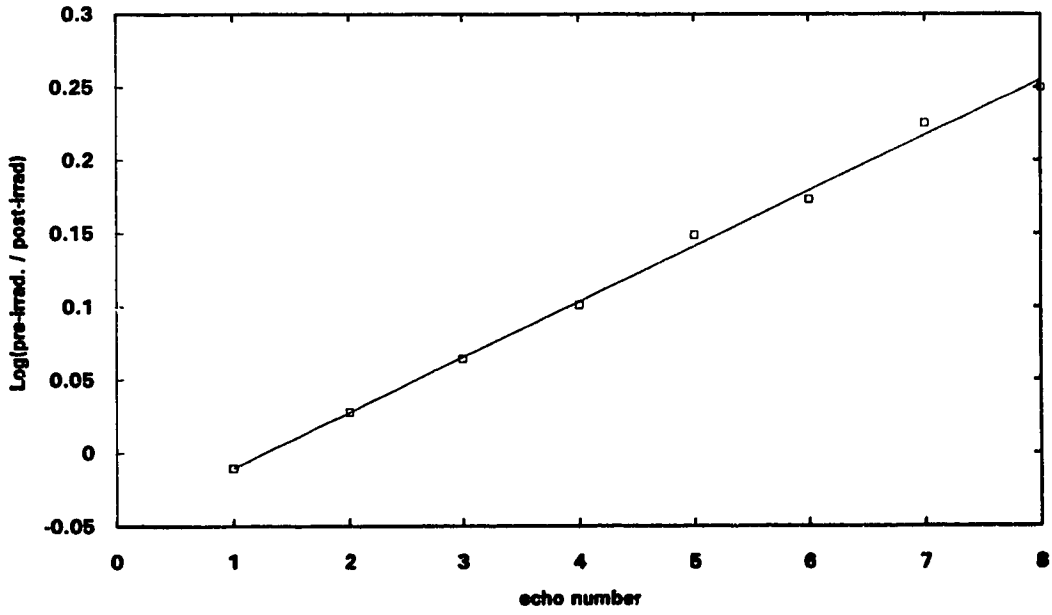

Figure 5.3b Ratio of pre-irradiation to post-irradiation echo amplitudes for data shown in Figure 5.3a.

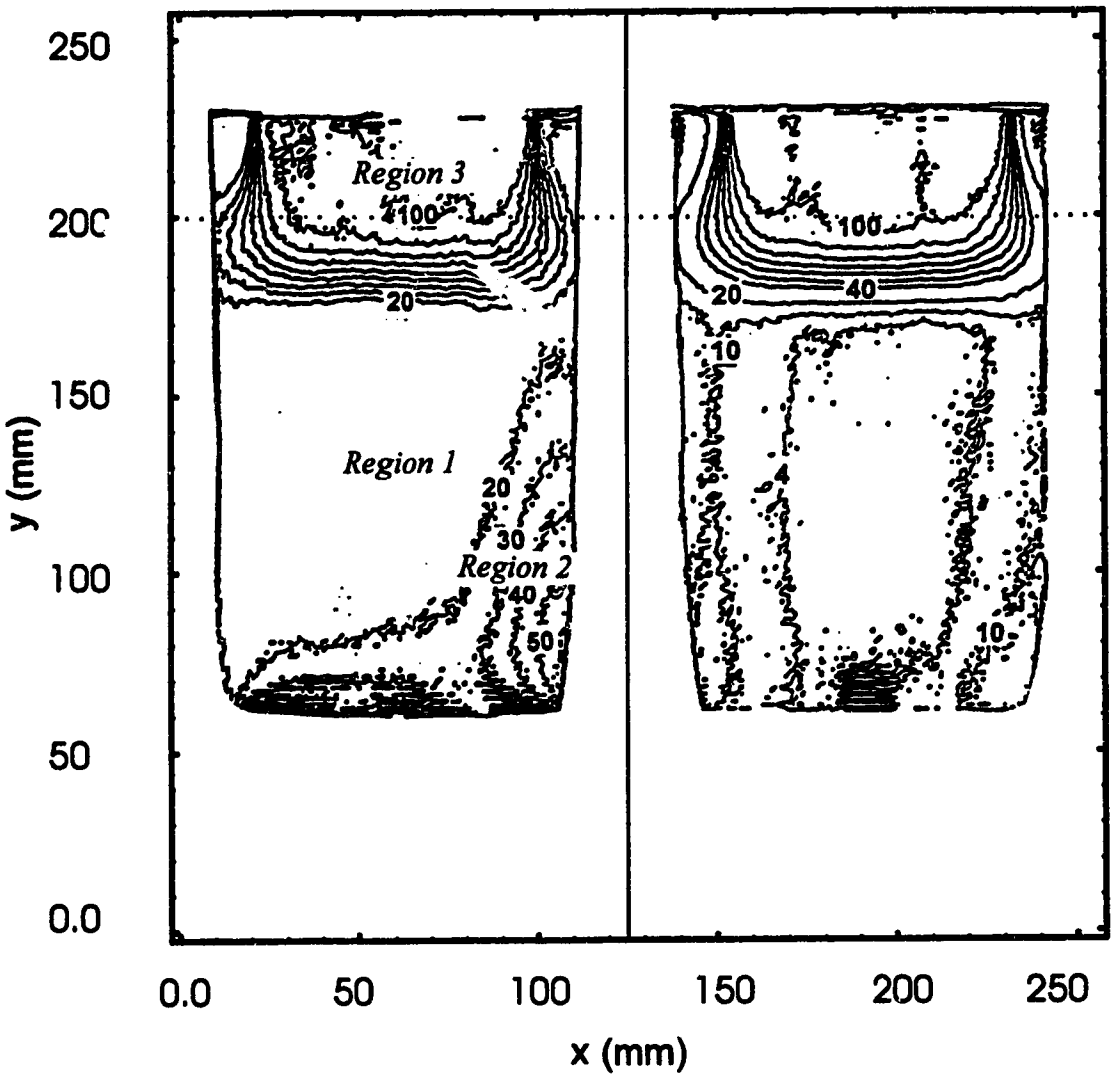

Figure 5.4 Iso-R2 and change in R2 contours in a Fricke gel phantom irradiated with a 12 MeV electron beam and imaged in the transverse plane. The phase encode direction was left-right. On the left the R2 contours were calculated using a two-parameter exponential fit to the 8 echo amplitudes. On the right are change in R2 contours calculated using the echo quotient technique applied to pre- and post-irradiation echo amplitudes. Contour values are normalized to 100 at a depth of 2.8 cm, indicated by the dotted line, on central axis.

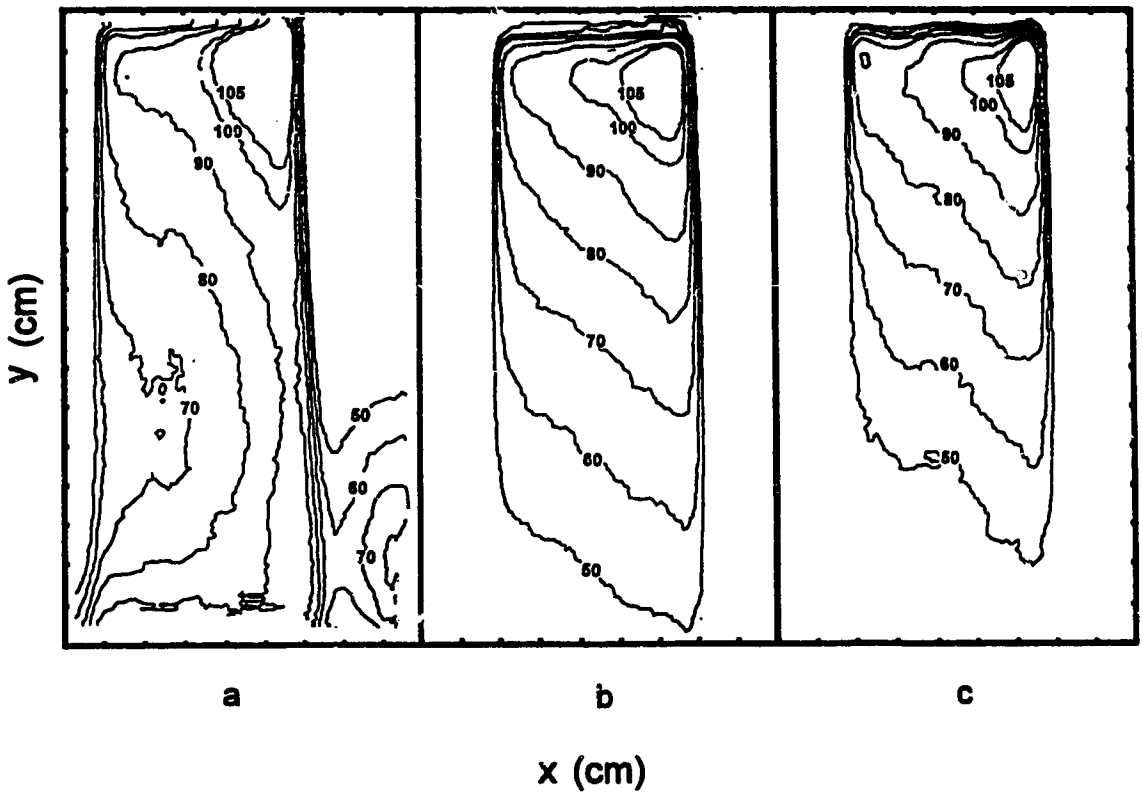

Figure 5.5 A second example of distortion in a calculated R2 distribution for a post-irradiation scan (a) and the corrected change in R2 distribution using the echo quotient technique (b). Also shown in (c) is the change in R2 distribution obtained by subtracting the R2 values calculated by fitting the pre-and post-irradiation echoes separately. A 5x5 median filter was applied to all data to reduce the noise. The same phantom and imaging parameters as in Figure 5.4 were used.

Chapter 6

Applications

6.1 Electron beam

Electron beam dosimetry is a situation where conventional small volume dosimeters such as diodes work well for determining relative dose distributions. Diode measurements in a water phantom can serve as a standard against which the accuracy of the MRI technique can be evaluated. A measured isodose distribution for a 12 MeV electron beam using the MRI echo quotient technique with slice thickness 1.0 cm is shown at the left in Figure 6.1. The electron beam was produced using a linear accelerator[a] with a beam-defining aperture (cutout made of lead alloy) of 8 x 8 cm^2 positioned 5.0 cm from the surface of the phantom. A dose of 30 Gy was delivered to a depth of 2.8 cm on the central axis, at a dose rate of 3 Gy min^{-1}. The plastic-walled two litre phantom contained the standard Fricke gelatin material and the beam entrance surface was open to the air during irradiation. The dimensions of the phantom were 11 cm x 13 cm x 18 cm in height. Prior to and following irradiation, the phantom was capped in order to prevent dehydration near the gel surface. The phantom was placed in a 30 x 30 cm^2 x 20 cm deep water tank to provide full scattering conditions during irradiation. A quadrature head coil and the *standard imaging sequence* (refer to Section 5.3) with a slice thickness of 1 cm and pixel size 1 mm x 1 mm were used. No data smoothing was done after the two-parameter exponential fit to the echo quotients.

On the right in Figure 6.1 is the corresponding dose distribution measured using a silicon diode with a sensitive volume ~0.3 cm^3 designed for electron beam dosimetry. The two dose distributions agree along the central axis to within 1 mm except in the buildup region near the phantom surface. The MRI measurement is incorrect in this region since the 90% isodose curve should close on itself as indicated by the diode measurement. Also, near the lateral edges of the dose window (which correspond to the edges of the phantom), the MRI data tend to balloon out to a greater extent than the diode data. For example at its widest point, the half width of the 50% isodose line is 4.6 cm for the MRI data and 4.2 cm for the

[a] Clinac 2300 CD, Varian Associates Inc., Palo Alto CA

diode data. This 4 mm difference corresponds approximately to a 10% difference in dose, according to the distance between adjacent isodose curves in this region. This discrepancy may result from the residual 10% distortion in $\Delta R2$ near the phantom edges shown in Figure 5.4. Although the dosimeter gel might be better aerated near the phantom edges due to oxygen penetration through the plastic walls, it is unlikely that this would account for a 10% discrepancy in $\Delta R2$ at a dose of 15 Gy. Changes in magnetic susceptibility at the phantom-air interface might be responsible for this effect, and could be avoided by using a larger phantom, allowing at least a 2 cm margin around the expected dose distribution. Alternatively, there could be some banding artifacts present [Zur and Stokar 1987], resulting from the interference of some remaining stimulated echoes, causing the observed discrepancy.

The variation in relative dose along the central beam axis for the MRI and diode measurements is shown in Figure 6.2. Doses are normalized to 100% at a depth of 2.8 cm (d_{max}). The expected surface dose for 12 MeV electrons is 87% of the dose delivered to d_{max} in this case, whereas the measured MRI value near the phantom surface is greater. This can be partially explained by the presence of higher levels of oxygen near the surface of the gel compared with deeper positions, as discussed in Chapter 4, however the magnitude and depth of the discrepancy are larger than expected based on the oxygen effect alone. Since the oxygen level will decrease with depth along the beam axis, the dosimeter sensitivity will also decrease, and correction for the varying degree of over response will be difficult. If the maximum dose is kept to 20 Gy, the difference between the linear dose response curve for well-oxygenated gel and the non-linear dose response for gel at depth can be kept to a maximum of 5%. It is interesting to note that similar results for electron beam dose distributions near the phantom surface have been described by other groups [Hiraoka *et al.* 1993, Olsson *et al.* 1990].

One possible means of overcoming the problems associated with variations in oxygen concentration would be to use a gel cassette phantom geometry. A thin layer (5 mm) of gel poured into a plastic cassette could be used to measure dose in a slice sandwiched between slabs of an anthropomorphic phantom, much the way film and TLD are used. A uniform gel layer carefully prepared could have a more uniform oxygen concentration and homogeneous dose response. Several other advantages could also result from the use of a gel cassette. Slice-selective RF pulses would not be required since the slice would automatically be defined by the cassette itself, potentially leading to better tip angle uniformity at slice edges. This could however, be offset by the abrupt change in magnetic susceptibility at the edges of the

cassette. Also, the small sample volume of a gel cassette would contribute less electronic noise to the images (as discussed in Chapter 3) while the signal magnitude from the slice would remain the same, contributing to increased signal-to-noise ratio in the images. The author's initial experiences with such a gel cassette have been hindered by the difficulty of preparing a uniform thin layer of gel, free of air bubbles. In addition, the plastic base plate supporting the gel layer has the tendency to warp after several uses. Substantial effort would be required to design a cassette free of these problems.

6.2 Dynamically wedged photon beam

The dynamic wedge technique involves creating angled isodose curves for photon beams by stepping one collimating jaw across the treatment field during irradiation. Both the dwell time of the jaw and the dose rate are modulated in time. Currently dose distributions for the dynamic wedge must be obtained either by film (calibrated against ion chamber) or by arrays of ion chambers or diodes. The advantages of MRI dosimetry in this case have been outlined in Chapter 1.

In this study, a 5 x 5 cm^2, 45° dynamically-wedged 6 MV photon beam was used to deliver a dose of 20 Gy to a point on the central beam axis at a depth of 1.5 cm. Again, a linear accelerator[a] was used to produce the photon beam. 20 Gy was chosen in order to reduce the effects of variations in oxygen concentration (see Figure 4.9). The phantom used was a two litre plastic rectangular box, with the beam entrance surface exposed to air. Its dimensions were again 11 cm x 13 cm in cross section and 18 cm in height. The phantom was imaged in the transverse imaging plane (as defined in Figure 5.3) using the standard imaging sequence with slice thickness 1.0 cm.

Measured isodose curves for this application are shown in Figure 6.3. The isodose curves at the left are film data that have been corrected for non-linear dose response and normalized to ion chamber data along the central beam axis. The data at the right were obtained using the echo quotient MRI technique and an independently measured 6 MV dose response curve. The two sets of isodose curves agree to within ± 2 mm.

---

[a] Varian Clinac 2300 CD, Varian Associates Inc., Palo Alto CA

In Figure 6.4 percent depth dose along the central beam axis and beam profiles at a depth of 10.0 cm determined using MRI and either film or ion chamber are shown. In addition to the echo quotient MRI data, the data resulting from subtraction of *R2* values calculated from the pre and post-irradiation scans (as discussed in Chapter 5) are shown. The agreement between MRI echo quotient data and ion chamber data along the central axis is within 2.5%, indicating that any residual distortion near the phantom edge was minimal. The *R2* subtraction data is in error by up to ~10%. In the dose buildup region near the phantom surface, very good agreement is shown between the MRI and ion chamber data, indicating that oxygen depletion effects were minimal. The absolute dose measured using the echo quotient technique at the normalization point is accurate to within 2% of the prescribed dose. The wedge angle from the echo quotient MRI data was determined to be 40° ± 2°, compared with 42° ± 1° from the film data. Although these both differ from the nominal 45° angle specified by the accelerator software, the good agreement between the two reinforces the potential of the MRI technique.

6.3 High Dose Rate Brachytherapy

The potential advantages of measuring brachytherapy dose distributions using MRI gel dosimetry have been outlined in Chapter 1. These include the water equivalent response of the dosimeter over a wide range of photon energies, and high spatial resolution. In high dose rate (HDR) brachytherapy , doses in the optimal range for Fricke gel dosimetry can be delivered in a matter of minutes. Due to the problem of significant ion diffusion over the course of several hours, low dose rate (LDR) brachytherapy, where periods of ~ 20 hours are required to deliver doses in the sensitivity range of Fricke gels, is not a suitable candidate for Fricke gel dosimetry.

An isodose distribution surrounding a Nucletron microSelectron[a] ^{192}Ir source, measured using the echo quotient technique, is shown at the left in Figure 6.5. The slice thickness was 5 mm and the pixel size in the plane of the distribution was 1 mm x 1 mm. The slice thickness therefore exceeded the catheter diameter by approximately 3.5 mm. The source entered the phantom from the lower edge of the figure. Shown in the upper right quadrant is the dose distribution around the source

[a] Nucletron Corp., Columbia MD

calculated using the planning system currently in use[a] at the Cross Cancer Institute for clinical brachytherapy treatment planning. Isodose levels for the MRI measurement were obtained from the treatment planning system, based on a dose of 17 Gy delivered to a reference point 2 cm from the source along its perpendicular bisector, indicated by the line AB on Figure 6.5. The measured and calculated isodose curves are therefore matched in position along the line AB, at a distance of 2 cm from the centre of the source. However, very good agreement is also seen between the measured and calculated isodose curves along the line CD. Less than 1 mm discrepancy is observable between the two sets of isodose curves. It should be noted that partial volume effects have been neglected in all the HDR measurements presented in this thesis. However, the effects of voxel size on MRI measurements in HDR dosimetry could form the basis for further study.

A defining characteristic of each brachytherapy source is the anisotropy in the dose distribution due to attenuation of photons in the capsule enclosing the radionuclide. Pinching in of the isodose curves at the ends of the source, as seen in Figure 6.5, is due to a longer path length traveled by emerging photons in traversing the ends of the capsule compared with the sides. The source used here has approximate active dimensions of 0.6 mm in diameter and 3.5 mm in length. Including the stainless steel encapsulation, external dimensions are approximately 1.1 mm in diameter and 4.5 mm in length, not including the weld at the end of the capsule securing the source to the drive cable. The plastic intralumenal catheter within which the source assembly moves has an inner diameter of approximately 1.5 mm, allowing for a maximum deviation of ~ 2° between the source and catheter axes.

The anisotropy factor is defined as the ratio of the dose at a given radius and angle θ from the source axis to the dose at the same radius for $\theta = 90°$, the angle at which maximum dose is achieved. In air, the anisotropy is essentially independent of radius, whereas in water, the anisotropy decreases with distance from the source due to photon scattering within the medium. The treatment planning algorithm used to produce the isodose curves in Figure 6.5 requires as input an estimate of the source anisotropy. It is recommended that the anisotropy be measured for every new source acquired, and compared with that used in the treatment planning system. The measured anisotropy in dose at a radius of 2.0 cm for the isodose curves shown in Figure 6.5 is presented in Figure 6.6. Interpolation within the 1 mm x 1 mm

[a] Nucleton Planning System Version 10.3, Nucletron Corp., Columbia MD.

pixel grid was accomplished using Mathematica[a] software Also shown are the anisotropy measurements of two other groups, [Muller-Runkel and Cho 1994] who employed 1 mm diameter by 6 mm length rod-shaped TLD's in polystyrene, and [Baltas *et al.* 1993] who used a 0.1 cc ion chamber in water. The data of Baltas *et al.* are currently used in the Nucletron treatment planning software. The standard deviation in the ion chamber measurements was 0.6%, whereas the uncertainty in the TLD measurements was ± 3%. In both of these cases, the values given are the results of averaging three different measurements. The MRI data show very good agreement with the other techniques despite the fact that only a single measurement was done. The standard deviation in $\Delta R2$ at a distance 6.0 cm from the source (where the dose distribution is essentially flat) is $\pm 0.02\ s^{-1}$, corresponding to a minimum detectable dose of ~ 1 Gy or ~ 5% of the dose at the 2 cm radius where the anisotropy was measured.

Ideally, an independently-measured dose response curve should be used to calculate absolute dose for the brachytherapy distribution. The $\Delta R2$ dose response curve (based on doses calculated using the planning system) for the ^{192}Ir source is compared with dose response curves for ^{60}Co photons (mean energy 1.25 MeV) and a 6 MV photon beam in Figure 6.7. The maximum discrepancy in $\Delta R2$ for points equidistant from the source to the left and right is $0.15\ s^{-1}$. This is most likely a result of the ± 0.5 mm uncertainty in selecting the midpoint of the dose distribution. Both the 6 MV and ^{60}Co data agree with the ^{192}Ir data within this margin of error, however there seems to be a slight trend of under-response in the ^{192}Ir data at higher doses. The reason for this is at present undetermined but within the accuracy of the experiment it can be concluded that the dosimeter response is equivalent for photons of energy ranging from ~ 400 keV (mean energy of ^{192}Ir) to ~ 2 MeV (mean energy of 6 MV beam), as expected from the discussion in Section 2.1.

Due to the very sharp dose gradients present around the source, ion diffusion may have significant implications for quantitative brachytherapy MRI dosimetry. Measurements of the $\Delta R2$ profile along the perpendicular bisector of the source at 20 minute intervals over a 1 1/2 hour period following irradiation are shown in Figure 6.8. A dose of 17 Gy at 2 cm from the source was delivered in 21.6 minutes. The imaging sequence involved a voxel size of 1 mm x 1 mm x 5 mm (slice thickness) and took 17.1 minutes. The times listed in Figure 6.8 represent the intervals from the midpoint of irradiation to the midpoint of each scanning sequence.

---

[a] Mathematica Version 2.0.4, Wolfram research Inc., Champaign IL

From this data it is evident that ion diffusion has a marked effect on the measurement of dose within a 12 mm radius of the source. The dip in $\Delta R2$ at the central position is due in part to the presence of the catheter and in to part to the reduction of Fe^{3+} to Fe^{2+} in this region of very high dose. Beyond 12 mm, the shape of the dose profile is essentially unperturbed over the 103 minute interval following irradiation. For many clinical applications it is not necessary to measure doses at distances less than 15 mm from the source, and therefore the MRI gel technique described here will likely be a useful dosimetry modality for HDR brachytherapy.

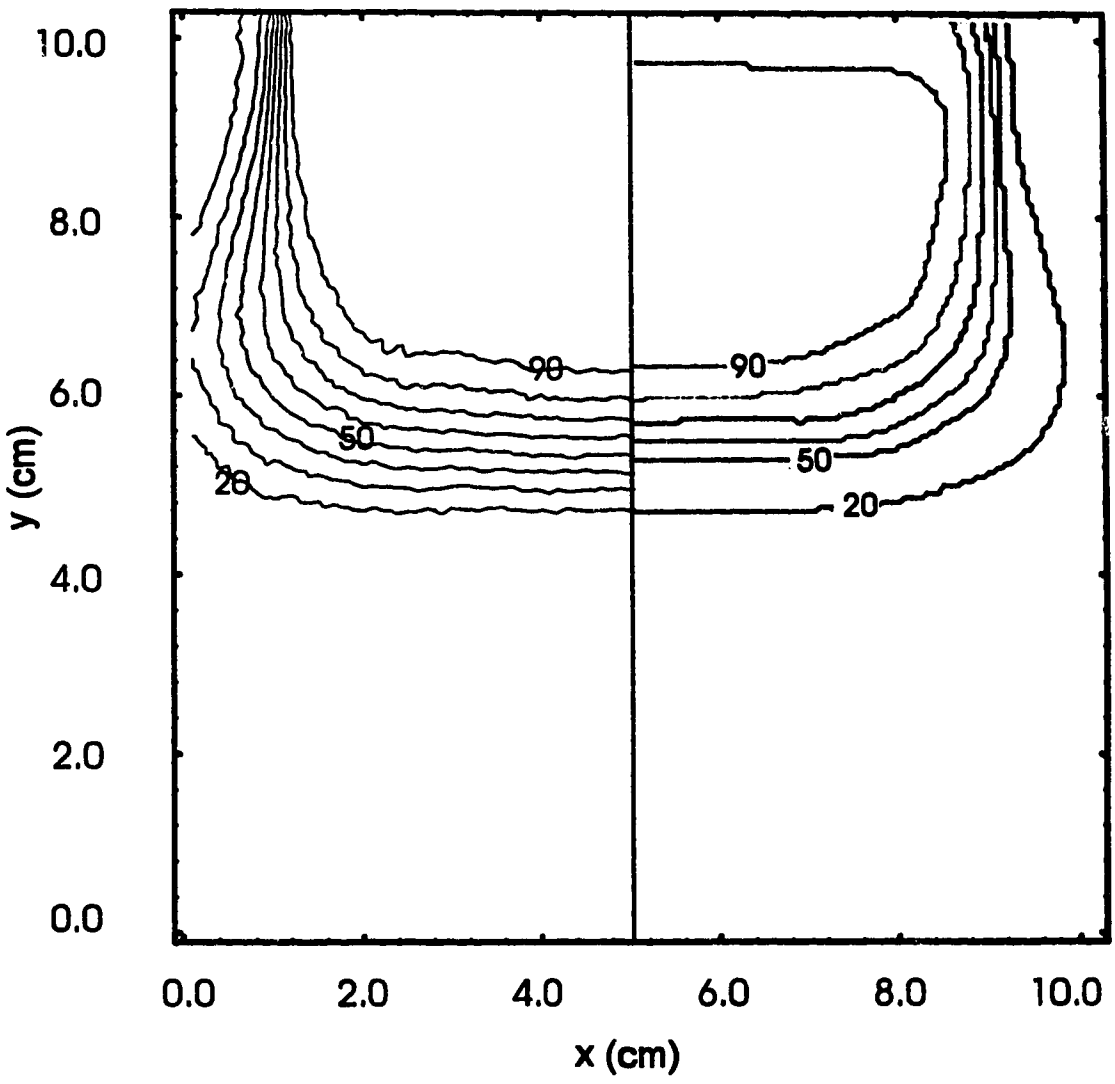

Figure 6.1 Isodose curves for a 12 MeV electron beam in 10% increments. A dose of 30 Gy was delivered to the 100% normalization point at a depth of 2.8 cm on the central axis. At the left are data measured using the MRI echo quotient technique. Imaging was done in the transverse plane. At the right are data measured using a diode.

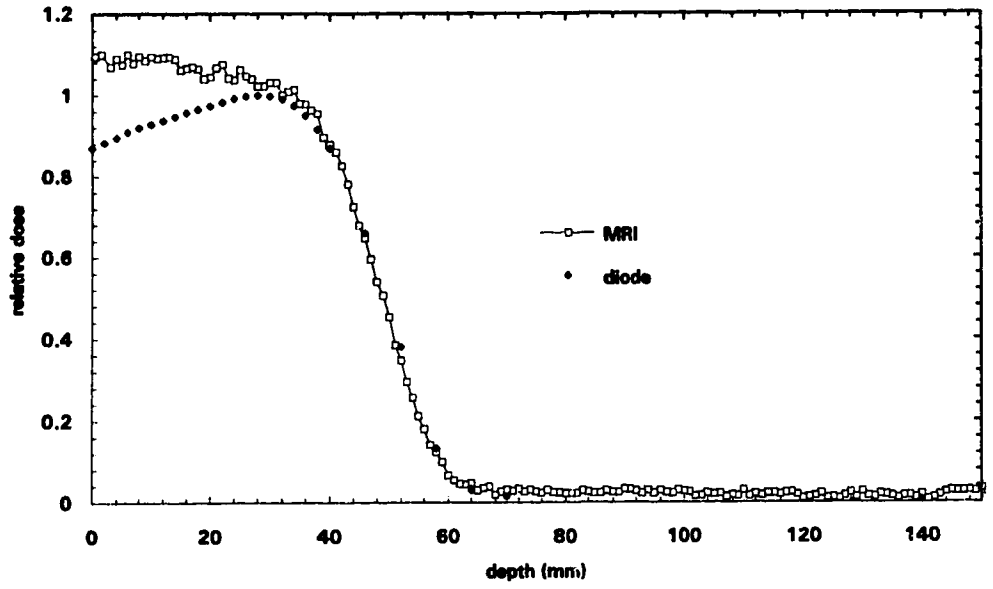

Figure 6.2 Comparison of relative dose along the central beam axis, measured with MRI and diode for a 12 MeV electron beam. Values are normalized to 1.0 at a depth of 2.8 cm.

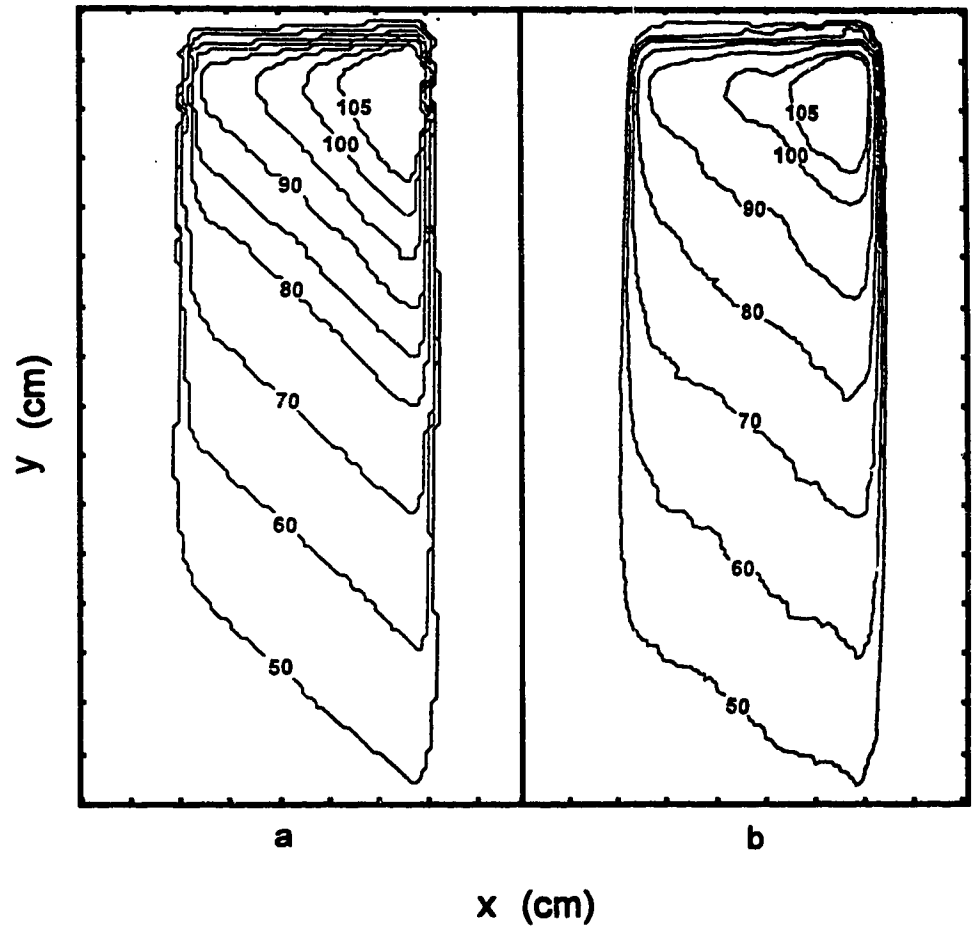

Figure 6.3 Isodose curves for a 6 MV dynamically-wedged photon beam. Isodose curves were normlaized to 100% at a depth of 1.5 cm on central axis where a dose of 20 Gy was delivered. Curves in a)were measured using film and ion chamber whereas curves in b) were measured using the echo quotient technique.

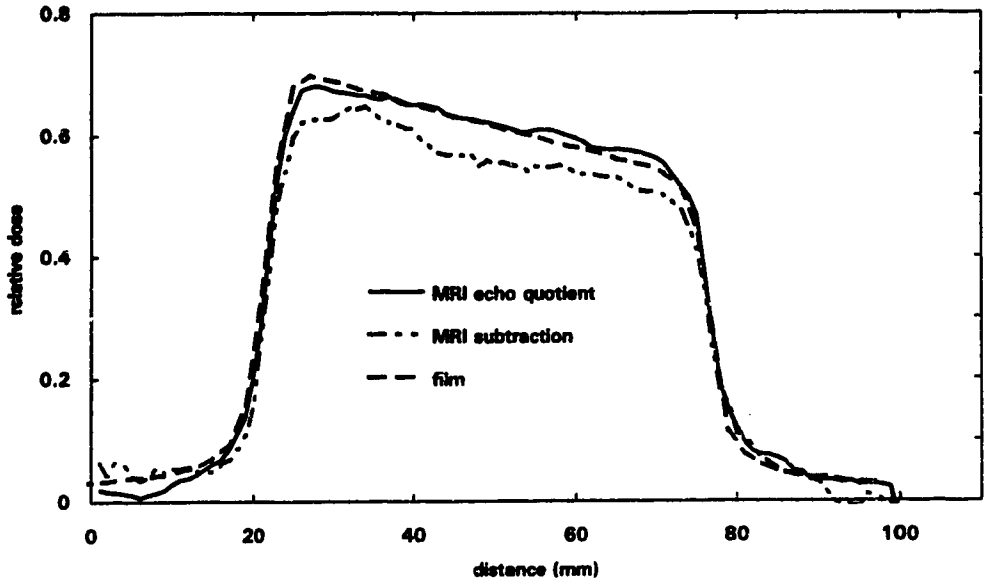

Figure 6.4a Comparison of 6 MV dynaimcally-wedged photon beam relative dose profiles at a depth of 10.0 cm. Values are normalized to 1.0 at a depth of 1.5 cm along the central axis.

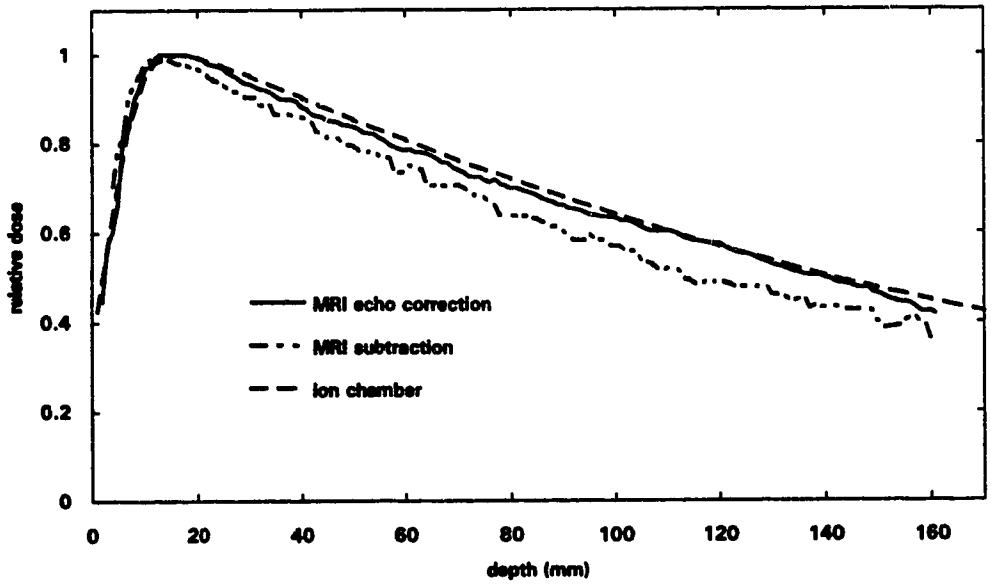

Figure 6.4b Comparison of 6 MV dynamically-wedged photon beam relative depth dose curves along the central beam axis. Values are normalized to 1.0 at a depth of 1.5 cm along the central axis.

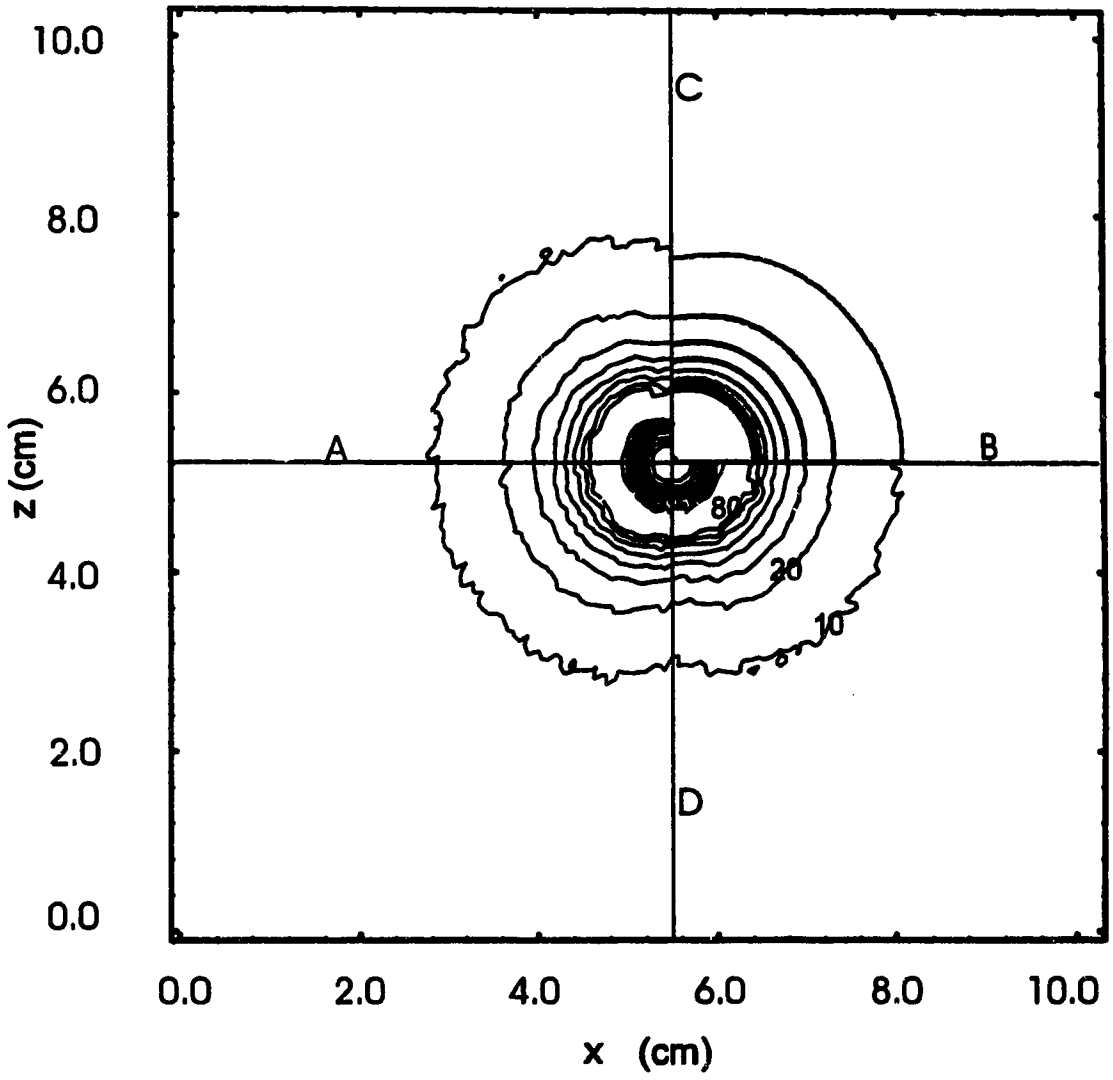

Figure 6.5 Isodose distribution for an ^{192}Ir HDR source. The single catheter applicator axis lies along the line CD. Isodose values range from 10 Gy to 80 Gy in 10 Gy increments. Inner contours are a result of dose response inversion at dose levels beyond 100 Gy. The upper right quadrant contains isodose lines calculated using the Nucletron planning system. Imaging was done in the coronal plane.

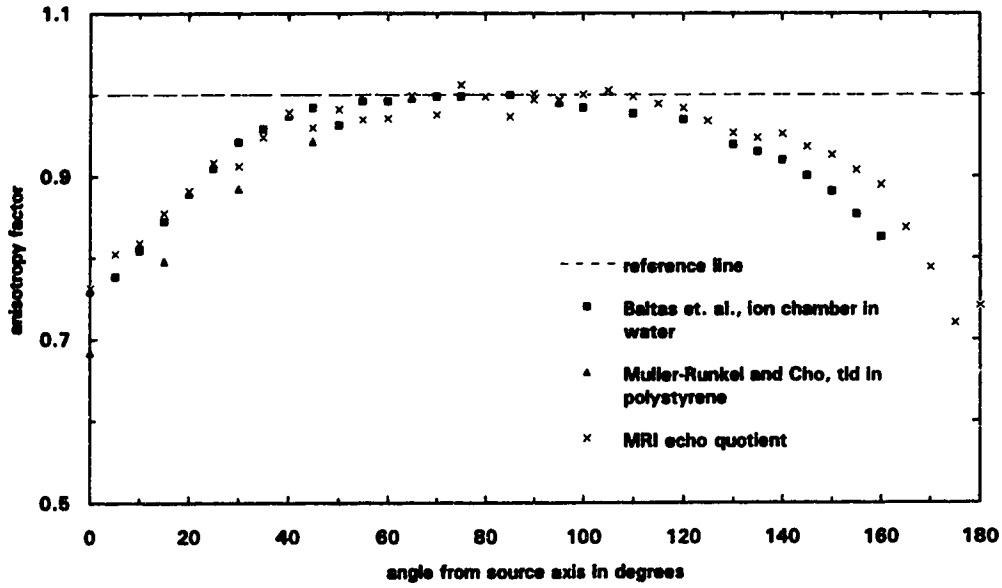

Figure 6.6. Comparison of anisotropy measurements about the ^{192}Ir microSelectron HDR stainless steel encapsulated source. The 0° position lies along the applicator axis indicated by the line CD in Figure 6.5. MRI values are an average over left and right sides of the dose distribution.

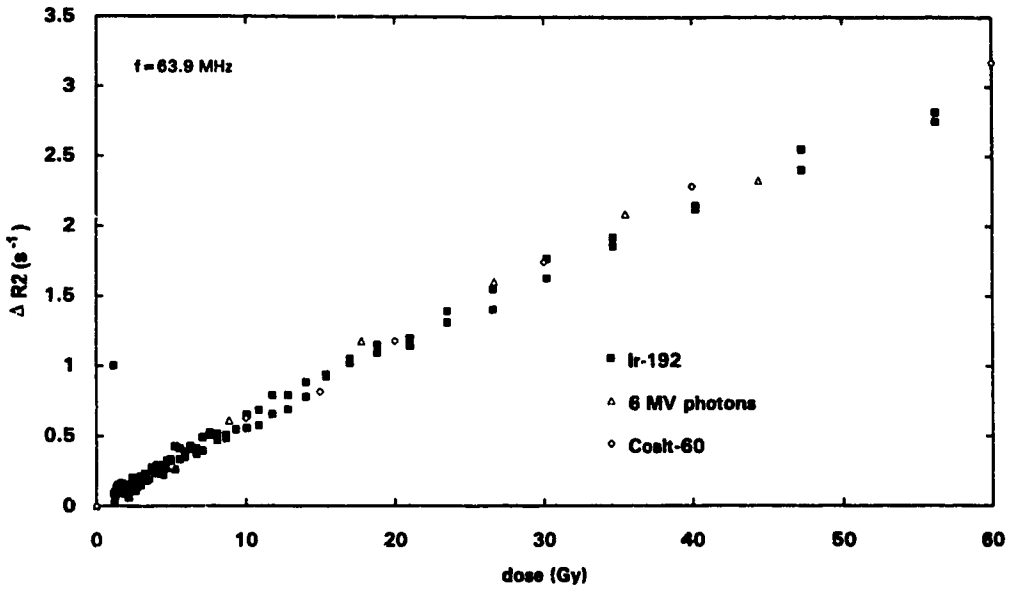

Figure 6.7. Comparison of dose response curves obtained for an ^{192}Ir HDR source (both left and right sides of the dose distribution) with those obtained for ^{60}Co photons and 6 MV photons. The phantom material was 4% gelatin, 0.05 M H_2SO_4, 1 mM $FeSO_4$ in all cases. Slice thickness was 5 mm.

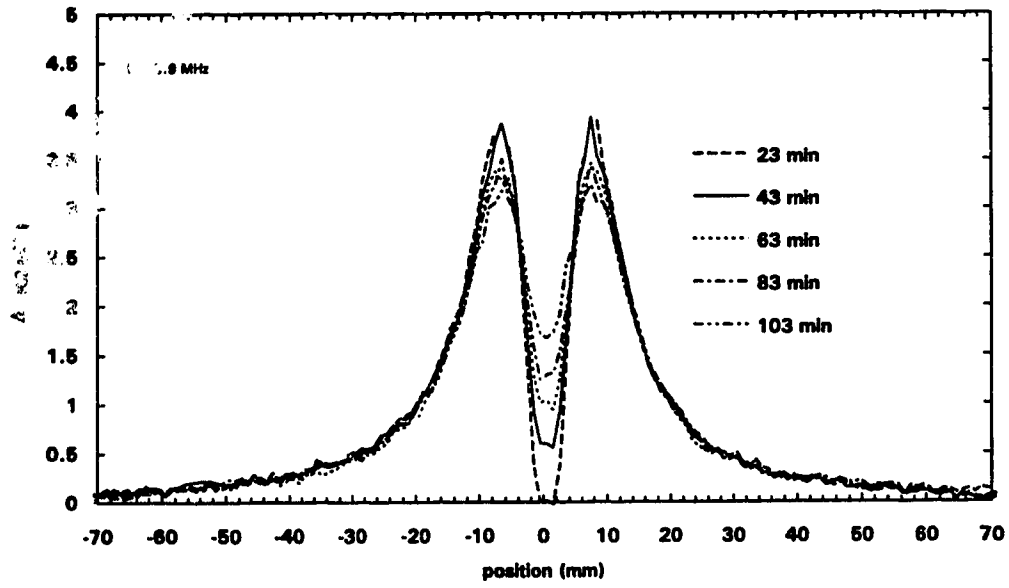

Figure 6.8. $\Delta R2$ profiles along the perpendicular bisector of an ^{192}Ir source measured at various post-irradiation times. The phantom material was 4% gelatin, 0.05 M H_2SO_4 and 1 mM $FeSO_4$. The measurements were done in the coronal imaging plane using the echo quotient technique. Slice thickness was 5 mm.

Chapter 7

Summary and conclusions

The potential for accurate dosimetry using MRI to measure changes in spin-spin relaxation rate in Fricke-gelatin phantoms has been investigated. It has been demonstrated that *R2* is a more sensitive measure of dose than *R1* and that 50 - 100% increases in *R2* sensitivity occur at proton resonant frequencies of 64 to 100 MHz compared with 20 MHz. One possible explanation for this is an increasing electron spin relaxation time for the ferric ion at higher frequencies. It is therefore recommended that *R2* be the parameter of choice over *R1* when an accurate *R2* measurement technique, such as the phase-alternated CPMG sequence, is available.

The change in relaxation rate with absorbed dose has been shown to be highly dependent on the composition of the gel material. Increasing concentrations of H_2SO_4 and O_2 serve to sensitize the dosimeter. However, increasing the concentration of H_2SO_4 also increases the rate of ion diffusion and subsequent blurring of the measured dose distribution. Increased gelatin concentration does not significantly reduce ion diffusion rates in the 0.05 M H_2SO_4 dosimeter material and leads to depressed sensitivity as a result of increased pH. The optimum ferrous sulphate-gelatin material in terms of both sensitivity to dose and ion diffusion contains 0.05M H_2SO_4, and 4% gelatin in addition to 1mM $FeSO_4$. Optimization of ferric ion concentration has been examined elsewhere [Olsson et al 1989].

Varying degrees of oxygenation throughout a large phantom volume as a result of preparation conditions can lead to variation in gel sensitivity. This moderates somewhat the original supposition made in Chapter 1 that gelatin might be preferred over agarose as a gelling agent due to less severe oxygen loss during the preparation stage. However, the gelatin based material is still simpler to prepare than agarose. For thin layers (2 mm) of Fricke gelatin prepared with no additional reoxygenation, the dose response curve extends linearly to ~ 120 Gy. Problems associated with preparation, such as air bubbles near the surface, and non-uniformity of layer thickness, make the use of large gel "cassettes" difficult for dosimetry purposes. For larger samples representative of the full phantom situation, saturation occurs at ~ 80 Gy, comparable to the saturation in reoxygenated agarose at ~ 70 Gy [Schulz et al 1990]. At doses beyond ~ 100 Gy in large phantoms, the dose response shows inversion, indicating reduction of ferric ions to ferrous ions.

Increases in phantom temperature lead to decreasing *R2* values in Fricke gelatin. Evidence in Figure 4.16 suggests that irradiated Fricke gelatin undergoes a larger drop in *R2* than unirradiated Fricke gelatin as temperature is increased. Temperature therefore affects the dose response sensitivity of Fricke gelatin, and it is essential that a constant uniform phantom temperature be maintained during the imaging process. It may also be worth investigating the dose response and ion diffusion properties of Fricke gelatin as a function of phantom temperature since both may be improved at lower temperatures. This would require the development of a temperature regulating device to maintain thermal equilibrium of the phantom at reduced temperatures.

The G of ~ 44 ions $(100\ eV)^{-1}$ for Fricke gelatin, although substantially enhanced value in liquid Fricke (15.6 ions $(100\ eV)^{-1}$) is inferior to ~ 100 ions (agarose Fricke [Olsson 1991, Schulz et al 1990]. The addition of small amo nzoic acid does not enhance the ferric ion yield in the Fricke gelatin dosimeter. The doubling of the Fe^{3+} yield in agarose as compared with gelatin appears at first glance to indicate that agarose should be preferred to gelatin for Fricke MRI studies. With higher Fe^{3+} yield, lower doses requiring shorter irradiation times can be used with Fricke agarose compared with Fricke gelatin. This could potentially be an advantage when diffusion of Fe^{3+} ions within the gel proceeds at a rapid rate.

Diffusion of Fe^{3+} ions throughout the gel medium following irradiation compromises the integrity of the measured dose distribution. The significance of ion diffusion depends on the distribution being measured. For external beam radiotherapy where the steepest gradient in ferric ion concentration occurs in the penumbral region, diffusion results in a minimum of 1.5 mm spread in the measured beam penumbra over 2 hours. In general, a time lapse between irradiation and imaging of up to two hours for external beam dosimetry should be tolerable. In the case of HDR brachytherapy, it has been demonstrated that beyond a 1.2 cm radius about an ^{192}Ir source, change in the dose distribution is negligible over a 2 hour period following irradiation. However, in regions of steep ferric ion gradient as are found within 1 cm of the source (due to reversal of the oxidation processes), filling in of the region of low ferric ion concentration is evident after 20 minutes. Thus in narrow regions of low ferric ion concentration surrounded on both sides by high ferric ion concentration, as might be found behind narrow blocks such as eye shields, accurate measurement of dose will be difficult. An approximate diffusion coefficient of $0.027 \pm 0.005\ cm^2\ hr^{-1}$ has been established for the standard 4% gelatin, 0.05 M H_2SO_4 and 1 mm $FeSO_4$ material, indicating only a slight disadvantage compared with agarose Fricke gels having a diffusion coefficient of $0.019 \pm 0.001\ cm^2/hr$ [Schultz

et al 1990, Olsson et al 1992] and the gelatin material can be certainly used in MRI dosimetry without undue difficulty.

A novel method of correcting for non-uniformity in tip angles across large volume phantoms in MRI has been demonstrated. The echo quotient technique can be used to measure $\Delta R2$ distributions, providing better uniformity in response and reduced noise compared with $R2$ subtraction techniques. Also, a considerable savings in imaging time compared with single Hahn echo techniques is achieved. An image acquisition time of 17 minutes and slice thickness of 1 cm with 0.1 cm x 0.1 cm spatial resolution allows for a minimum detectable dose of ~ 1 Gy. This also corresponds to the level of uniformity achievable in the dosimeter response throughout the phantom, except in the vicinity of phantom edges where the maximum distortion using the echo quotient technique corresponds to a dose level of ~ 3 Gy.

Applications of the techniques developed in Chapter 5, to clinical dosimetry situations as described in Chapter 6, indicate the potential of MRI $\Delta R2$ dosimetry to be a valuable adjuvant dosimetry tool. Guidelines for implementation of accurate large phantom Fricke gel dosimetry include:

- measure $\Delta R2$ at the highest available imaging frequency,
- use an accurate measurement technique such as the echo quotient method,
- use a dosimeter composition of 0.05 M H_2SO_4, 4% gelatin by weight and 1mM $FeSO_4$,
- stay within a maximum dose of 20 Gy to avoid significant O_2 depletion and non-linearity of dose response,
- ensure a constant phantom temperature during the imaging process,
- perform the MRI measurements within 2 hours of phantom irradiation,
- allow a 2 cm margin between the expected dose distribution and the phantom edges in the phase encode direction.

Based on the studies detailed in this thesis, several suggestions for future work that could further improve $\Delta R2$ MRI dosimetry include:

- investigate the $\Delta R2$ response at higher field strengths and better define the contact interaction parameters for the Fe^{3+} ion
- determine the origin of residual $\Delta R2$ distortion near phantom edges in the phase encode direction
- fully determine the cause of the overresponse to dose near the phantom surface for electron beam irradiation

- investigate the possibility of incorporating anatomical inhomogeneities into gel phantoms and how susceptibility differences affect $\Delta R2$ in the vicinity of the structures.
- investigate possible *R2* contrast enhancement and ion diffusion reduction by using a lower gel temperatures
- investigate alternatives to the phase alternated CPMG sequence and extend image acquisition to 3 D.

References

AAPM 1992 "The Physics of Magnetic Resonance Imaging" *Proceedings of the AAPM Summer School*, Banff Alberta

Ablett S, Lillford P J, Baghdadi S M A and Derbyshire W 1978 *Journal of Colloid and Interface Science* **67** 355-377

Abragam A 1961 "The Principles of Nuclear Magnetism", (Oxford University Press: Oxford)

Appleby A, Christman E A, and Leghrouz A 1987 Imaging of spatial radiation dose distribution in agarose gels using magnetic resonance *Med. Phys.* **14** 382-384

Attix F H and Roesch 1966 "Radiation Dosimetry II: Instrumentation" (Academic Press: New York)

Attix F H 1986 "Introduction to Radiological Physics and Radiation Dosimetry" (John Wiley and Sons: New York)

Audet C, Keller B M, Schreiner L J 1993 NMR Relaxation in the Fricke-Gelatin Dosimeter *Proceedings of the SMRM Annual Meeting (abstract)*

Audet C and Schreiner L J 1991 NMR-based radiation dosimetry using polymer solutions, (abstract) *Med. Phys.* **18** 645

Audet C and Schreiner L J 1994 Multiple site fast exchange model for spin-lattice relaxation in the Fricke-gelatin dosimeter *COMP Annual Scientific Meeting*, Toronto

Beddar A S , Mackie T R and Attix F H 1992a Water-equivalent plastic scintillation detectors for high energy beam dosimetry:I. Physical characteristics and theoretical considerations *Phys. Med. Biol.* **37**(10) 1883-1900

Beddar A S , Mackie T R and Attix F H 1992b Water-equivalent plastic scintillation detectors for high energy beam dosimetry: II Properties and measurements *Phys. Med. Biol.* **37**(10) 1901-1913

Berendsen H J 1962 Nuclear magnetic resonance study of collagen hydration *J.Chem. Phys.* **36**(12) 3297-3305

Bloch F W, Hansen W W and Packard M 1946 The Nuclear Induction Experiment, *Phys. Rev.* **69** 127

Bloembergen N, Purcell E M, and Pound R V 1948 Relaxation effects in nuclear magnetic resonance absorption *Phys. Rev.* **73** 678

Bloembergen N 1950 On the shift of the nuclear magnetic resonance in paramagnetic solutions *Phys. Rev.* **79** 179-180

Bloembergen N 1957 Proton relaxation times in paramagnetic solutions *J.Chem. Phys.* **27**(2) 572-573

Bottomley P A and Andrew E R 1978 RF magnetic field penetration phase shift and power dissipation in biological tissue:implications for NMR imaging *Phys. Med. Biol.* **23**(4) 630-643

Brunt U N H, Eagle J A, Kacperek A, Lawrence G P and Shaw J E 1994, Display and analysis of proton dose distributions from a therapy cyclotron using magnetic resonance imaging of Fricke gels *Proceedings of the XIth International Conference on the use of Computers in Radiation Therapy*, Manchester U.K., 360-361

Carr H and Purcell E M, 1954 Effects of diffusion on free precession in nuclear magnetic resonance experiments *Phys. Rev.* **94** 630-638

Chan M. F and Ayyangar K 1993 Verification of Water Equivalence of FeMRI gels using Monte Carlo Simulation, *35th Annual Meeting of the AAPM* Washington DC

Charlesby A 1981 Crosslinking and degradation of polymers *Radiat. Phys. Chem.* **18**(1-2) 59-66

Crawley A P and Henkelman R M 1987 Errors in T2 estimation using multislice multi-echo imaging *Mag. Res. Imag.* **4** 34-47

deGuzman A, Gore J C, Schultz R J 1989 Dose-response curves for gels infused with Fricke dosimeter by NMR *Med. Phy.s* (abstract) **16**(3) 457

Dixon R L and Ekstrand K E 1982 The physics of proton NMR *Med. Phys.* **9** 807

Duzenli C, Sloboda R, and Robinson D 1994 A spin-spin relaxation rate investigation of the gelatin ferrous sulphate NMR dosimeter *Med.Phys.Biol.* **391577-1592**

Duzenli C and Robinson D 1994 Correcting for RF inhomogeneities in multi-echo pulse sequence MRI dosimetry *Med.Phys.* (submitted Nov.1994)

Edelstein W A , Glover G H , Hardy C J and Redington R W 1986 The intrinsic signal to noise ratio in NMR imaging *Mag. Res. Med.* **3** 604-618

Eisinger J, Shulman R G, Szymanski B M 1962 Transition metal binding in DNA solutions *J. Chem.Phys.* **36**(7) 1721-1729

Foo Thomas K F , Hayes Cecil E and Kang Yoon-Won 1991 An analytical model for the design of RF resonators for MR body imaging *Mag. Res. Med.* **21** 165-177

Fransson A, Ericsson A, and Sperber G O 1993 MRI Measurments of the Dependence on T1 of the echo amplitudes using a multiple spin-echo scheme *Mag. Res. Imag.* 11 1185-1192

Fraunfelder H and Henley E M 1974 "Subatomic physics" (Prentice-Hall:Toronto)

Fricke H and Hart E J 1966 in "Radiation Dosimetry II Instrumentation" ed. Attix and Roesch (New York: Academic) 167-240

Fricke H and Morse S 1927 The chemical action of roentgen rays on dilute ferrous sulphate solutions as a measure of dose *Am J. Roentgenol. Radium Therapy Nucl. Med.* **18** 430

Fricke H and Peterson B W 1927 The relation of chemical, colloidal, and biological effects of rontgen rays of different wavelengths to the ionization which they produce in air I. Action of rontgen rays on solutions of oxyhemoglobin in water *Am J. Roentgenol. Radium Therapy Nucl. Med.* **17** 611

Gambarini G, Arrigoni S, Cantone M C, Molho N, Facchielli L and Sichirollo A E 1994 Dose-response curve slope improvement and result reproducibility of ferrous-sulphate-doped gels analysed by NMR imaging *Phys. Med. Biol.* **39** 703-717

Geisselsoder J , Kingkade M J and Laughlin J S 1963 The radiation chemistry of aqueous ferrous sulphate-benzoic acid solutions, *Radiat. Res.* **20** 263

Gore J C, Kang Y S, Schultz R J 1984 Measurement of radiation dose distibutions by nuclear magnetic resonance (NMR) imaging *Phys. Med. Biol.* **29** (10) 1189-1197

Gore J C, Kennan R P and Zhong J 1992 MRI contrast agents - principles and constraints in "The Physics of MRI " *Proceedings of the AAPM Summer School* Banff 299-319

Graumann R , Oppelt A , and Stetter E 1986 Multiple-spin-echo imaging with a 2D Fourier method *Mag. Res. Med.* **3** 707-721

Guan T Y, Almond P R, Park H C, Lindberg R D, and Shields C B 1993 Imaging of radiation dose for sterotactic radiosurgery *Medical Dosimetry* **18** 135-142

Hahn E L 1950 Spin echoes *Phys Rev* **80** 580-594

Hardy P, Bronskill M J and Henkelman R M 1985 Signal strength on a 0.15-T magnetic resonance imager *Med. Phys.* **12** (5) 581-585

Hazle J D, Hefner L, Nyerick C E, Wilson L, and Boyer A L 1991 Dose-response characteristics of a ferrous-sulphate-doped gelatin system for determining radiation absorbed dose distributions by magnetic resonance imaging (Fe MRI) *Phys. Med. Biol.* **36** (8) 1117-1125

Hendrick R E and Haacke E M 1993 Basic physics of MR contrast agents and maximization of image contrast *J. Mag. Res. Imag.* **3** 137-148

Hiraoka T, Fikuda N., Ikehira H , Hoshino K, Nakazawa K, Tateno Y and Kawashima K 1986 Digital imaging of dose distributions by nuclear magnetic resonance *Nipp. Acta. Radiol.* 46 503-505

Hiraoka T, Fikuda N , Ikehira H , Hoshino K, Tateno Y and Kawashima K 1992a Digital imaging of dose distributions using NMR imager *Nipp. Acta. Radiol.* **52** 1177-1182

Hiraoka T, Fikuda N , Hoshino K, Ikehira H , Nakano T and Kawashima K 1992b Development of a gel phantom for dose distributions by MR imager *Nipp. Acta. Radiol.* **52** 1039-1041

Hiraoka T, Hoshino K, Kawashima K, Kato H, and Tateno Y 1993 A new gel using super absorbant polymer for mapping the spatial dose distributions of electron beams by MR imager *Medical Dosimetry* **18** 73-79

Hubbel J H 1969 "Photon Cross Sections, Attenuation Coefficients, and Energy Absorption Coefficients From 10 keV to 100 GeV" (NSRDS-NBS: Washington DC)

Hughes D G 1977 Errors in T2 values measured with the Carr-Purcell-Meiboom-Gill Pulsed NMR sequence *J. Mag. Res.* **26** 481-489

ICRU Report 37 1984 "Stopping Powers for Electrons and Positrons" (ICRU: Bethesda MD)

ICRU Report 50 1993 "Prescribing, Recording, and Reporting Photon Beam Therapy" (ICRU: Bethesda MD)

Johns H E and Cunningham J R 1983 "The Physics of Radiology" 4th Ed. (Charles C. Thomas: Springfield, Illinois)

Keller B M, Audet C, Schreiner L J 1993 NMR studies of the Fricke-gelatin dosimeter *Conference Proceedings of the C.O.M.P.* Toronto 116-117

Keller B M 1994 "Characterization of the NMR-based Fricke-Gelatin Radiation Dosimeter" *MSc Thesis*, McGill University, Montreal Canada

Koenig S H, Baglin C M and Brown R D III 1985 Magnetic field dependence of solvent proton relaxation in aqueous solutions of Fe^{3+} complexes *Mag. Res. Med.* **2** 283-288

Koenig S H and Brown R D 1984 Relaxation of solvent protons by paramagnetic ions and its dependence on magnetic field and chemical environment:implications for NMR imaging *Mag. Res. Med.* **1** 478-495

Kozar J 1965 "Light Sensitive Systems Chemistry and application of non-silver halide photographic processes" (New York: John Wiley &Sons)

Kozlov P V and Burdygina G I 1983 The structure and properties of solid gelatin and the principles of their modification *Polymer Reviews* **24** 651-666

Kron T , Rajanayagam and Pope J M 1994 Fast T1 imaging for the evaluation of diffusion in NMR imaging dosimetry gels (abstract) *Med. Phys.* **21**(6) 909

Kron T, Metcalfe P, and Pope J M 1993 Investigation of the tissue equivalence of gels used for NMR dosimetry *Phys. Med. Biol.* **38** 139-150

Kron T and Pope J M 1994 Dose distribution measurements in superficial x-ray beams using NMR dosimetry *Phys. Med. Biol.* **39** 1337-1349

Lauterbur P C 1973 Image formation by induced local interactions: examples employing NMR *Nature* **242** 190

Luz Z, and Shulman R G 1965 Proton magnetic resonance shifts in aqueous solutions of paramagnetic metal ions *J. Chem. Phys.* **43**(10) 3750-3756

Majumdar S , Orphanoudakis S C , Gmitro A , O'Donnell M and Gore J C 1986 Errors in the measurement of T2 using multiple-echo MRI techniques *Mag. Res. Imag.* **3** 397-417

Maquet J, Theveneau H, Djabourov M, Leblond J, and Papon P 1989 State of water in gelatin solutions and gels: An ^1H NMR investigation *Polymer* **27** 1103-1110

Maryanski M J , Gore J C, Kennan R P ,and Schulz R J 1993 NMR relaxation enhancement in gels polymerized and cross-linked by ionizing radiation: A new approach to 3D dosimetry by MRI *Mag. Res. Imag.* **11** 253-258

Maryanski M J Ibbott G S , Xie J , Gore J C , and Schultz R J 1994 Magnetic resonance imaging of dose distributions from brachytherapy sources embedded in tissue equivalent BANG polymer dosimeters *Med. Phys.* **21**(6) 929

Maryanski M J , Schultz R J, Ibbott G S , Gatenby J C , Xie J, Horton D, and Gore J C 1994 Magnetic resonance imaging of radiation dose distributions using a polymer-gel dosimeter *Phys.Med.Biol.* **39** 1437-1455

Maryanski M J and Gore J C 1992 Flip angle variations in large volumes of dielectric and conductive media at high fields:Implications for quantitation of relaxation times from images *Proceedings of the SMRM Annual Meeting*

McLaughlin W L , Yun-Dong Chen, Soares C G , Miller A , Van Dyk G and Lewis D F 1991 Sensitometry of the response of a new radiochromic film dosmeter to gamma radiation and electron beams *Nuclear Instruments and Methods in Physics Research* **A302** 165-176

Meiboom S and Gill D 1958 Modified spin-echo method for measuring nuclear relaxation times *Rev. Sci. Instrum.* **29** 688-691

Menon R S 1991 Baseline errors possible when using RF solenoids for multi-echo transverse relaxation time measurements *Proceedings of the SMRM Annual Meeting* 703

Muhr A H and Blanshard M V 1982 Diffusion in gels *Polymer* **23** 1012-1025

NCRP Report No. 69 1981 "Dosimetry of x-ray and gamma-ray beams for radiation therapy in the energy range 10 keV to 50 MeV "(National council on Radiation Protoection and Measurements: Washington DC)

Olsen D R and Hellesnes J 1994 Absorbed dose distribution measurements in brachytherapy using ferrous sulphate gel and magnetic resonance imaging *British Journal of Radiology* 67 1121-1126

Olsson L E, Petersson S, Ahlgren L, Mattsson S 1989 Ferrous sulphate gels for determination of absorbed dose distributions using MRI technique: basic studies *Phys. Med. Biol.* **34**(1) 43-52

Olsson L E 1991 "Radiation Dosimetry using magnetic resonance imaging" *PhD Thesis* Lund University Malmo, Sweden

Olsson L E , Fransson A , Ericsson A and Mattson S 1990 MR imaging of absorbed dsoe distributions from radiotherapy using ferrous sulphate gels *Phys. Med. Biol.* **35**(12) 1623-1631

Olsson L E , Arndt J, Fransson A and Nordell B 1992 Three-dimensional dose mapping from gamma knife treatment using a dosimeter gel and MR-imaging *Radiotherapy and Oncology* **24** 82-86

Olsson l E , Westrin B A , Fransson A , and Nordell B 1992 Diffusion of ferric ions in agarose dosimeter gels *Phys.Med.Biol.* **37** 2243-2252

Podgorsak M B, Schreiner L J 1992 Nuclear magnetic relaxation characterization of irradiated Fricke solution *Med. Phys.* **19**(1) 87-95

Prasad P V, Nalgioglu O, Rabbani B, 1991 Measurement of three-dimensional radiation dose distributions using MRI *Rad. Res.* **128** 1-13

Press W H , Flannery B P , Teukolsky S A , and Vettering W T 1988 "Numerical Recipes in C: the art of scientific computing" (Cambridge University Press: Cambridge) 542-547

Proctor B E and Goldblith S A 1950 Oxidation-reduction dyes as radiation indicators *Nucleonics* 7(2) 83

Purcell E M , Torrey H C and Pound R V 1946 Resonance absorption by nuclear magnetic moments in a solid *Phys. Rev.* **69** 37

Rikner G 1983 "Silicon diodes as detectors in relative dosimetry of photon, electron and proton radiation fields" PhD Thesis, University of Uppsala Sweden

Rousseaux J, Gibon D, Sarrazin T H, Doukhan N and Marchandise X 1994 Magnetic resonance imaging of agarose gel phantom for assessment of three-dimensional dose distribution in linac radiosurgery *B.J.R.* **67** 646

Schreiner L J MacTavish J C, Pintar M M and Rupprecht A 1991 NMR spin grouping and correlation exchange analysis: Application to low hydration NaDNA paracrystals *Biophys. J.* **59** 221

Schreiner L J, Crooks I, Evans M D C , Keller B M , and Parker W A , 1994 Imaging of HDR brachytherapy dose distributions using NMR Fricke-gelatin dosimetry *Mag. Res. Imag.* **12** 901-907

Schenk J F 1992 Radiofrequency coils: types and characteristics, in "The Physics of Magnetic Resonance Imaging" *Proceedings of the AAPM Summer School,* Banff

Schulz R J, deGuzman A F, Nguyen D B, and Gore J C 1990 Dose response curves for Fricke-infused agarose gels as obtained by nuclear magnetic resonance *Phys.Med.Bio.* **35** 1611-1622

Schulz R J, Maryanski M J, Ibbott G S and Bond J E 1993 Assessment of the accuracy of stereotactic radiosurgery using Fricke-infused gels and MRI *Med. Phys.* **20** 1731-1734

Shankar 1984 "Principles of quantum Mechanics" (Plenum Press: New York)

Slichter C P 1980 "Principles of Magnetic Resonance", 3rd Ed., (Springer Verlag: Berlin)

Solomon I 1955 Relaxation processes in a system of two spins *Physical Review* **99**(2) 559-565

Sumanaweera T , Glover G , Binford T O , and Adler J R 1993 MR Susceptibility Misregistration Correction *IEEE Transactions on Medical Imaging* **12**(2) 251-259

Swallow A J 1973 "Radiation Chemistry" (London: Longman) 136-166

Thomas S J , Wilkinson I D , Dixon A K and Dendy P P 1992 Magnetic resonance imaging of Fricke-doped agarose gels for the visualization of radiotherapy dose distributions in a lung phantom *British Journal of Radiology* **65** 167-169

Veis A 1964 "Macromolecular Chemistry of Gelatin" (New York: Academic)

Vold R L , Vold R R and Simon H E 1973 Errors in Measurements of Transverse Relaxation Rates *J. Mag. Res.* **11** 283-298

Vymazal J, Bulte J W M, Brooks R A, Frank J A and Di Chiro G 1992 T2 field dependence of paramagnetic ions and magnetite *Proceedings of the SMRM Annual Meeting* 1427

Ward A G and Courts A 1977 "The Science and Technology of Gelatin" (New York: Academic)

Wishnia A 1960 Proton relaxation times in protein complexes of paramagnetic ions *J. Chem. Phys.* **32**(3) 871-875

Zur Y, and Stokar S 1987 A phase cycling technique for cancelling spurious echoes in NMR imaging *J. Mag. Res.* **71** 212-228